2021

Accident Tolerant Fuels Claddings and the Evolution of their Surface Characteristics under Critical Heat Flux

Rajnikant V. Umretiya
Virginia Commonwealth University

Accident Tolerant Fuels Claddings and the Evolution of their Surface Characteristics under

Critical Heat Flux

A thesis submitted in partial fulfillment of the requirements for the Degree of Doctor of Philosophy

at Virginia Commonwealth University.

By

RAJNIKANT V UMRETIYA

Master of Science, Virginia Commonwealth University

Director: Dr. Jessika V Rojas

Assistant professor

Department of Mechanical and Nuclear Engineering

Committee:

Dr. Raul B Rebak

Dr. Reza Mohammadi

Dr. Mark Anderson

Professor James Miller

Virginia Commonwealth University

Richmond Virginia

April 2021

Acknowledgments

I would like to thank my advisor Dr. Jessika Rojas for her constant support and guidance throughout this project. Her expertise, advice, and mentorship were invaluable for the research in this dissertation. Her dedication to conducting research inspired me to have a profound appreciation in engineering and science. I would like to appreciate my former advisor Dr. Sama Bilbao y Leon, for giving me the opportunity to work on this project. I am grateful for the support and involvement of my advisory committee members Dr. Raul B. Rebak, Dr. Reza Mohammadi, Dr. Mark Anderson and Professor James Miller.

I would also like to thank Dr. Carlos Castano for his guidance and for allowing us to use the PVD coating device in his lab. I would also like to thank his students, Santiago Vargas and Dr. Diana Galeano, for helping me with coating and XPS analysis. I am especially thankful to Daniel Ginestro and Robert Uhorchuk for helping me taking some surface characterization data at the beginning of this project. I appreciate working with Gilbert Annohene, Monish Sapkota, Josh Carter, and many others on our graduate coursework and projects. I like to thank the staff at the Nanomaterials Core Characterization (NCC) Facility in the VCU College of Engineering for their technical support with advanced materials characterization. I acknowledge the Department of Energy's Nuclear Engineering University Program (NEUP) for funding the research.

I am taking this opportunity to thanks my brothers Rajesh and Manish, sisters Sonal and Sangita, cousin Haresh and his family, my in-laws, all my relatives and friends who have always acted like many pillars of strength for me.

My biggest gratitude goes to my beloved wife, Shweta. She was always there when I need her love and support. I cannot express how fortunate I have her with me. Last but not least, none of this work would have been possible without the support and blessings of my parents Bhavnaben Umretiya and Vallabhbhai Umretiya. I owe everything in my life to their everlasting values and principles.

Table of Contents

v

vi

vii

x

Abstract

Accident Tolerant Fuels Claddings and the Evolution of their Surface Characteristics under Critical Heat Flux

By Rajnikant V Umretiya

A dissertation submitted in partial fulfillment of the requirements for the degree of Doctor of Philosophy at Virginia Commonwealth University.

Virginia Commonwealth University, 2021

Director: Dr. Jessika V Rojas

Assistant Professor, Department of Mechanical and Nuclear Engineering.

Intending to increase the performance and safety of existing nuclear power plants, the research and development of Accident Tolerant Fuels (ATFs) are of high priority within the nuclear community. There are two widely studied ATF concepts. The first one consists of replacing currently used zirconium alloy for other cladding materials that provide resistance to hydrogen production during accident conditions. The second is the deposition of protective functional coatings on the Zircaloy cladding to mitigate the risk. Cr-coated Zircaloy and FeCrAl alloys are currently being considered for ATF candidates. However, understanding the evolution of ATF materials' surface characteristics, microstructure, and mechanical properties when exposed to the Critical Heat Flux (CHF) in flow boiling testing is a critical need as these materials continue to mature for nuclear reactor applications. In this dissertation, the surface properties of FeCrAl alloys (APMT and C26M), Zircaloy-2, Zircaloy-4, and Cr-coating on Zircaloy-4 substrates produced by Physical Vapor Deposition (PVD) and Cold Spray were investigated according to their chemistry, topography, and wettability. The static contact angle changed from 75º for as-received Zircaloy-4 substrates to almost 20º after the Cr coating deposition. However, this significant increase in wettability observed after chromium deposition on Zircaloy changed with environmental surface aging. Investigations of the surface chemistry and surface energy studies helped explain the contact angle variation with aging time for the plasma-treated surfaces. Results demonstrated that the formation of chromium oxides and hydroxides, and other carbonaceous species affected the surface coating affinity

with water upon ambient exposure. The Surface chemistry of the Cr-coated Zircaloy and the two FeCrAl alloys, APMT and C26M, after CHF was studied thoroughly to understand its evolution at the early stage high-temperature exposure in short periods. The X-ray photoelectron spectroscopy (XPS) results from Cold Spray Cr coating evidenced a higher level of chromium attributed to oxides, while the PVD Cr coating showed a large amount of carbon on the surface. The results from post-CHF FeCrAl alloys indicated a thin layer composed of oxides and hydroxides of Al, Cr, and Fe with varying proportions at different depths in the layer, as indicated by high-resolution XPS and depth profiling. Cross-sectional examination using focused ion beam (FIB) revealed the ~100-200 nm thick oxide layer for both alloys. The evolution of the materials' surface chemistry also led to a noticeable increase in their wettability, with a slight increase in roughness. The investigation of the materials' mechanical properties indicated an increase in hardness by 10-15% and an increase in their yield strength, as evidenced by the microindentation and ring compression tests conducted before and after CHF testing.

Chapter 1: Motivation and Research Objectives

1.1 Introduction

Following the station blackout event at the Fukushima Daiichi nuclear power plant in 2011, which led to hydrogen explosions and a release of radionuclides to the environment, issues concerning light water reactor (LWR) fuel performance under accident conditions were raised [1]. These events negatively impacted the public perception of nuclear energy production regarding reliability and safety [1-3]. However, this accident gave a message to the nuclear community that a decrease in the oxidation rate of Zr-based alloys at high-temperature is a key issue involved in improving the fuel assembly's accident tolerance. In the United States, Congress has directed the Department of Energy, Office of Nuclear Energy, to initiate the United States Fuel Cycle Research and Development Advanced Fuels Campaign program to focus on developing nuclear fuels and cladding with enhanced accident tolerance [4]. Accident tolerant fuels (ATF) are defined as fuels that, in comparison with the standard UO_2- Zircaloy fuel cladding system, can tolerate a loss of active cooling in the reactor core for a considerably longer amount of time, while maintaining or improving the fuel performance during normal operating conditions, design basis accidents, and beyond design basis accidents [5-7]. Materials must have several properties such as low oxidation rate, high thermal performance, and stable mechanical properties under normal and accident operational conditions to qualify for ATF cladding candidate. Among these desired characteristics, improved resistance to high-temperature steam oxidation is considered a priority [3]. From this standpoint, materials that form protective oxide layers of chromia, alumina, or silica are far more resistant than Zirconium to high-temperature steam oxidation. These oxide layers limit the diffusion of oxidizing species, protecting the underlying material [8]. Many ATF cladding concepts are being considered to improve upon the performance of current Zr-based alloys, especially in terms of oxidation resistance and mechanical strength under accident conditions [9-15]. Systematic experimental testing showed improved oxidation resistance of several cladding candidates, for example (a) Zr alloy coatings [16-20], (b) Mo-Zr cladding [10][21], (c) FeCrAl alloys [14][22-23], and (d) SiC_f/SiC cladding [15][24-

27]. Several factors should be considered as positive attributes while designing ATF, such as safety, economics, the fuel cycle, technological challenges, and the development schedule. The ATF concepts widely studied to meet these requirements are grouped as near-term solutions [16] and long-term technologies [28-29].

The nuclear industry has developed infrastructure, experience, and expertise on Zr-based fuel cladding to the maximum extent possible. Thus, the deposition of coatings on the current Zircaloy appears to be one promising near-term ATF cladding concept. The advantages related to this approach include 1) well-known physical and chemical properties of the substrate material, 2) reduced fretting corrosion, and 3) minimized hydrogen release during loss-of-coolant accidents [16][30-31]. This strategy becomes a practical way to improve the existing nuclear fuel system, thus finding intense research interests. There are two main research areas for the coated cladding: the coating material and the coating technology. In this regard, different protective coatings and coating methods are being studied to replace the current cladding with reliable ATF systems [3][16][18-20][32-43]. Chromium is a coating material that has shown promising results among the different considered so far and being tested [35][38][44-51]. Several coating technologies have been highlighted to produce high-quality Cr coatings on Zircaloy-4, including Chemical Vapor Deposition (CVD) and Physical Vapor Deposition (PVD), Thermal Spraying, and Cold Spray [40][45][52-56]. Among them, the latest generations of PVD and Cold Spray are the most widely used and most promising methods [36][38-39][57]. In the French Joint Research program, Framatome developed full-length PVD Cr-coated M5® cladding tubes, with ~15 μm thickness of Cr coating [45][58]. Westinghouse is developing Cr-coated cladding of ZIRLO® and Optimized ZIRLO™ using a Cold Spray process [59-60]. In general, polishing steps of the external surface have been developed to achieve a coating thickness of 20 to 30 μm [61-62]. Similar coated cladding concepts are under development at Korea Atomic Energy Research Institute [63], Czech Technical University [54], Ukraine [20], Institute for Energy Technology in Norway [64], and other institutes, evidencing enhanced corrosion resistance under normal conditions compared to the classical alloys Zircaloy-2 and Zircaloy-4 [65-66]. As

2

a nuclear fuel cladding application, the coating must adhere to the substrate to avoid spallation [34-36][47]. Studies on coated tube samples have shown good behavior of Cr-coatings, both in autoclave (415 °C, steam, 100 bars) with conditions close to nominal PWR operating conditions and in high-temperature environments (steam, up to 1300 °C) simulating accidental conditions [11][36][38][51][67-69]. With promising steam oxidation behavior at high temperatures, studies have also reported good irradiation stability of Cr-coatings [70-73]. Cr-coated Zircaloy-4 has demonstrated extraordinary mechanical properties without spallation at room temperature during ring tensile and ring compression tests [35][38][48][50][74]. Additionally, the cold sprayed Cr-coated Zircaloy-4 are more cost-effective compared to zirconium-alloy fuel cladding [36].

Iron-chromium-aluminum alloys, referred to as FeCrAl, also lead ATF cladding candidates in near-term solutions [75]. The outstanding high-temperature oxidation resistance of FeCrAl alloys is vital for developing systems with enhanced safety margins during design-basis and beyond-design-basis accident scenarios for LWRs [7][13][22][76-79]. The literature has evidenced remarkable stability of microstructural and mechanical properties of FeCrAl alloys under radiation doses relevant to LWRs [80-84]. Moreover, high yield and ultimate tensile strength are reported for unirradiated FeCrAl alloys at different temperatures [23][85-88]. FeCrAl alloys have a higher thermal neutron absorption cross-section than Zircaloy, but this can be compensated for by using a thinner cladding with slightly higher enriched fuel to maintain cycle length [23]. Moreover, the fabrication process of FeCrAl alloy is quite similar to current LWR fuel fabrication [22][89]. Similarly, other long-term cladding technologies such as SiC cladding provides good corrosion resistance and low thermal neutron absorption cross-section [28-29].

Despite the favorable characteristics of the cladding materials, an understanding of the candidate materials' thermal-hydraulic performance is needed and is a current matter of intensive research [90]. While evaluating these advanced cladding materials' thermal-hydraulic characteristics, an understanding of Critical heat flux (CHF) is essential. CHF represents the boiling transition point from the nucleate

3

boiling regime that has high heat transfer to the low heat transfer film-boiling regime [91-93]. Due to poor heat transfer at CHF, surface temperature abruptly increases, which may cause material failure [91][94-95]. Therefore, accurate knowledge and, in general, enhancement of the CHF value are important to the design of systems that use nucleate boiling heat transfer. Due to the complexity and the importance of CHF in the field of boiling heat transfer, numerous empirical correlations have been developed based on corresponding experimental outcomes and theoretical reasoning by previous investigators, with the aims of acquiring knowledge about CHF and of eventually enhancing it [96-98]. One of the earlier CHF models, such as Zuber CHF correlation, considered CHF a hydrodynamic instability phenomenon and thus ignored the effects of the boiling surface characteristics [93][99]. However, the experimental evidence suggesting the importance of surface effects on CHF. Key surface parameters that could affect the CHF are surface wettability [100-105], surface roughness [106-114], liquid-spreading ability [94][115-121], capillarity and wickability, [122-126] and porosity [127-129]. The experimental results of Jeong et al. [114] showed the CHF is highly affected by wettability, as determined by contact angle measurements. When the surface wettability of a Zircaloy-4 cladding specimen was modified from hydrophilic to superhydrophilic using the anodization process, the CHF was found to be twice as high compared to the non-modified surface [107]. The effect of oxidation and fractal surface roughness on the wettability and CHF of glass-peened Zircaloy tubes was studied by R.W.L. Fong [129]. As an outcome, higher CHF was noticed for the oxidized glass-peened surface with higher roughness due to oxidation. Similar results in many other studies investigate the surface characteristics of ATF candidates that may lead to changes in their thermal-hydraulic performance [95-97][109][121][125-134]. In more details, numerous analytical models have proven that the CHF strongly depends on the listed surface parameters [94-97][130-131][135-140]. Thus, the surface characteristics, such as roughness and wettability, of ATF cladding materials must be carefully assessed when evaluating their influence in thermal parameters such as CHF.

4

1.2 Motivation

This research project has an overall goal to investigate the ATF surface properties, such as surface topography and wetting characteristics, that may impact the CHF based on thermal-hydraulic experimental data and to study their changes post-CHF testing. This work is motivated by numerous studies investigating the effects of ATF cladding surface characteristics on boiling performance. Kam et al. [119] prepared ATF cladding samples by depositing SiC and chromium coatings on substrate stainless steel using DC magnetron sputtering. The pool-boiling CHF test showed 150% enhancement of CHF for SiC coating from that of the substrate, while CHF for Cr coating decreased by 70%. These results were explained by the superior wettability of SiC coating over Cr coating. The effect of surface roughness for Cr coating deposited on substrate SS316L was studied where an increase in roughness by 0.25 µm resulted in 79% CHF enhancement [116]. Seo et al. [117] reported CHF enhancement of 45% for FeCrAl coating compared to substrate SS316 due to the effect of surface roughness. Cr-coated SS304L samples, oxidized at 400 ℃ in dry air for 20 days, showed 48% of CHF enhancement [120]. Hyun et al. deposited Cr-coating on substrate SS316L using DC magnetron sputtering and recorded 27% CHF enhancement in a pool boiling test due to surface morphology and capillarity wicking [121]. A slight reduction of 12% in CHF was recorded for Cr-coated ZIRLO samples produced by cold spray, and the results were attributed to a slight reduction in wettability and thermal properties of the material [126]. Furthermore, Son et al. [116] demonstrated in their experiment that the roughness-augmented superhydrophilic property effectively delays the CHF occurrence. Fig. 1.1 shows the CHF comparison between experimental data taken from literature and data calculated using CHF models. The green region emphasizes materials with low roughness for fuel cladding applications, as they may be more corrosion-resistant than boiling-friendly high-roughness surfaces. Comparing CHF values between ATF candidates, superhydrophilic Cr-layers showed further enhancement than hydrophilic FeCrAl layers. Here, compared to lumped nanostructures of FeCrAl, particulate nanostructures of Cr-layer enlarge geometric area in nanoscale, and subsequently, enhance wicking potential. In general, surface characteristics such as wettability,

roughness, porosity, thickness of likely oxide layers, and thermal properties of the cladding may have an impact on the characteristics of CHF.
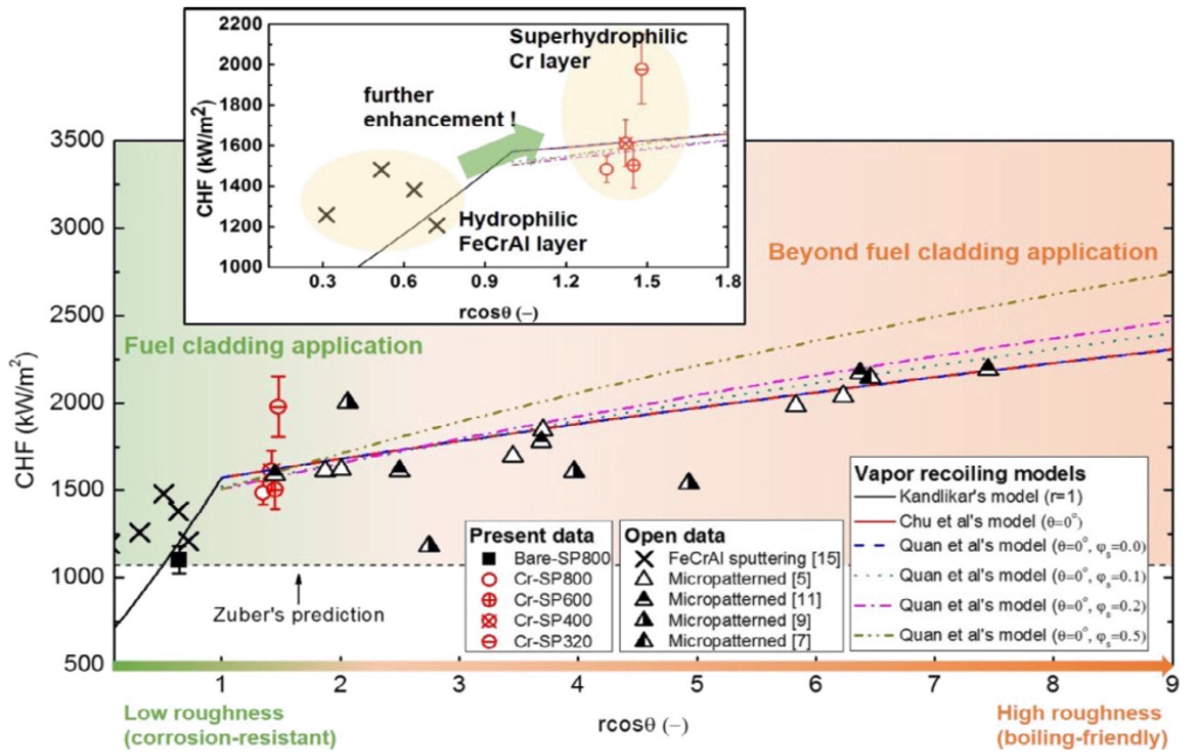
Figure 1.1 Comparison of CHF data in terms of surface roughness factor r and contact angle θ (Son et al.(2017) [116].

Given the high temperatures of the cladding expected at CHF, it becomes crucial to understand the materials' surface chemistry when this event occurs as it would provide the chemical nature of the oxides formed at the early stage and the impact on the surface energy. These studies would lead to knowledge of oxidation mechanisms and kinetics, ultimately explaining materials' performance. For example, Lee et al. [128] repeated the flow boiling experiment several times using identical test specimens to study the impact of an evolving surface structure on CHF. After ten steady-state experiments, the average contact angle of FeCrAl, Zircaloy-4, and Inconel 600 were decreased from as received contact angle of 69.43°, 76.48° and 73.79° to 53.64°, 64.04° and 55.92°, respectively. The surface roughness of all materials also

decreased after flow boiling experiments. It is believed that the development of an oxide layer on the surface is responsible for the increased wettability, which is supported by contact angle data for oxidized FeCrAl alloys and Zircaloy-4 [128][141-142]. Hence, this opens a research scope to investigate the surface characteristics of ATF candidates and changes in surface chemistry when CHF is reached.

In this research, the mechanical properties, microstructure, surface characteristics, and surface chemistry for ATF candidates, including FeCrAl alloys and Cr-coated Zircaloy-4, were investigated before and after flow boiling CHF testing and compared with the standard Zircaloy cladding. The mechanical properties such as hardness, adhesion strength for the coated samples, and compression strength were measured by different mechanical testing methods for an initial assessment of the materials' characteristics and coating integrity. Furthermore, the materials' surface topography was assessed using contact profilometry atomic force microscopy (AFM). The materials were also characterized using scanning electron microscopy (SEM), energy dispersive spectroscopy (EDS), and X-ray diffractometry (XRD). Surface wettability was acquired by performing contact angle measurements. The dynamic wetting characteristics of all samples were studied by liquid-spreading experiments. The environmental aging effect of surface wettability with time, particularly for Cr-coated Zircaloy, was measured by tracking the contact angle with time and correlated that with the evolution of their surface chemistry studied using XPS. Finally, after flow boiling CHF testing, detailed surface chemistry analysis carried out by XPS depth profiling evidenced various oxides at different depths. Thus, the results presented throughout this dissertation will open a scope to perform thermal-hydraulic experiments and simulations with taking surface parameters into account for more accurate assessment of heat transfer in LWRs, which could help the nuclear industry make progress on next-generation reactors having accident tolerant fuel cladding materials.

1.3 Research Objectives

The attractive properties of Zirconium-based alloys such as; good resistance to corrosion under the operating conditions of a pressurized- or boiling-water reactor, low absorption cross-section of thermal

neutrons with limited irradiation growth and creep make them well suited for their application as nuclear fuel cladding and structural components in conventional light water reactors [143]. However, the aggressive oxidation and significant heat production of Zr-based alloys in a high-temperature steam environment could significantly increase the risk of explosion caused by hydrogen gas, as seen in the Fukushima nuclear reactor accident [2-3]. As a result, issues regarding nuclear plants' safety during severe accidents and natural disasters were raised, and solutions were discussed. Among various approaches suggested to enhance safety, replacing current Zr-based alloys for fuel cladding with advanced ATF materials exhibiting lower oxidation rates can be the solution [4-6]. While research on ATF initiated and tremendous progress has been accomplished on materials development and manufacturing processes, evaluating thermal-hydraulic characteristics of these advanced cladding concepts is also an essential consideration for finalizing and implementing the ATF concepts. CHF, also known as a departure from nucleate boiling, provides safety margins for LWR operations [93]. CHF is a function of operating conditions, system geometry, and it may also be affected by the surface properties. Furthermore, materials' temperature abruptly increases at the CHF point, leading to the evolution of surface composition and topography. Thus, it becomes important to understand the materials' surface chemistry when this event occurs as it would provide the chemical nature of the species formed at the early stage of oxidation at CHF. *The objective of this project is to investigate the effects of surface characteristics of the ATF on their thermal-hydraulic performance and assess their evolution when subjected to environmental exposure and flow boiling CHF testing.* Four specific aims are proposed to achieve this goal:

1.3.1 Investigation of surface characteristics of as-manufactured ATF cladding materials.

The first step of this research aimed to explore different ATF fuel candidates as an alternative to standard Zircaloy cladding materials. ATF cladding materials must improve fuel reliability and safety during accident scenarios in water-cooled reactors [5]. These ATF cladding should also perform comparable or better than the current zirconium alloy cladding under reactor normal operating conditions. The CHF is an essential aspect of the materials' thermal-hydraulic performance of materials that needs to

8

be investigated to safety margins, where materials' surface parameters may affect it. This work investigates several ATF candidates' surface characteristics, microstructure, and mechanical properties using various advanced materials characterization techniques. The ATF claddings included: (1) a Cr-coated Zircaloy-4 produced by both plasma-assisted physical vapor deposition (PAPVD) (coating thickness ~4-5 μm), (2) the FeCrAl alloy APMT, (3) the FeCrAl alloy C26M, and the baseline conventional Zircaloy-4 and Zircaloy-2.

Tasks:

1.3.1.1 Characterization of FeCrAl alloys and Zircaloy-2

1.3.1.2 Effect of Cr-coating on surface characteristics of Zircaloy-4

1.3.1.3 High-temperature wettability measurements

1.3.2 Surface modification and the evolution of ATF cladding surface under environment exposure.

ATF cladding surfaces were modified with different levels of surface roughness by either grinding procedures of the substrate or the final coating. For example, in the chromium-coated Zircaloy-4 produced by PVD, the substrate was modified by mechanical polishing, and the surface served as a template to the coating leading to different roughness parameters. Similarly, surfaces of FeCrAl alloys were polished to understand the relationship between surface morphology and wetting characteristics. Cr-coated Zircaloy-4 and FeCrAl specimens were exposed to a humid environment and normal air at atmospheric conditions. The impact of environmental exposure on the materials' surface wettability and topography was investigated. Furthermore, the surface chemistry was evaluated to elucidate the implications for wettability and topography.

Tasks:

1.3.2.1 Characterization of ATF materials after surface modification

1.3.2.2 Ambient aging effect and XPS investigations

9

1.3.3 Microstructure and surface characteristics evolution of ATF after flow boiling testing

This objective focuses on understanding the evolution of ATF candidates' surface characteristics, microstructure, and mechanical properties when exposed to the CHF in flow boiling testing. The ATF claddings included: (1) a Cr-coated Zircaloy-4 produced by PVD (coating thickness ~5-6 μm) and cold-spray (coating thickness ~25-30 μm), (2) the FeCrAl alloy APMT, (3) the FeCrAl alloy C26M, and the standard Zircaloy-4. At CHF, a continuous vapor film develops on the surface, resulting in a sudden and significant reduction in the local heat transfer coefficient and a dramatic increase in the cladding surface temperature. It becomes crucial to understand the materials' surface chemistry when this event occurs as it would provide the chemical nature of the oxides formed at the early stage. These studies would lead to knowledge of oxidation mechanisms and kinetics, ultimately explaining materials' performance.

Tasks:

1.3.3.1 Surface characterization for post-CHF Cr-coated Zircaloy-4

1.3.3.2 Study of microstructure and surface characteristics for pre- and post-CHF FeCrAl samples

1.3.3.3 Effect of ramp heating on the microstructure and surface chemistry of APMT FeCrAl

1.3.4 Comparison of the experimental results with preliminary results obtained from RELAP5-3D

Thermal hydraulic experimental data for standard Zircaloy taken at atmospheric pressure using CHF testing facility was compared with computational thermal-hydraulic analysis performed using RELAP5-3D. An input deck and nodalization of the experimental test section was developed to model the experiments. The boundary conditions of the RELAP5-3D model, including the inlet coolant temperature, the outlet pressure, and the mass flow rate, were set to be consistent with those in the experiment. The cladding surface temperature profiles were obtained using RELAP5-3D simulation and compared against the CHF experimental results to check the model accuracy.

In this study, we quantitatively investigated the ATF cladding surface characteristics, their stability when exposed to normal humid environments (STP), and their evolution when subjected to CHF boiling

10

tests. Results showed that the wettability and topography of ATF cladding surfaces altered because of the dynamic change of the materials' surface chemistry due to environmental testing conditions (the type of coolant, temperature, pressure) and testing their testing into flow boiling facility. This work will provide a foundation for future experimental and computational studies assessing the thermal performance of ATF in full-scale systems taking into account their surface characteristics.

This dissertation of organized as follows: in Chapter 1 the motivation and research objectives behind this work are explained. In chapter 2, a detailed description of accident tolerant fuels, their need, and selection of ATF candidates' materials is provided. Furthermore, this chapter highlights properties of selected materials and different surface characteristics, which may potentially impact their thermal-hydraulic performance. Chapter 3 is an overview of the various material characterization techniques used in this study. Chapter 4 shows the surface characteristics of both FeCrAl alloys, APMT and C26M, and compares them with standard Zircaloy-2 and Zircaloy 4 cladding material. Additionally, the surface characteristics of Cr-coated Zircaloy-4, manufactured by PAPVD technique, were investigated. In Chapter 5, long tubes of Zircaloy-4 were coated using two different coating technologies, PVD and Cold Spray, and then characterized using advanced material characterization techniques. More importantly, this chapter also describes the influence of the plasma treatments and environmental aging on the wettability at atmospheric conditions of the coated Zircaloy by investigating the evolution of their surface chemistry. In Chapter 6, the evolution of the surface characteristics, microstructure, and mechanical properties of ATF candidates such as Cr-coated Zircaloy-4 produced by PVD and cold-spray, APMT, C26M, and the standard Zircaloy-4 were studied when exposed to the CHF in flow boiling testing. In Chapter 7, cladding surface temperature obtained from the flow boiling experiments is compared with predicted surface temperature from RELAP5-3D. Finally, in Chapter 8 outlook, conclusions and the future work of this project are presented.

Chapter 2: Background and Significance

2.1 Why ATF?

Nuclear power has proven to be a reliable, environmentally sustainable, and cost-effective source of large-scale electricity. In a nuclear power reactor, the heat released during the fission of uranium in the fuel is captured by the water surrounding the fuel rods to produce steam, which is used to spin the turbines to generate electricity. The water that extracts the heat generated by the nuclear fission reaction is called the coolant. The fuel is urania or uranium dioxide (UO_2), approximately 10 mm tall and 10 mm diameter pellets piled about 4 m high inside vertical metallic tubes called the cladding. Currently, zirconium-based alloys such as Zircaloy-4, Zircaloy-2, M5, or Zirlo are mainly used as the cladding for LWRs [7][30][144-145]. Zirconium alloys have adequate resistance to corrosion in high-temperature water under the standard operating conditions of pressurized water reactors (PWRs) and boiling water reactors (BWRs) at near 300 ºC [145]. However, the corrosion resistance in water and steam of zirconium alloys decreases rapidly as the temperature increases above 400 ºC. During the plant blackout events at the Fukushima Daiichi nuclear power stations, the water temperature inside the reactor increased to above the normal operation condition values for the reactors, and the zirconium alloys reacted rapidly with water and steam forming hydrogen gas and releasing large amounts of oxidation reaction heat to the environment [1]. The highly exothermic oxidation reaction of zirconium cladding with steam can be written as follows:

$$Zr + 2H_2O \rightarrow ZrO_2 + 2H_2 + heat \qquad (2.1)$$

From this equation, we can see that zirconium oxidizes into zirconium dioxide (zirconia), producing hydrogen and heat due to the exothermic reaction. This can become dangerous in a loss of coolant scenario for several reasons. First, it has been shown that as temperature increases, the zirconium/steam oxidation reaction kinetic increases parabolically [146]. Second, as oxidation occurs, hydrogen is produced. Hydrogen is very reactive with oxygen, and in the case of a reactor vessel leak, it can combust with oxygen in the outside air causing an explosion and the subsequent release of radionuclides to the

13

environment. Additionally, the increase in hydrogen concentration and the increase in temperature can increase hydrogen diffusion into unoxidized portions of the cladding, resulting in embrittlement and an increased potential for cladding failure and the subsequent release of radionuclides [6]. After almost seven decades of successfully using zirconium alloys in reactors, the international nuclear materials community is now searching for safer and more resistant alternative materials for fuel components.
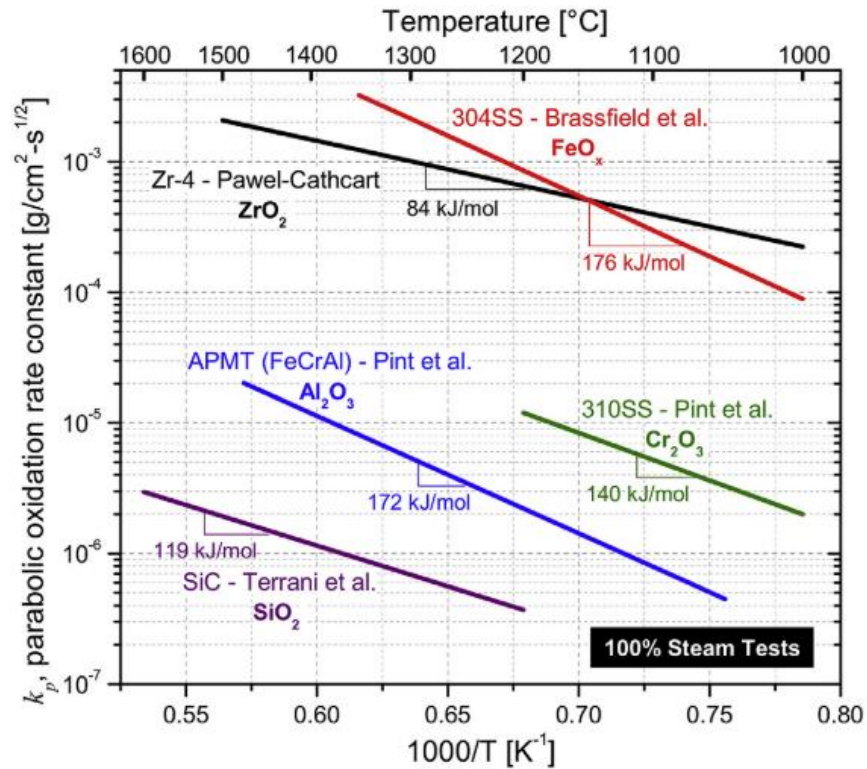
Figure 2.1 Parabolic oxidation rate for various cladding materials and their resulting oxide in steam as a function of temperature [24][143][147].

Since reducing the rate and total amount of heat generated from steam oxidation is the basis behind the development of ATF cladding materials, it is worth asking whether there are materials with significantly higher steam oxidation resistance. After the Fukushima accident, various research and development programs were launched worldwide to address this question. Early studies showed that although high-temperature steam is a far more aggressive environment than dry O_2 [148], the three

14

conventional classes of protective oxide films, namely, chromia, alumina, and silica, may be utilized to

protect the underlying materials. This is shown in Fig. 2.1, the parabolic oxidation rate constant, for

various cladding materials and their resulting oxide films when exposed to steam at elevated

temperatures. The graph shows that the reaction rates for Zr-based cladding are very high among all

tested materials. On the other side, both alumina (for APMT) and silica (for SiC) scales have lower

reaction rates and can remain protective to much higher temperatures.

Improved Clad Reaction Kinetics with Steam

❑ Heat of oxidation
❑ Oxidation rate
❑ Hydrogen bubble and explosion
❑ Hydrogen embrittlement of the clad

Enhanced Retention of Fission Products

❑ Gaseous fission products
❑ Solid/liquid fission products

Improved Fuel Properties

❑ Lower operating temperatures
❑ Clad internal oxidation
❑ Fuel relocation/dispersion
❑ Fuel melting

Improved Cladding Properties

❑ Clad fracture
❑ Geometric stability
❑ Thermal shock resistance
❑ Melting of the cladding

Figure 2.2 Major issues that need to be addressed in establishing accident-tolerant fuel attributes

[5].

In addition to maintaining good performance under normal operating conditions, there are four main

desired attributes of ATFs, as outlined in Fig. 2.2. Firstly, during a loss of coolant accidents and station

blackout events, suppressed oxidation compared to Zr alloy cladding in the presence of hot steam would

simultaneously minimize hydrogen generation and enthalpy input. Also, the accident tolerant fuel system

should exhibit good dimensional stability and fission product retention up to temperatures above 1200 °C

in order to maintain a controllable and coolable core geometry without a significant release of radioactive

materials. For reactivity-initiated accidents (RIAs) scenarios that produce a relatively rapid temperature increase of short duration, a key attribute of the cladding is the resistance to rupture via pellet-cladding mechanical interaction [149]. This implies cladding materials with improved ductility and toughness at moderate to high temperatures compared to Zr alloys. Finally, fuel forms that enhance the confinement of fission products under various accident scenarios are desirable.

2.2 Material Selection

The ATF program's mission is to develop fuel cladding materials with the primary objective of enhancing oxidation resistance and ultimately suppressing hydrogen production in severe accident conditions. Fig. 2.3 shows the two concepts being considered as hydrogen-suppressing cladding system: surface-modified Zr alloy [150-151] and developing new non-zirconium cladding [14][150]. There are some differences between these thoughts and result in different consequences. For example, coating the Zircaloy cladding will inherit the mechanical properties of Zircaloy cladding in general. In contrast, a new non-zirconium cladding material, such as Fe-based alloys, will lead to different mechanical behavior. In any case, these methods' primary objective is to solve the oxidation reaction and hydrogen generation problems at high temperatures. At present, universities [36][74][152], national labs [150][153], relevant industries [88][154], and other cooperators are working together on this promising technology via experiments or simulations. Many ATF cladding concepts, such as (a) different coatings [44-45][63][67][155-157], (b) iron-based alloys [80][158], and (d) ceramic matrix composites SiC cladding [25-27][159] are being considered to improve on the performance of current Zr-based alloys.
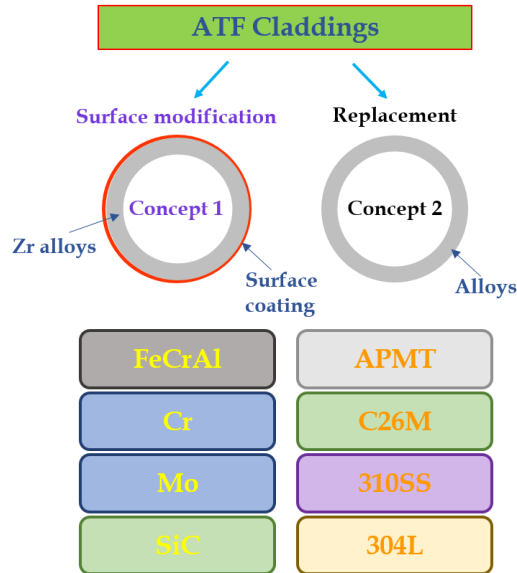
Figure 2.3 Schematic view of the two ATF cladding concepts.

High-performance stainless steels offer the potential for improved strength and oxidation resistance compared to existing Zr alloys over a broad temperature range [14]. However, issues to be resolved include the effect of higher thermal neutron absorption cross-section on fuel enrichment and other operational requirements, potential enhanced susceptibility to stress corrosion cracking in LWR primary coolant water chemistries, the impact of radiation hardening and embrittlement on cladding performance under normal operating conditions, mitigation of the increased tritium burden associated with bare steel-clad, and pellet-cladding mechanical interaction behavior under RIA conditions [14]. Silicon carbide ceramic composites are potential cladding material candidates due to their low thermal neutron absorption cross-section, retention strength up to very high temperature, good radiation resistance, and good oxidation resistance in air and steam up to temperatures of at least 1600 °C [160]. While potentially very attractive, this class of materials has yet to find engineering familiarity in design and application. Refractory alloys based on Nb, Mo, Ta, or W offer the potential for significant improvement in high-temperature strength compared to Zr alloys. Nevertheless, these refractory alloys generally exhibit poor behavior in high-temperature oxidizing environments [161]. Thus, in this study, we have focused on

17

different types of FeCrAl alloys, APMT and C26M, Cr-coated Zr-4 coated using different coating techniques such as PVD and Cold Spray.

2.2.1 FeCrAl alloys

As a candidate cladding material for LWR, the iron-based FeCrAl has been successfully investigated in some industries where high-temperature oxidation is needed, such as water-vapor-containing environments in fossil fuel energy plants [7][162]. The FeCrAl/UO_2 fuel rod is compatible with current large-scale production technology. A series of different FeCrAl alloys are developed with element compositions of Fe + (10-22) Cr + (4-6) Al + (2-3) Mo + traces of Y, Hf, Zr, etc. Additions of Cr and Al are essential for improving oxidation resistance at elevated temperatures by forming protective oxide layers. Higher content of Cr in the alloy can be beneficial for the high-temperature oxidation resistance via supporting the stability of Al_2O_3 in both hot water and steam environment [163]. However, its existence would bring potential embrittlement to the alloy under normal operation [164]. Similarly, higher Al content would also enhance the resistance to oxidation due to the formation of protective Al_2O_3 on the cladding surface in steam environments but increases the difficulty of cladding manufacturing [165]. In this research, we focused on two FeCrAl alloys, APMT (Fe-21Cr-5Al-3Mo), developed by GE Research and C26M (Fe-12Cr-6Al-2Mo), developed by Oak ridge national laboratory (ORNL). The C26M was manufactured in the traditional way of melting, casting, forging, and rolling, and APMT was produced using powder metallurgy plus extrusion process. Fig. 2.4 shows an etched metallographic cross-section of APMT and C26M tubes. The microstructure of APMT shows mostly smaller grains in the order of 10 μm. On the other hand, the microstructure of C26M shows comparatively larger grains.
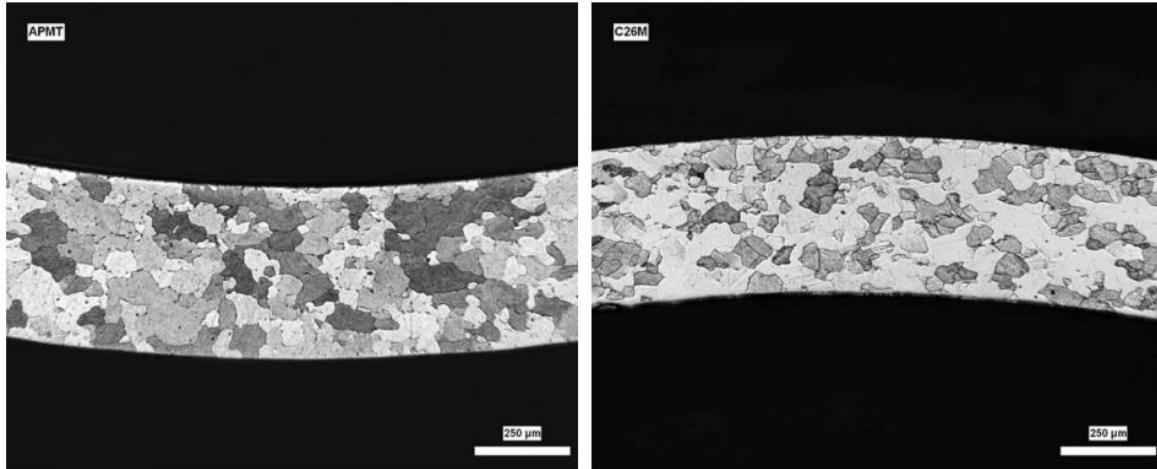
Figure 2.4 Microstructure of thin-walled tubes of APMT (left) and C26M (right) fabricated using industrial practices [22].

Fig. 2.5 shows the process of how FeCrAl alloys behave in a superheated steam environment. The protection of the alloys is given by the formation of a chromium-rich oxide on the surface that is thermodynamically possible under normal operation conditions and up to 1000 °C. However, as the temperature increases beyond 1000 °C, alumina forms between the metal and the chromium oxide layer. Eventually, in the presence of steam, the chromium oxide layer volatilizes, and the alumina layer remains on the surface protecting the alloy from further oxidation up to its melting point (~1500 °C) [22]. The behavior of FeCrAl in different corrosive environments has been widely investigated. The comparison during the high-temperature steam oxidation experiment, FeCrAl alloy demonstrated higher oxidation resistance than Zr-2, Zr-4, 304SS and 310SS alloys [153]. Pint et al. [166] reported a thin layer of alumina formed for FeCrAl alloy (APM with 20% Cr) at 1400-1500 °C in steam and air environment compared to the thick zirconia layer of Zircaloy-4. The effect of atmosphere and temperature on oxidation film of FeCrAl during long-time oxidation showed that α-Al_2O_3 could still protect the matrix and the aluminum oxide grows outward after oxidation at 900 and 1200 °C for more than 30 days [167]. Park et. al. [78] reported extremely low weight change for FeCrAl alloy compared to Zircaloy tested in pressurized 360 °C water for up to 500 days, equivalent to 1200 °C for 3000 sec in a steam environment.

Similar uniform corrosion behavior of FeCrAl alloys was reported with negligible thickness loss after one year of LWR water corrosion in the absence of irradiation [168]. The fuel performance modeling using BISON simulations for both light water reactor normal operation and loss-of-coolant accidents showed that the FeCrAl behaves similarly to Zircaloy-4 with the advantage of improved oxidation performance [169]. Rebak et. al. [170] have studied and explained how the oxide films that FeCrAl forms under the normal operating condition of the reactors (hydrogenated water near 300 °C) and severe conditions. Both FeCrAl alloys, APMT and C26M showed similar oxidation rates in air and steam in the temperature range 800-1300 °C for 2-h and 4-h tests [171].
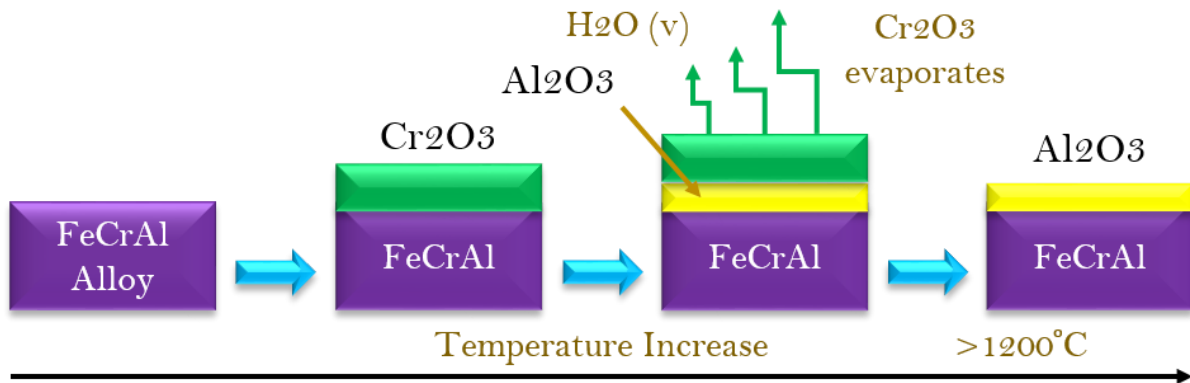
Figure 2.5 Oxidation behavior of FeCrAl in super-heated steam [22].

Fig. 2.6 shows a comparison of mechanical properties for nonirradiated APMT and Zircaloy-2. It is clear that the yield stress of APMT (Fig. 2.6(left)) is approximately four times higher than for Zircaloy-2, the Ultimate tensile strength (UTS) is approximately three times higher, and elongation to failure (Fig. 2.6(right)) for two alloys is comparable [7][89][143]. Lee and Byun focused on the grid-to-rod fretting (GTRF) mechanisms, including looking at FeCrAl-FeCrAl interactions and FrCrAl-Zr interactions under unlubricated (air) and lubricated (water) conditions [172]. They concluded that Zr-based grids could be more susceptible to GTRF than a FeCrAl-based grid when FeCrAl-based rods are used within a fuel assembly [86]. The broad literature has shown that the mechanical properties, such as yield strength,

UTS, and hardness of wrought, ferritic FeCrAl alloys have strong dependencies on test temperature, alloys composition, and microstructure [23][88][173]. The studies on the ductile-to-brittle transition temperature (DBTT) showed that doubling the Al content from 3 wt% to 6 wt% leads to a nearly 100-150 °C increase in the DNTT [88][174].
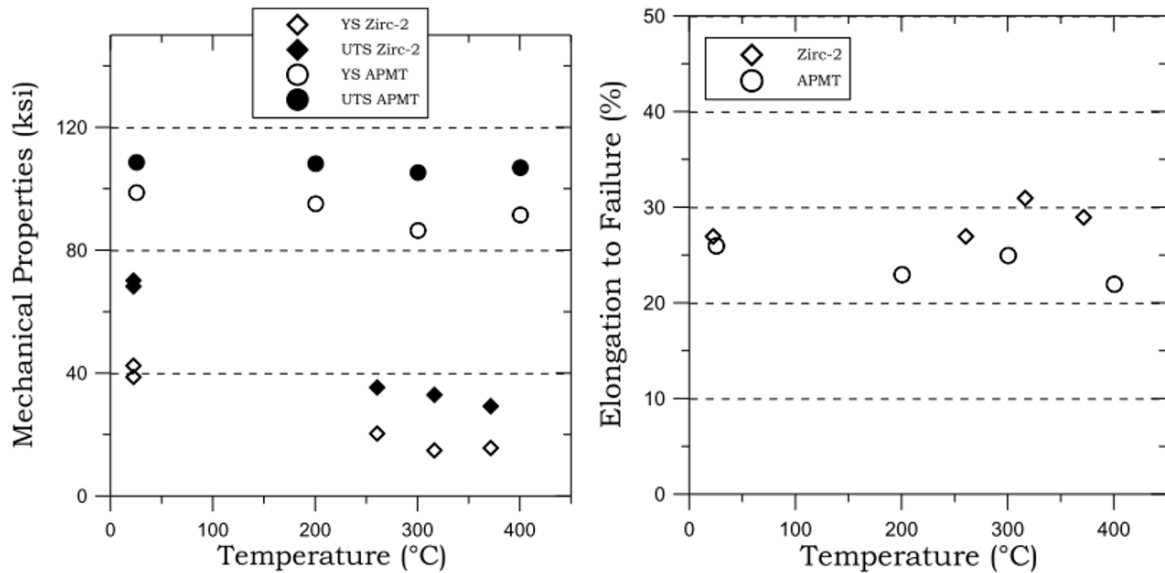
Figure 2.6 Mechanical properties of nonirradiated Zircaloy-2 and APMT [89].

The literature study of irradiated FeCrAl alloys is limited because they have not been used before in nuclear reactors. Irradiation to up to 30 dpa of FeCrAl in the temperature range 380 °C-615 °C showed swellings below the experimental detection limit of 0.1% [175]. Neutron irradiation tests of four noncommercial FeCrAl alloys (3%Al+17%Cr to 5%Al+10%Cr) at 320 °C-382 °C to a nominal dose level of 1.8 dpa showed a slight increase in yield stress with the formation of dislocation loops and alpha prime [80]. However, the total elongation to failure was always higher than 10%, and it remained somewhat constant or increased due to the annealing or recovery of the cold work in the nonirradiated material [80]. The same group irradiated FeCrAl alloys (Kanthal APMT and Alkrothal 720) in the temperature range of 334 °C-382 °C up to 1.8 dpa and recorded similar swelling resistance with no observations of voids or cavities in the microstructure as examined using electron microscopy-based techniques [176]. Heavy ion

21

irradiation for a dose of up to 16 dpa at 300 ℃ of two laboratory-made FeCrAl, namely C06M2

(Fe+10Cr+6Al+2Mo+0.2Si+0.05Y) and C36M3 (Fe+13Cr+6Al+2Mo+0.2Si+0.05Y) tube strips reported

a gradual increase in the surface hardness as the dose of irradiation increased; however, the hardness

leveled off between 3.4 dpa and 16 dpa [81].

2.2.2 Cr-coated Zircaloy-4

An immediately obvious and evolutionary approach to ATF cladding is adopting a protective coating

on the surface of Zr-based alloys [30]. Thin coatings are expected to have a minimal effect on the

thermomechanical behavior of Zr-based cladding [74] and the core physics in LWRs [177]. They should

have the potential to enhance the heat transfer characteristics of the cladding [119]. It is necessary that the

coating be adherent to and chemically stable with the Zr-based cladding substrate during normal and

accident conditions. As mentioned before, materials capable of exhibiting high-temperature steam

oxidation resistance are chromia, alumina, and/or silica formers. Therefore, any ATF coating technology

needs to contain at least one of the elements Cr, Al or Si. The most widely explored coating technologies

on Zr-based alloys to date are, Cr metal [35][45][60][67], CrAl [16], and CrN [64]. Among various

coating techniques available, the majority of the work on the manufacturing protective Cr-coatings for

substrate Zr alloys has been conducted using Cold spray and PVD processes [40][45][52-56]. As shown

in Fig. 2.7(left), the PVD is a thin film deposition technique, where a solid material is vaporized in a high

vacuum environment and deposited on a substrate as a pure material or alloy composition coating [55].

Similarly, in the Cold Spray process (Fig. 2.7(right)), powder particles of the coating materials are fed to

a stream of high-velocity media (helium and nitrogen) to achieve the desired kinetic energy. After

particle-substrate impacts occur, this energy deforms the particles and bonds them to the substrate [55].
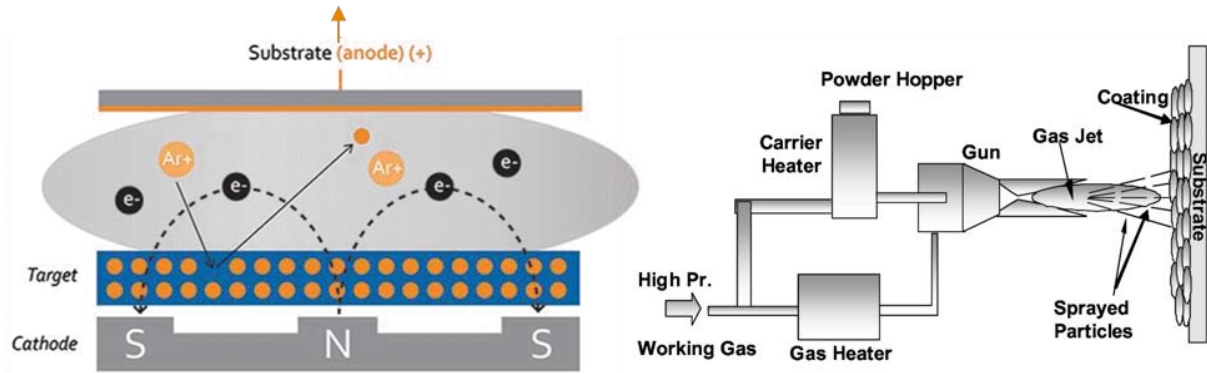
Figure 2.7 Principle of PVD magnetron sputtering (left) and Cold spray (right) coating technologies [55].

The performance of the coated cladding concept is fundamentally focused on the corrosion behavior and mechanical strength under normal operation, as well as the oxidation behavior during accident conditions. Thus, the corrosion/oxidation resistance and strength at high-temperature have to improve more than the current Zr alloys. Significant data exists in the literature on the high-temperature corrosion study of unirradiated Cr-coated Zircaloy. These data are summarized in Table 2.1. In general, all these coatings have been found to provide improved corrosion resistance relative to Zr-alloy cladding.

Table 2.1 Summary of high-temperature oxidation data for Cr-coated Zr cladding.

Coating material and deposition method	Test Description	Performance remarks (noncoated samples as benchmark)	References
Cr-coated M5® by PVD	Ramp test beyond eutectic to 1500 °C	Evidence of localized melting but sample retained it integrity and geometry	Bischoff et. al. [178]

Cr-coated M5® by PVD	Steam between 1000 ℃ and 1500 ℃	Significant reduction in oxidation rate of coated samples relative to uncoated samples	Brachet et. al. [179]
Cr-coated M5® by PVD	Steam at 1100 ℃	Weight gain of coated samples about 10 times lower than uncoated samples	Bischoff et. al. [180]
Cr-coated Zr-4 by PVD	360 ℃, 415 ℃ at 10 MPa for 200 days	Excellent corrosion resistance (tens of times higher)	Brachet et. al. [67]
Flat coupons of Cr-coated M5® by PVD	Steam at 415 ℃ for more than 120 h	For noncoated M5 alloy the mass gain was in order of 160 mg/dm^2, while the mass gain of the Cr-coated coupons was less than 1 mg/dm^2	Bischoff et. al. [180]
Flat coupons of Cr-coated M5® by PVD	PWR type water with less than 10 ppb of dissolved oxygen at 360 ℃ for up to 180 days	For noncoated M5 alloy the mass gain after 180 days was in order of 50 mg/dm^2, while the mass gain of the Cr-coated coupons was 1-2 mg/dm^2	Bischoff et. al. [180]

Cr-coated Zr-4 by Cold Spray	1200 ℃ steam	Weight gain 6 times lower for coated cladding than uncoated cladding	Sevecek et. al. [37]
Cr-coated Zr-4 by Cold Spray	1200 ℃ steam	Half oxide thickness on coated cladding than uncoated cladding	Shahin et. al. [38]
Cr-coating on ZIRLO by Cold Spray	1300 ℃ and 1500 ℃ steam for 5-25 min	Nonsignificant weight gain at 1300 ℃, evidence of surface melting seen at 1500 ℃	Oelrich et. al. [181]
Cr-coating on ZIRLO by Cold Spray	1300 ℃ air for 20 min	Oxide layer thickness was 30 times lower on coated cladding than uncoated cladding	Shah et. al. [62]
Cr-coated Zr-4 by 3D laser coating	Steam at 1200 ℃ for 20 minutes	Oxide layer thickness was 25 times lower on coated cladding than uncoated cladding	Kim et. al. [35]
Cr-coated Zr-4 by CVD	1200 ℃ in air	Weight gain was 4 times lower for coated cladding than uncoated cladding	Michau et. al. [182]

Fig. 2.8 shows the engineering stress and strain curves of the ring tensile and ring compression test. The maximum stress in the ring tensile test is about ten times higher than that of the ring compression test. Although the strength of the Cr-coated samples was somewhat higher than that of the non-coated

samples in both the tensile and compression tests, the variation trend of stress-strain curves was similar between the reference samples and the Cr-coated cladding samples. The Cr-coated layer was cracked at the severely deformed regions after both tests, which could be caused by the brittle characteristics of the Cr layer as well as the influence of the laser treatment [35]. Several other studies have reported similar results for unirradiated Cr-coated Zr cladding. Brachet et. al. [67] measured similar mechanical properties such as elastic modulus, yield stress, UTS, and elongation for Cr-coated M5® and substrate Zircaloy M5® at room temperature and 400 ℃. Similarly, Shahin et. al. [38] reported nonsignificant change in UTS, burst pressure, and burst strain results after Cr-coating on Zr-4 substrate. During fatigue cycling in air and water between 300 ℃ and 312 ℃, fatigue failure was observed significantly earlier in Cr-coated samples (~10,000 cycles) than uncoated samples (~100,000 to 500,000 cycles) [37]. However, the coating has demonstrated extraordinary adherence under thermal cycling at 300 ℃ [35][183]. Park et al. [77] heated Cr-coated Zr alloy samples at 1200 ℃ for 300 s and quenched them with water to 800 ℃. They reported a greater ductility for the coated sample than for the uncoated sample after the quenching test. Several fretting tests have been performed and indicated that Cr-coated Zr cladding exhibits superior wear resistance relative to uncoated Zr [67][178][180][184].
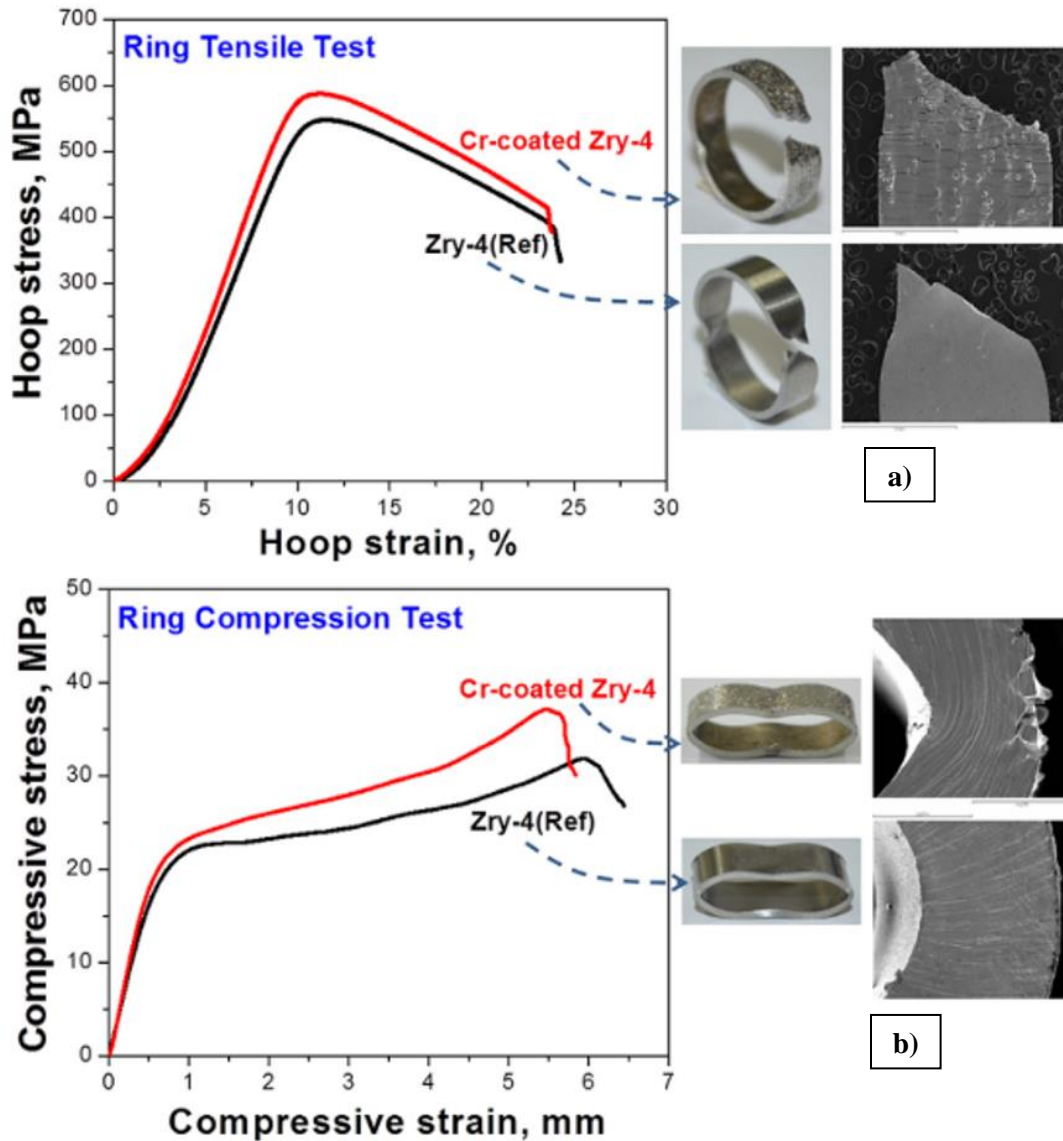
Figure 2.8 Result of ring tensile (a) and ring compression (b) tests of Zr-4 and Cr-coated Zr-4 with the appearance of the tubes after testing [35].

Irradiation test data for Cr-coated Zr cladding is relatively sparse. Wu et. al. [73] irradiated first-generation chromium coated Zr-4 using 20 MeV Kr^{8+} at 400 ℃ with damage at the interface of 10 dpa. They reported good chemical and microstructural stability of the Zr/Cr interface. The radiation resistance of Cr deposited coatings was investigated through the study of void swelling after irradiation with 1.4 MeV argon ions at 400 ℃ to doses of 5, 15, and 25 dpa [41]. The radiation-induced swelling is observed

to be 0.16% under the dose of 5 dpa, and attains 0.66% under the dose of 25 dpa, this being an order of

magnitude lower than the allowable swelling for the core materials of the reactor [41].

2.3 Surface Characteristics and their potential impact on CHF

An accurate prediction of heat removal from fuel elements during accident scenarios is desirable in

the safety analysis of water-cooled nuclear reactors. It is well known that surface parameters strongly

affect both nucleate and transition boiling. Based on the vast literature, the key surface parameters that

can delay a boiling crisis and improve boiling efficiency are surface wettability, roughness, surface

chemistry [97][185]. In general, the wettability of a surface is the ability of a liquid to wet such surface,

and it is represented by sessile droplets of fluids at room temperature on the surface and defined in

Young's equation [186]:

$$\cos \theta' = \frac{\gamma_{SV} - \gamma_{SL}}{\gamma_{LV}} \tag{2.2}$$

Wenzel [186] modified the equation by introducing the roughness factor into the above equation as

following:

$$\cos \theta = r \times \cos \theta' = r \times \frac{\gamma_{SV} - \gamma_{SL}}{\gamma_{LV}} \tag{2.3}$$

Where, $\gamma_{SV} - \gamma_{SL}$ is the adhesion tension, γ_{LV} is the surface tension, θ' is the static contact angle and

θ is the apparent contact angle. The roughness factor (r) is defined as the area of the actual surface over

the geometric surface area, which is a factor that represents the degree of surface roughness. The smaller

contact angle represents a higher surface wettability, and the contact interface between solid and liquid is

extended so that the surface stays wet during the boiling process. Furthermore, roughness is a measure of

the surface texture, measured by profilometry and expressed by roughness parameter Ra, defined as the

arithmetical mean deviation of the assessed profile. Surfaces with a higher degree of roughness exhibit an

increased heat transfer area and more nucleation sites for bubble formation. Hence, to comprehend the

CHF enhancement, these characteristics need to be understood. A summary of the enhancement to CHF

achieved in boiling experiments with surface modifications is listed in Table 2.2.

28

Table 2.2 Effects of surface parameters on CHF.

Authors	Pool boiling conditions	Coating characteristics	Maximum CHF enhancement	Main root causes for CHF enhancement
Jo et. al. [137]	Substrate: Nickel-chrome wire, Electroplating time:0-100 s	Cuprous oxide (Cu_2O), fractal-like nanotexturing	80%	Roughness
Jones et. al. [130]	Substrate: Aluminum Surfaces R_a ranging from 0.027 μm to 10 μm	No coating	100% with water & 200% with FC-77	Roughness
Kim et. al. [136]	Substrate: Copper Surfaces R_a ranging from 0.041 μm to 2.36 μm	No coating	100%	Roughness
Son et. al. [138]	Substrate: SA508, Atmospheric pressure, Work fluid: DI water	SA508, Pre-oxidational surface	140% with bare SA 508	Wettability
Kim et. al. [139]	Substrate: Aluminum, Atmospheric pressure, Work fluid: DI water	Aluminum, Pre-oxidational surface	30%	Roughness
Tetreault Friend et. al. [140]	Method: layer-by-layer deposition technique, Work fluid: saturated water, Atmospheric pressure	SiO_2 nanoparticle coating	110%	Porous structure
Schroeder Richte et. al. [135]	Substrate: Inconel-600, Atmospheric pressure, Work fluid: DI water	Inconel-600 powder coating, particles size 80-100 μm	Not mentioned	Porous structure

29

Hendricks et. al. [131]	Substrate: Al, Cu substrate, Work fluid: water, Method: MAND^{TM} method	ZnO nanostructure, carpet-like, flower-like, unique	255%	Nucleation site densities, bubble dynamic
Seo et. al. [124]	Substrate: stainless steel, Method: Immersive, Layer-by-layer assembly technique, PEI/MWCNT bilayers number are 10, 20, 40, Work fluid: DI water	PEI/MWCNT	94%	Rewetting ability, efficient bubble ebullient
Authors	Flow boiling conditions	Coating characteristics	Maximum CHF enhancement	Main root causes for CHF enhancement
Seo et. al. [187]	Substrate: SS316L tube, Mass flux: 1600–2600 kg/m^{2}s, Method: quenching method, Work fluid: R123 refrigerant, Atmospheric pressure, Inlet sub cooling: 5 °C	Al$_2$O$_3$, nanoparticle-coated surface	17%	Porosity and capillarity
Khanika et. al. [188]	Substrate: copper, Working fluid: water, Mass velocities: 86– 368 kg/m^{2}s, Inlet subcooling: 30/60 °C, Rectangular microchannel	CNTs coating	23% at low inlet subcooling and low mass velocity	Increased heat transfer area

	Substrate: copper, Work fluid:			Higher
SujithKum ar et. al. [134]	DI water, Method: spray pyrolysis technique, Mass flux: 88–248 kg/m^{2}s, Fe: x% (x = 0, 1.8, 3.6, 7.2)	Fe doped TiO$_2$- Al$_2$O$_3$ composite coating	52.39%	roughness and enhanced hydrophilicity and micro-cavity

Furthermore, some studies have reported CHF enhancement after deposition of coatings due to changes in surface characteristics. Fig. 2.9 compiles the results from previous research reported in the literature for Cr- and FeCrAl- based coated surfaces, targeting ATF designs and their performance in CHF testing [95][116-121][126][128]. As seen in the figure, a significant increase in CHF for a Nichrome wire was observed after coating it with chromia nanofluid by boiling deposition, which resulted from a combined effect of surface wettability and surface structure [118]. The same study reported a CHF enhancement of ~88% when the chromia layer was deposited on Nichrome wire using RF sputtering technique. Similar results were reported for Cr-coating on substrate SS316, where an enhancement in CHF of ~ 79% was explained by the mechanism of capillarity wicking [116]. Kim et. al. [120] also confirmed the effect of surface roughness and capillarity wicking on CHF enhancement for Cr-coated SS304L. This work also proved a CHF enhancement of 48% for Cr-coated samples oxidized at 400 °C dry air for 20 days. In a different study, Cr-coated SS316L substrates prepared by DC magnetron sputtering led to 27% CHF enhancement in pool boiling tests due to surface morphology and capillarity wicking [121]. While various studies have reported CHF enhancement after the deposition of Cr-based coating on metallic substrates, others have described the opposite effects. For example, Kam et al. [119] prepared Cr-coated surfaces using electroplating, but the contact angle of the Cr-coated sample was higher than that of both the non-coated stainless steel substrates and Zircaloy-4. Furthermore, the CHF on the Cr-coated specimens was lower than both the stainless steel and Zircaloy-4. Similarly, a small decrease of ~12% in CHF was recorded for Cr-coated ZIRLO produced using the Cold Spray technique. This decrease in CHF was attributed to differences in wettability and thermal properties of the tested

materials [126]. Moreover, CHF was enhanced for the FeCrAl layered surfaces compared to the base 316 SS surfaces. For example, FeCrAl layers deposited at a substrate temperature of 150 ℃ and a sputtering time of 1 h and FeCrAl deposited at a substrate temperature of 600 ℃ and a sputtering time of 1 h enhanced CHF by 42% and 32%, respectively [117]. In a steady-state flow boiling experiment, FeCrAl alloy, with higher wettability, demonstrated a 22% and 14% increase in CHF compared to Zircaloy-4 and Inconel 600, respectively [128]. Amir et. al. [95] studied the effect of surface characteristics on pool boiling CHF for as-machined and oxidized samples of FeCrAl and Zircaloy-4. The resulting CHF values from pool boiling experiments showed nonsignificant CHF value changes for as-machined samples, while oxidized FeCrAl showed almost 39% higher CHF than Zircaloy-4 samples.
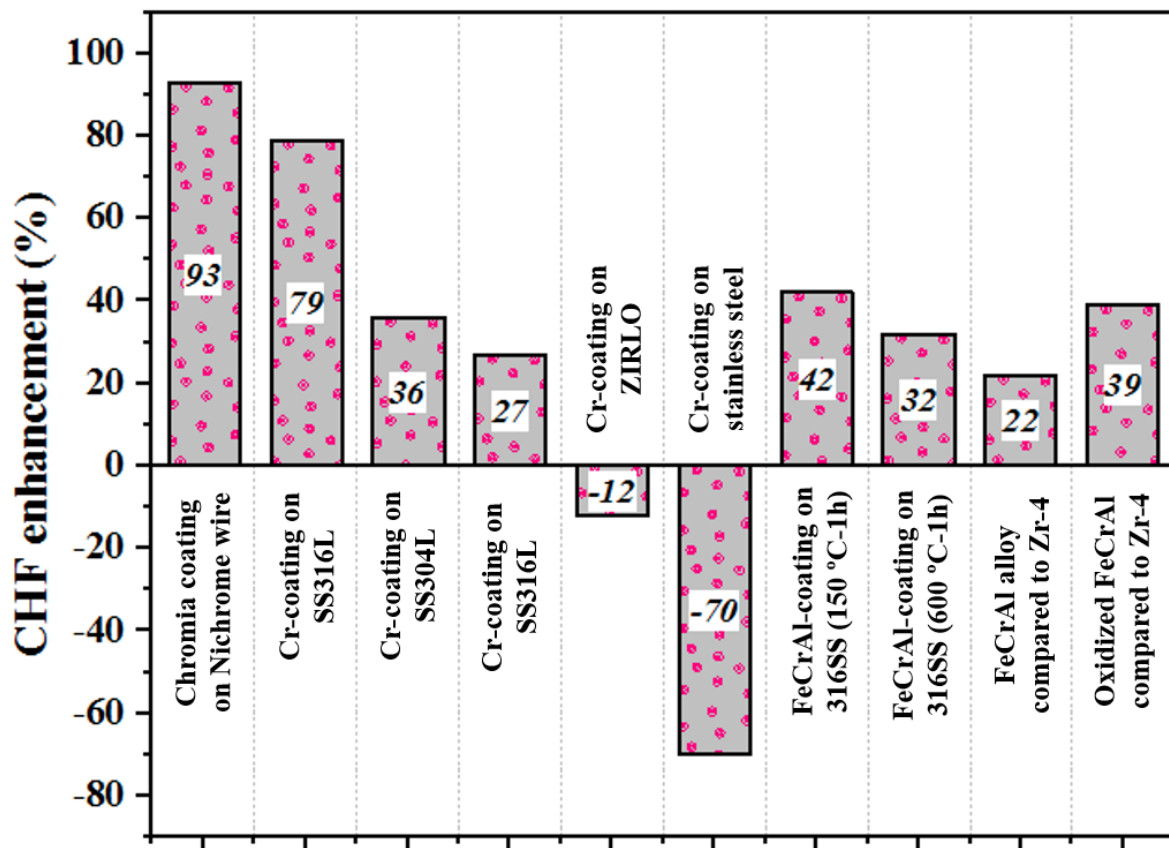
Figure 2.9 CHF enhancement for ATF cladding materials (data summary from the literature).

Chapter 3: Overview of Material Characterization

3.1 Materials and sample preparation

   The samples in this study were commercially available nuclear grade Zircaloy-4, Zircaloy-2, FeCrAls (APMT and C26M), Cr-coated Zircaloy-4. The chemical composition of all tested materials is shown in Table 3.1. Tube segments had an outer diameter of 9.5 mm (wall thickness 0.51 mm), and 10.26 mm (wall thickness 0.4 mm) for Zr-based alloys and FeCrAl alloys, respectively. For coated samples, the Cr coating was deposited on the external surfaces of Zircaloy-4 tubes by using two different techniques, PVD and Cold Spray. Fig. 3.1 shows the step-by-step procedure used to prepare the samples in this work. Before PVD of the Cr coating, the samples' surfaces were modified with three different roughness levels to investigate their effect on the wetting characteristics: a) as-received, b) ground with 600-grit SiC grinding paper, and c) ground with 240-grit SiC grinding paper. During the grinding process, every sample was mounted in a lathe head (Clausing 13" × 25" Geared Head Lathe) and rotated at 40 rpm (CW). Then, after approximately 3 minutes of grinding, radial sanding patterns developed on the tubes' surface. DI water was used as a coolant during the grinding procedure to avoid excessive heating of the sample. Following the surface preparation, the samples were cleaned of all grinding media with ethanol and non-abrasive cloth. A Buehler IsoMet low speed-cutting machine with a diamond saw was used to section a slice of the tube specimen for characterization. The specimens were rigorously cleaned with acetone and DI water to remove solid and organic contaminants by immersing them in an Ultrasonic bath for ~5 minutes and then allowed to dry in air. Finally, the samples were mounted in epoxy for microstructural and chemical analysis using a resin and hardener kit from Allied Chemicals Inc.

Table 3.1 Chemical composition of all tested samples (as obtained from energy dispersive spectroscopy).

%wt.	Sn	Fe	Cr	Ni	Zr
Zircaloy-4	1.65	0.27	0.17	0.007	Balance
Zircaloy-2	1.43	0.49	0.24	0.85	Balance
FeCrAl	Cr	Al	Mo	Y	Fe
APMT	20.53	5.20	4.11	0.88	Balance
C26M	11.73	6.48	2.92	0.74	Balance
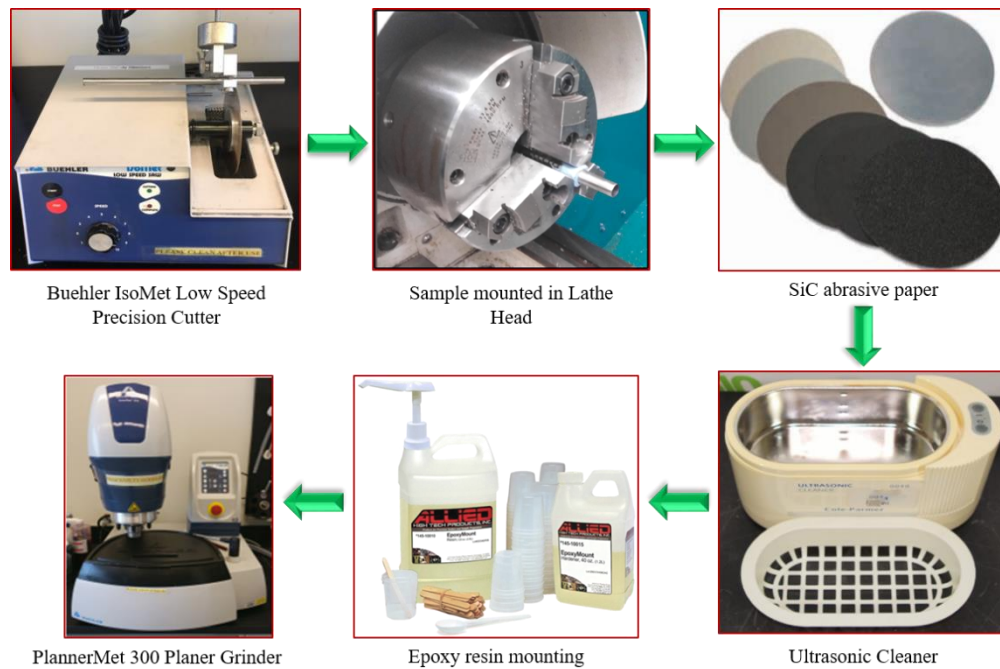
Figure 3.1 Step-by-step sample preparation for all samples.

3.2 Microstructure analysis

Different advanced material characterization techniques studied the microstructure of all samples. X-ray diffraction studies were performed with a Malvern empyrean XRD instrument with a Copper target (voltage 45 kV, current 40 mA, and $\lambda_{K\alpha1}$=1.5406 Å). The XRD patterns were collected at a scan rate and

step size of 3º/min and 0.013º, respectively. A scanning electron microscope (SEM) Phenom ProX at 15 kV and a Hitachi SU-70 FE, 20 kV, both fully equipped with energy dispersive spectroscopy (EDS) and the element identification (EID) were used to analyze oxide thickness for post-CHF samples and morphology of the deposited coatings for Cr-coated samples. For transmission electron microscopy (TEM) characterization, an electron transparent lamella was prepared using a focused ion beam scanning electron microscope (FIB-SEM, Zeiss Auriga, 30 kV). The thin Pt and Au layers were deposited on the sample surfaces to protect the oxide layer from any damage during the milling process. Following Pt-Au deposition, a 10 μm long, 2 μm wide and 10 μm deep lamella was milled and attached to a standard two-post Cu TEM grid. The lamella was then carefully thinned on both sides using the ion beam. The operating conditions of the ion beam were 30 kV voltage and an ion current ranging between 50 pA (for imaging) and 4 nA (for rough milling). SEM images during the milling were collected at 5 kV. High-resolution Transmission Electron Microscopy (HRTEM) observations and chemical analysis of the lamella sample were performed using 200 kV TEM JEOL JEM-F200 coupled with EDS. The TEM images were processed using ImageJ (IJ 1.46r).

3.3 Surface characterization

The static contact angle was measured at ambient conditions using a Rame-hart contact angle goniometer equipped with a NET GmbH 1394 Digital Camera, as shown in Fig. 3.2. The device has an automated dispensing system that allows for accurate control over the droplet volume, assuring measurement repeatability. The American Society of Testing Materials (ASTM) standards for contact angle measurements of metal surfaces provide a detailed measuring procedure, including the necessary number of droplets, droplet volume, and measuring time [189-190]. Thus, according to the procedure, a 5 μL drop of deionized water was gently deposited on the specimens. The static contact angle was recorded within 25 s to ensure the volume of the droplet did not change due to evaporation. A total of fifty measurements were taken throughout the surface to provide a representative value of the contact angle.
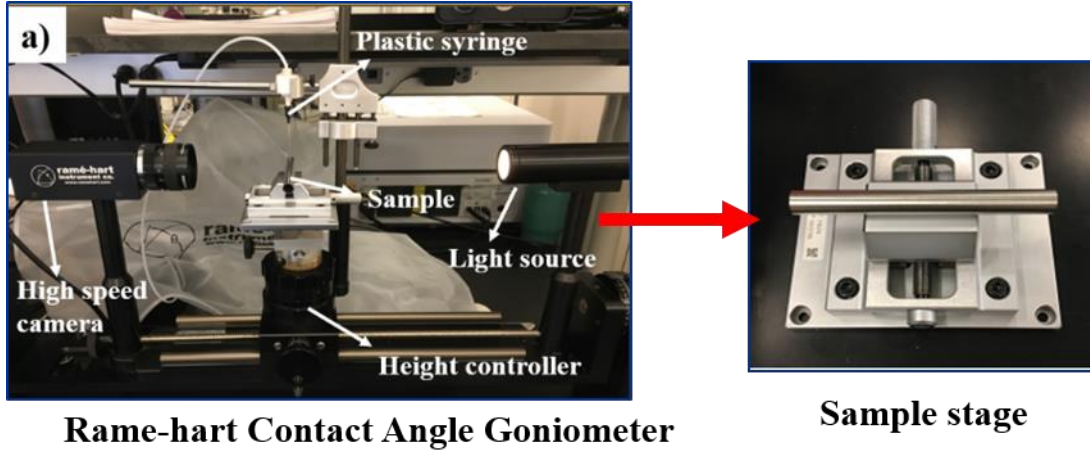
Figure 3.2 Schematic of Rame-hart instrument.

The surface profile of the specimens was measured with a stylus profilometer Mitutoyo Surftest SJ-410 (Fig. 3.3(left)), using a tip of 2 μm radius and 60° tip angle. Several surface roughness parameters, Ra, Rz, Rsk, Rku, and RSm were measured parallel to the axial direction of the tube following International Organization for Standardization (ISO) standards [191-192]. According to ISO standards these surface parameters are defined as following: Ra, the arithmetic average roughness; Rz, the average of the five highest peaks and the five deepest valleys; Rsk, skewness, which is the symmetry of the surface profile about the mean line; Rku, kurtosis, which is the degree of concentration around the mean line and the sharpness of the profile; Rsm, the arithmetic mean value of the width of profile peaks. A graphical representation of these surface parameters is shown in Fig. 3.3 [193]. All scans, each 5 mm long, were recorded from the various specimens at a traverse speed of 0.5 mm/s. The scans were randomly collected for each sample at different locations throughout the tube surface. Each profile was obtained by filtering with a Gauss filter using the cutoff length of 0.8 mm. An Atomic Force Microscope (Bruker Dimension Icon) (shown in Fig. 3.3(right)) operating in tapping mode was also used to study the surfaces' topographies at the nanoscale. The microscope is capable of scanning up to an 8100 μm^2 scan area with a commercial silicon cantilever. An AFM tip with a radius of curvature less than 10 nm, tip height 10-15 μm, a resonance frequency of 320 kHz, and an approximate force constant of 60 N/m was

36

used to scan the materials' surface. The recorded AFM scans were filtered by a Gaussian mask with a cutoff of 2.5 μm to capture surface features at the nanoscale.
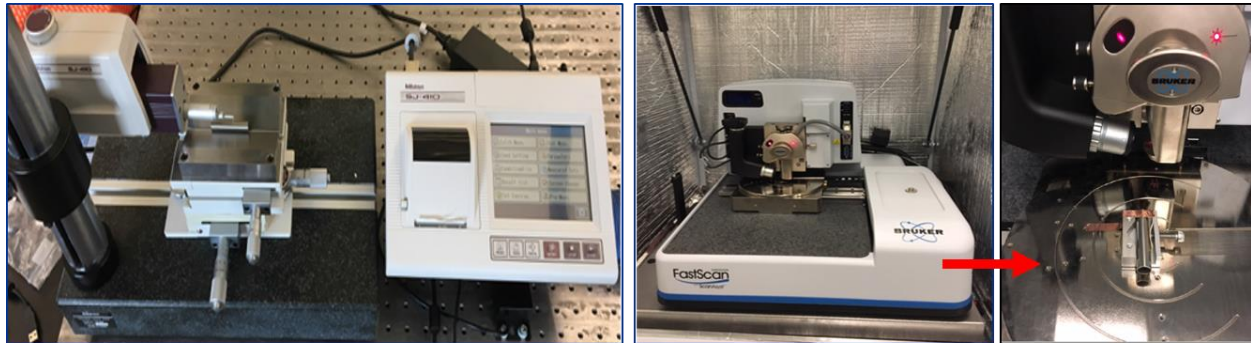
Mitutoyo SJ-410 profilometer   **Bruker Dimension Icon AFM**
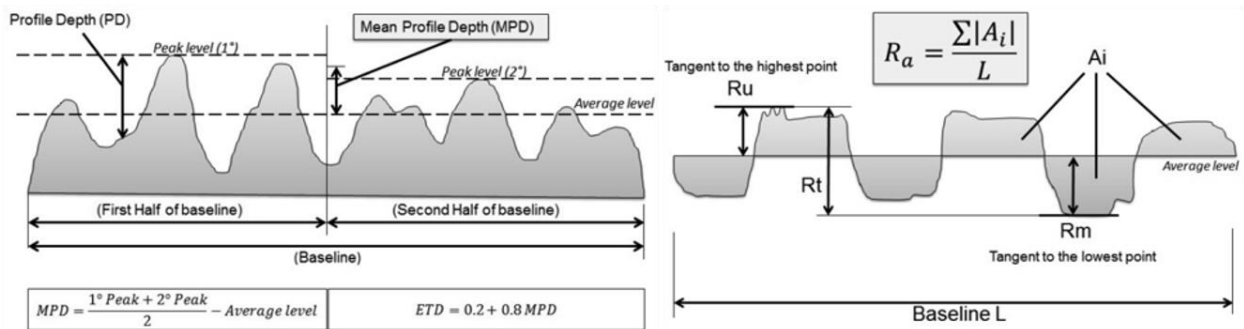
The surface roughness parameters Ra and Rsm
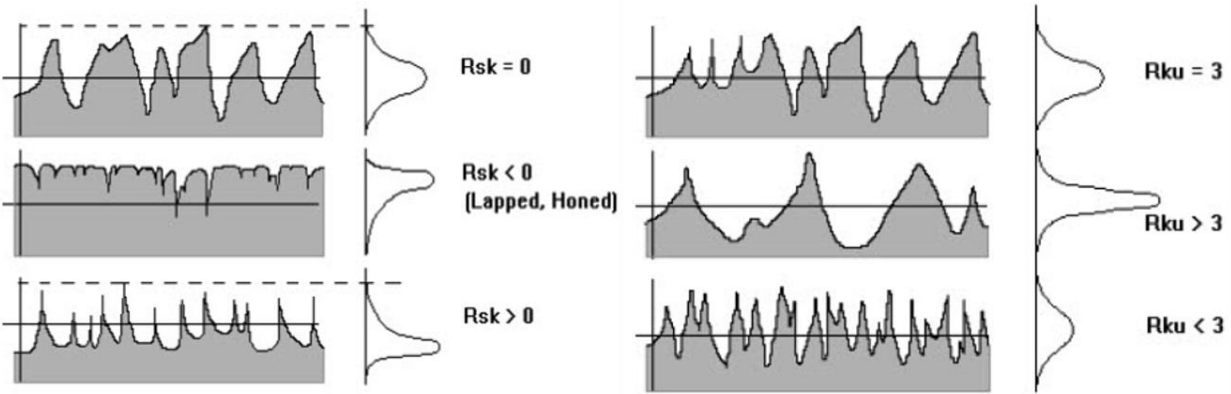
The surface roughness parameters Rsk and Rku

Figure 3.3 Surface roughness measurement procedures with understanding of important surface roughness parameters.

3.4 Surface chemistry

X-ray Photoelectron Spectroscopy (XPS) measurements were collected to investigate the evolution of the samples' surface when exposed to DI water/air and before and after CHF testing. The XPS investigations were performed in a PHI VersaProbe III X-Ray Photoelectron Spectrometer with a monochromated Al k-Alpha X-ray source with a 26-eV pass energy setting. Additionally, post-CHF FeCrAl samples were subjected to incremental argon ion beam sputtering for depth-profiling XPS analysis. The standard operating conditions for the etching were set to a beam energy of 3 keV and a sputter current of 1 μm. The ion beam was scanned in a square raster (9 mm^2) over the specimen surface. Before depth profile data collection, beam current was calibrated using standard SiO_2 film of 250 Å thickness. Several high-resolution spectra of Al2p, Fe2p, and Cr2p were collected using 26 eV pass energy settings and calibrated with the adventitious carbon C1s (284.8 eV). Casa XPS software (Version 2.3.19PR 1.0) was used to evaluate the XPS data with Gaussian/Lorentzian functions and Shirley background set for the deconvolution of the XPS spectra.

3.5 Mechanical testing

A micro-hardness tester, Bruker TUKON-1202, was used to perform hardness measurements following the ASTM standard practices [194-195]. In this study, a set of three applied loads, 25, 50, and 100 gf (0.245 N, 0.49 N, and 0.98 N of applied force, respectively), were used with an indentation dwell time of 15 s. For hardness measurements, tube specimens were mounted in epoxy and polished. Ring compression tests were carried out to assess the mechanical properties of materials. An MTS Insight 30, with 30 kN load capacity, was used to perform the tests. Rings ~4-5 mm long were taken from the tubes, and tested at a loading rate of 1 mm per minute.

Chapter 4: Investigation of Surface characteristics of as-manufactured ATF cladding materials

4.1 Introduction

The surface characteristics of a heater are important, as they affect the dynamics of the boiling heat transfer process, and consequently, the critical heat flux and rewetting are crucial thermal limits for LWRs. For example, surface wettability and roughness determine nucleation site density, bubble departure diameter, and bubble departure frequency [97-98][196]. Therefore, it is essential to quantify the surface parameters of candidate ATF cladding materials to determine their thermal-hydraulic behavior compared to conventional Zircaloy claddings. Ali et. al. [95] reported higher CHF and heat transfer coefficient during pool boiling testing for as machined Fe13Cr4Al than the Zirc-4, which was attributed to higher surface roughness and wettability of Fe13Cr4Al material. However, a negligible effect of the surface characteristics on CHF enhancement was reported for FeCrAl, Zircaloy and Inconel in flow boiling experiment. This study reported that the CHF enhancement was achieved due to various thermal properties of the materials [128]. Furthermore, for optimization and further advances in the claddings' performance, dense and uniform coatings can be applied to Zircaloy materials. For instance, Seo et. al. [117] prepared FeCrAl-sputtered surfaces using PVD sputtering. They primarily controlled the substrate temperature in the FeCrAl sputtering process and obtained different roughness and morphologies. The CHF for all coated surfaces was enhanced due to increased microscale roughness factors. With this in mind, we studied surface characteristic of FeCrAl alloys and Cr-coated Zircaloy-4 prepared using the PAPVD technique. The Cr-coatings were produced on Zircaloy-4 having various surface roughness to investigate its effect on the substrate-coating bond quality. Materials were characterized using various techniques which includes, XRD, SEM and EDS. Surface roughness and wettability were assessed with dynamic wetting by liquid-spreading experiments. Coating was tested with microindentation tests and adhesion property was measured using pull-off tests. In our wetting tests, Cr-coated surfaces showed improved wetting characteristics not only at room temperature but also at PWR temperature and pressure.

Similarly, rough surfaces of FeCrAl alloys are believed to exhibit a strong potential for CHF improvement.

4.2 Material and methods

Two FeCrAl alloys, APMT and C26M, and Zircaloy-2 used in this study were provided by General Electric. The Cr coatings were deposited on the small sections of Zircaloy-4 tubes using an in-house direct current magnetron sputtering system (DCMS) with a Cr target (99.5% purity) acquired from Vacuum Engineering Materials Co. Inc. and a SpinTron gun at the Surface and Coating Engineering Lab (VCU). No buffer layer was used, and the main process parameters used for coating are listed in Table 4.1. Detailed sample preparation and experimental procedures are explained in Chapter 3.

Table 4.1 PAPVD coating process parameters.

Sputtering parameters	Target condition
Target material	99.95% pure chromium
Substrate material	Zircaloy-4
Substrate temperature	Room temperature
Deposition time	4 h
Base pressure	9.6×10^{-7} Torr
Working pressure	6.5×10^{-3} Torr
DC power	100 W
Sputtering gas	Argon (Ar)
Ar flow rate (sccm)	17

Table 4.2 summarizes the characteristics of the samples for both uncoated and coated Zircaloy-4 and the sample identification used herein. Additionally, 2 mm thick flat Zircaloy-4 substrate and Cr-coated Zircaloy-4 coupons with dimensions 1×1 cm^2 were prepared for adhesion studies and high-temperature

surface wettability measurements. The pull-off test was performed to measure coating adhesion properties [197-198]. With epoxy glue (EP11HT Gray acquired from Resinlab), aluminum dollies with a diameter of 10 mm were mounted to the surface of the Cr-coated Zircaloy-4 flat samples. The samples were placed into an oven for 20 minutes at $100°$C to reduce the curing time of the glue. When the glue was cured, a normal force was applied to the dolly's outer tip using an automatic adhesion tester (PosiTest AT-A). The value of adhesion was determined with the load needed to delaminate the coating from the substrate.

Table 4.2 Test samples description.

Sample ID	Conditions
AR-Zr4	As received Zircaloy-4 sample from vendor
600G-Zr4	Zr-4 sample ground using 600 grit SiC abrasive paper
240G-Zr4	Zr-4 sample ground using 240 grit SiC abrasive paper
AR-Zr4-Cr	Cr-coating deposited on "AR-Zr4"
600G-Zr4-Cr	Cr-coating deposited on "600G-Zr4"
240G-Zr4-Cr	Cr-coating deposited on "240G-Zr4"

4.3 Result and discussion

4.3.1 Characterization of FeCrAl alloys and Zircaloy-2

The diffraction patterns of the materials under evaluation are shown in Fig. 4.1. According to peak analysis based on the ICDD database, the FeCrAl alloys (APMT, C26M) have the body-centered cubic (BCC) crystalline structure, while Zircaloy-2 has a hexagonal closed packed (HCP) crystalline structure [143]. The body-centered cubic (BCC) crystalline structure offers higher dimensional stability during neutron irradiation [22][80][83][143][158]. Due to the lower atomic packing density, BCC metal exhibits smaller volume expansion associated with the insertion of an interstitial atom, compared to other crystalline structures [8].
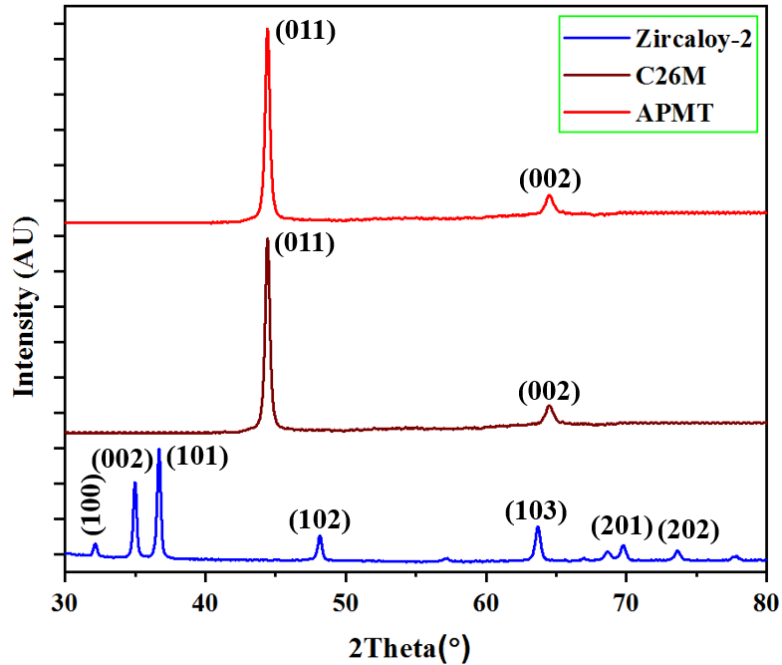
Figure 4.1 XRD patterns for FeCrAl alloys (APMT & C26M) and Zircaloy-2 [199].

Table 4.3 shows the average of one hundred roughness scans collected using contact profilometry for all three different samples. These results indicate that the average roughness values, Ra, for the C26M and APMT are comparable but approximately double that of the Zircaloy-2. The large Rz value of C26M is supported by its small value of Rsk measured, which indicates a larger number of peaks on the surface than valleys. In addition, the C26M sample yielded a large kurtosis value, which indicates a sharp surface profile. The roughness factors r and surface parameter Rsm for all three materials were recorded using AFM and presented in Table 4.3 as an average of three scan values. The largest r was logged for the APMT, while the other two materials have similar values. The AFM scans provided a qualitative assessment of the surfaces under review and validated surface characterization results obtained from stylus profilometry.

42

Table 4.3 Roughness data for APMT, C26M and Zircaloy-2.

Samples	SJ-410 Profilometer					AFM
	Ra (μm)	Rz (μm)	Rsk	Rku	r	Rsm (μm)
Zircaloy-2	0.36±0.04	4.46±1.08	0.01±0.32	4.46±1.79	1.02	0.18
APMT	0.68±0.07	5.94±0.84	-0.47±0.12	3.17±0.29	1.07	0.49
C26M	0.69±0.07	8.59±1.34	-1.05±0.31	6.23±1.76	1.02	0.38

Fig. 4.2 shows SEM images of the surface morphology of as-received APMT, C26M, and Zircaloy-2 with their respective static contact angles. The SEM image of the APMT surface showed less dense (higher Rsm) and large size (higher Ra) micro scratches that resulted in a higher roughness factor (r). On the other hand, the surface of Zircaloy-2 evidenced highly dense (lower Rsm) and small size (lower Ra) micro scratches that resulted in lower roughness factor (r). Despite deep micro-scratches (higher Ra and Rz) for the C26M, its lower roughness factor results from a lower Rsm value for the scanned area. The contact angle measurements quantified the surface wettability. In surface science, the wettability of a surface is most commonly recognized as hydrophilic when its static water contact angle θ is < 90º and is hydrophobic when θ is > 90º [200]. Zircaloy-2 evidenced the higher wettability, represented by the lowest contact angle among the evaluated samples (Fig. 4.2). To understand the lower contact angle value of Zircaloy-2, in comparison to the FeCrAl alloys (APMT and C26M), it is essential to understand the effects of surface roughness on contact angle. Solid surface roughness significantly affects the contact angle and plays an essential role in wetting and spreading processes [201]. The roughness increases the surface's resistance to wetting for moderately hydrophilic and hydrophobic materials [202]. A study of the surface roughness influences the wetting of the solids even at nano-scale demonstrated that an increase in surface roughness, from 6 to 13 nm, will also increase the contact angle of hydrophobic PTEF (poly-tetrafluoroethylene) surfaces and decrease surface wettability [203].
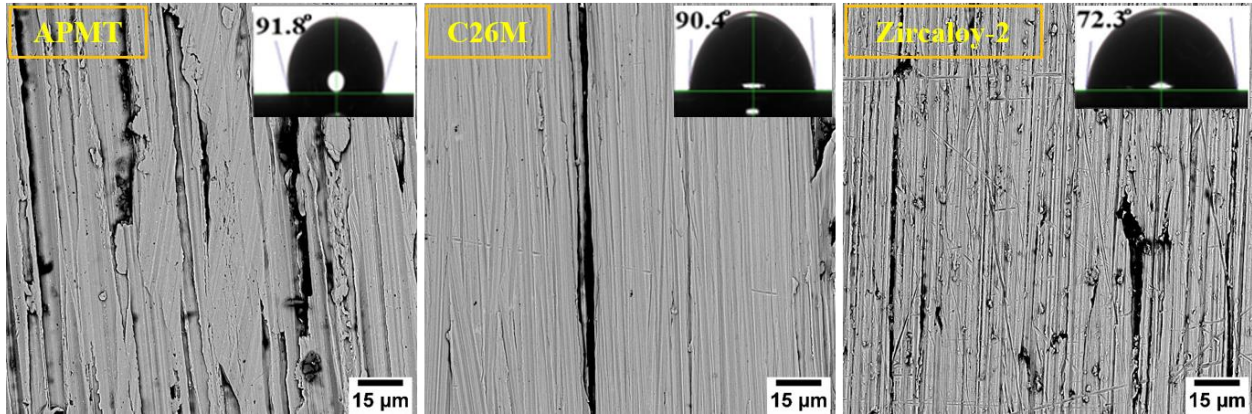
Figure 4.2 Surface characteristics, including the static contact angle and surface morphologies at microscale for all samples [199].

Fig. 4.3(a) shows how spreading contact length was measured in two different directions with respect to the tube's radial axis. For this purpose, the spreading of 5 μl of DI water droplet was recorded for ten seconds using 60 frames/s high-speed camera, and each droplet was analyzed every second to measure contact length using ImageJ. To obtain contact length in the normal direction, a relation between contact length and contact diameter was used. The spreadability results measured in different visualization directions, parallel (left) and normal (right) to the micro-scratches, are shown in Fig. 4.3 (b) for all samples. The Zircaloy-2 showed good affinity towards water with a higher spreading rate among all three samples in the direction parallel to the scratches. The spreading behavior of FeCrAl alloys (APMT and C26M), with almost similar contact angle values, can be understood by previous studies that evidence an augmentation of the contact angle with increasing roughness [204]. The APMT showed lower spreadability because of its higher roughness factor, making it relatively more hydrophobic than the C26M specimen. However, the spreading observed from the normal direction to the micro scratches showed a conflicting trend. The spreading rate for APMT was higher compared to C26M and Zircaloy-2 samples. The Zircaloy-2 showed poor wettability with lower spreading among all three samples. This means that the spreading through the scratches increases as the surface becomes rougher. Deep scratches on the APMT sample surface can be visually confirmed from SEM micrographs. These scratches on the

44

surface improve the capillary wicking effect and hence liquid spreading [136]. As a result, a different

trend was logged for spreading rate measured in different visualization directions.
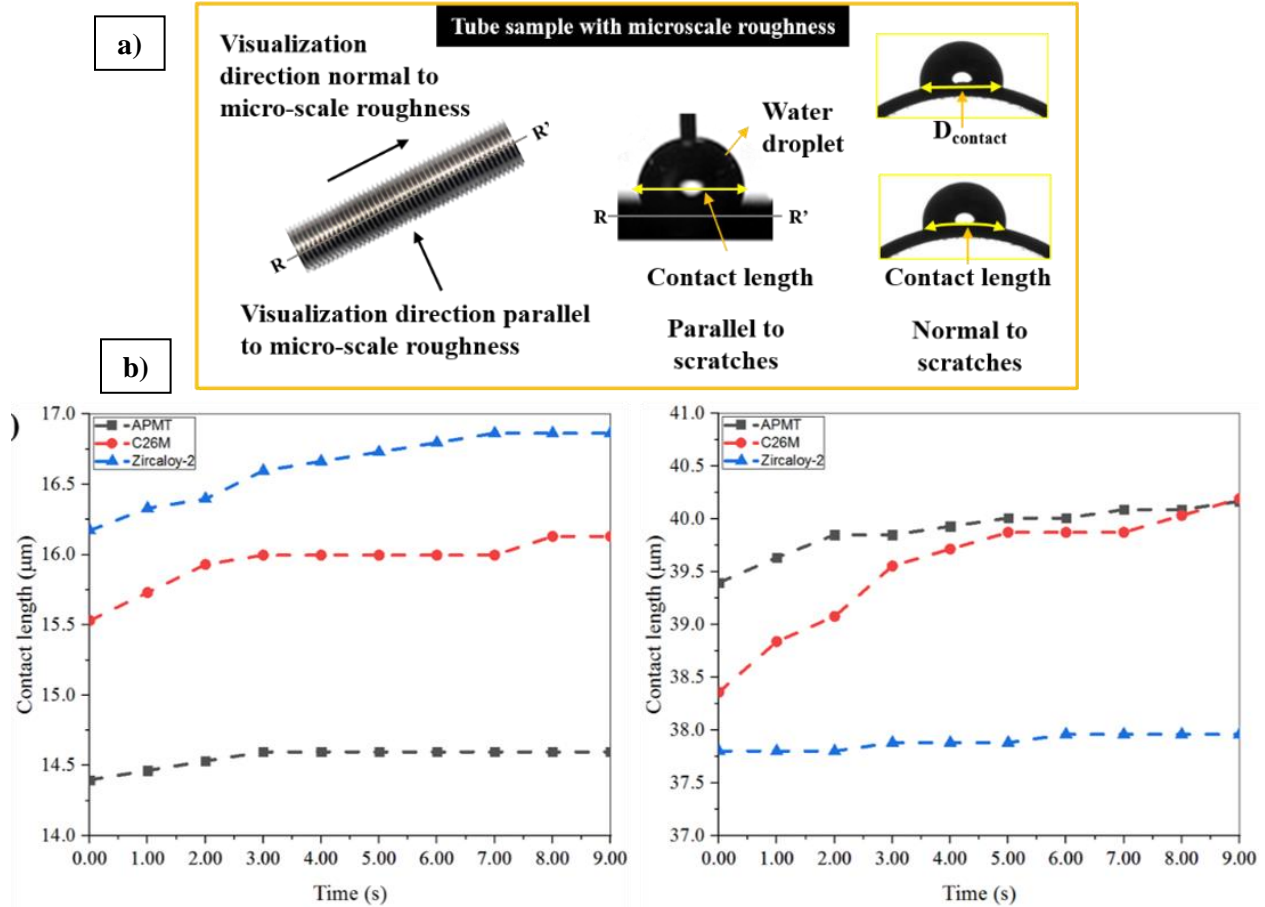
Figure 4.3 Spreadability test: a) Insets showing scratches and visualization direction, and b)

Increasing length with time for all three samples, visualization direction parallel (left) and

perpendicular (right) to micro scratches [199].

4.3.2 Effect of Cr-coating on surface characteristics of Zircaloy-4

The diffraction pattern of substrate Zircaloy-4 and Cr-coated Zircaloy-4 are shown in Fig. 4.4. All of

the diffraction peaks from the substrate correspond the α-Zr phase with a hexagonal closed packed (HCP)

crystal structure [143]. Furthermore, all four additional peaks identified from coating correspond to pure

chromium with a body-centered cubic (BCC) structure [44][205]. The attenuation of the diffracted X-rays causes the decrease in intensity of the peaks associated with Zircaloy-4 due to the presence of the coating.
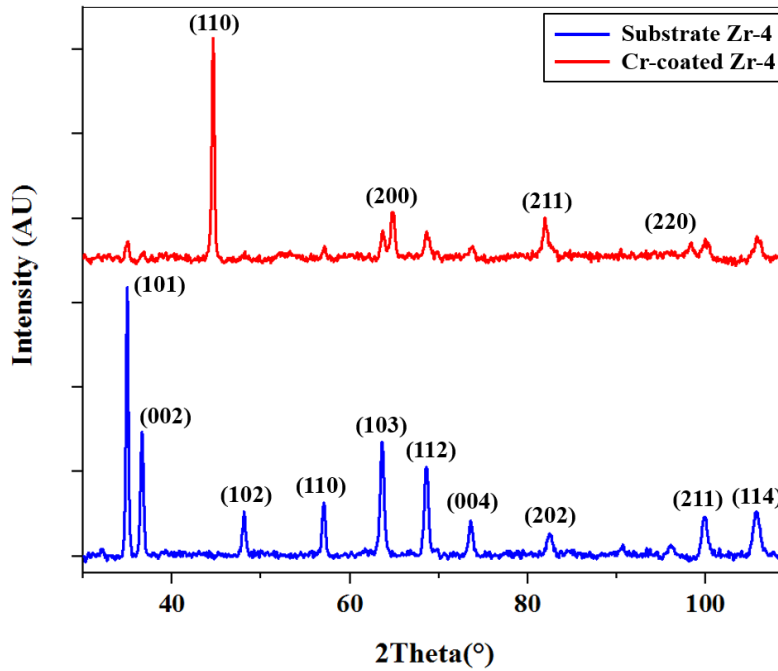
Figure 4.4 XRD patterns for substrate Zircaloy-4 and Cr-coated Zircaloy-4 [206].

Fig. 4.5 shows the SEM images of FIB-prepared cross-sections for the sample AR-Zr4-Cr. The thickness of a Cr layer is about 4 μm, and the Cr coating shows a columnar morphology, a uniform, and dense microstructure, with a well-defined interface. The measured average coating thickness for the other coated samples (600G-Zr4-Cr and 240G-Zr4-Cr) was similar (images not reported here).
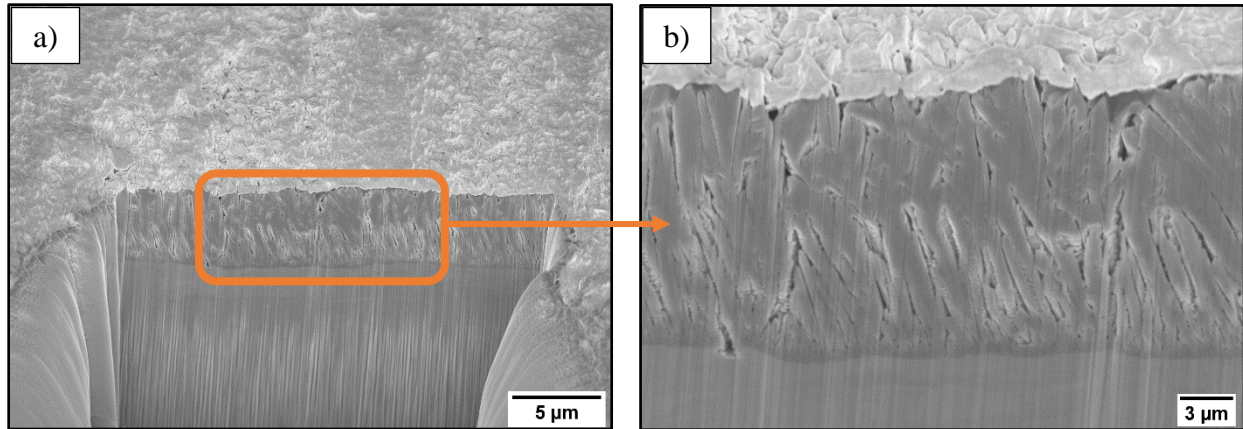
Figure 4.5 FIB cross-section images of a) AR-Zr4-Cr and b) Zoom-in of highlighted region in a) [206].

The results of the microindentation tests are summarized in Table 4.4. The flat samples, AR-Zr4 and AR-Zr4-Cr were measured with three different loads, 0.245 N, 0.49 N and 0.98 N. The hardness values of the substrate sample AR-Zr4 were confirmed with those in the literature [207-208]. As expected, AR-Zr4-Cr showed an increase in hardness at all three applied loads compared to the substrate. It must be noted that Cr coating has a low thickness (4-5 μm). The description of the data as a whole, noting that at the lowest load less effect of the substrate was observed, confirms the observations in the literature where hardness measurements may be strongly influenced by the penetration depth of the indenter relative to the coating(s) thickness [195][209]. The values obtained herein are comparable with those reported in the literature [40][210-212].

Table 4.4 Comparison of results of microindentation for substrate and coating material.

Material	H (GPa)		
	0.245 N	0.49 N	0.98 N
AR-Zr4	2.24±0.25	1.98±0.30	1.17±0.11
AR-Zr4-Cr	4.12±0.57	3.90±0.27	3.37±0.29

All measured roughness data are presented in Table 4.5. The average roughness values varied from 0.399 μm for the substrate, AR-Zr4 up to 0.910 μm for the 240G-Zr4-Cr sample. In general, coated samples evidenced a higher roughness compared to their substrate. Based on the definition of Ra, our results indicate more profound valleys and higher peaks in the surface profile with decreasing grit size during polishing. Similarly, an increase in RSm with increasing roughness suggests that the average distance between two profile elements increases.

Table 4.5 Roughness parameters for all six surfaces tested.

Sample	Roughness parameters (μm)			
	Ra	RSm	Rz	Rq
AR-Zr4	0.399	31.420	2.715	0.494
600G-Zr4	0.496	31.900	3.661	0.627
240G-Zr4	0.776	43.740	6.547	1.001
AR-Zr4-Cr	0.442	32.260	3.245	0.551
600G-Zr4-Cr	0.498	32.860	3.822	0.644
240G-Zr4-Cr	0.910	44.570	7.287	1.172

The quality of deposited coatings was verified by measuring adhesion strength between the coating and substrate using the pull-off test. The influence of substrate roughness on the adhesion strength of the deposited Cr coating is shown in Table 4.6. In the listed samples, the adhesion strength shows an increase with increasing substrate surface roughness. It is believed that a decrease in surface roughness reduces the mechanical interlocking at the interface between the coating and metal substrate. In other words, roughness increases the specific surface area, and it can be effective in improving the adhesion strength [213]. However, the difference among the value of adhesion strength of all tested samples was not remarkable. Optical micrographs in Fig. 4.6 were taken from the dolly used for the pull-off test, revealing

that adhesive failure occurred for all samples. For example, island regions are shown in micrographs (a-c) highlighted by the arrows indicated that the Cr-coating is not completely peeled off from the metal substrate. Large amounts of the coating were peeled off from the AR-Zr4-Cr sample compared to the other two samples, which can be verified from its lower adhesion strength (Table 4.6). Hence, the overall high adhesion strength of the Cr-coating can be noted as the result of this experiment.

Table 4.6 Adhesion strength of all tested samples.

Sample	Adhesion Strength (MPa)
AR-Zr4-Cr	21.79 ± 0.13
600G-Zr4-Cr	25.65 ± 2.90
240G-Zr4-Cr	25.90 ± 0.42
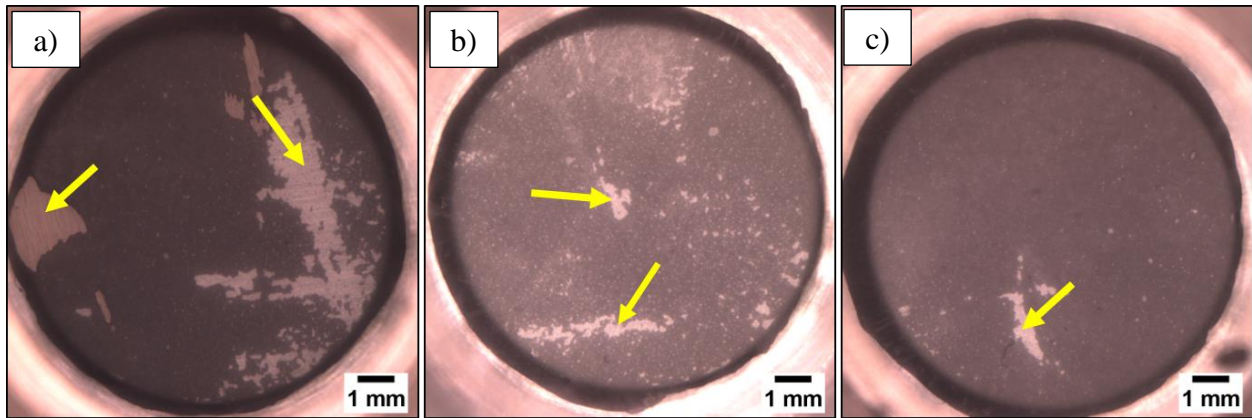
Figure 4.6 Optical micrographs of failed epoxy at the interface of the Cr-coating and substrate Zircaloy-4 for a) AR-Zr4-Cr, b) 600G-Zr4-Cr, and c) 240G-Zr4-Cr after pull-off test [206].

Fig. 4.7 shows the SEM micrographs of Cr-coated Zircaloy-4 tubes with a different surface finish. The SEM micrograph in Fig. 4.7(a) indicates that a uniform and continuous Cr layer has been uniformly deposited on the surface of the Zircaloy-4 cladding sample. As seen in Fig. 4.7(b-d), some scattered islands were observed on top of the layer, which resembles the Stranski-Krastanov (SK) growth mode

49

[214][215]. The roughnesses of Cr-coated Zr-4 shown in Fig. 4.7(b-d) are 0.442 μm, 0.498 μm and 0.910 μm respectively. Fig. 4.7(b) shows a smooth coating except for a small amount of Cr islands on the surface. As the surface roughness increases the peaks and valleys become more evident and a larger amount of Cr islands in the surface is observed, as seen in the micrograph Fig. 4.7(C). The SEM micrograph shown in Fig. 4.7(d) is the roughest of the listed three coatings.
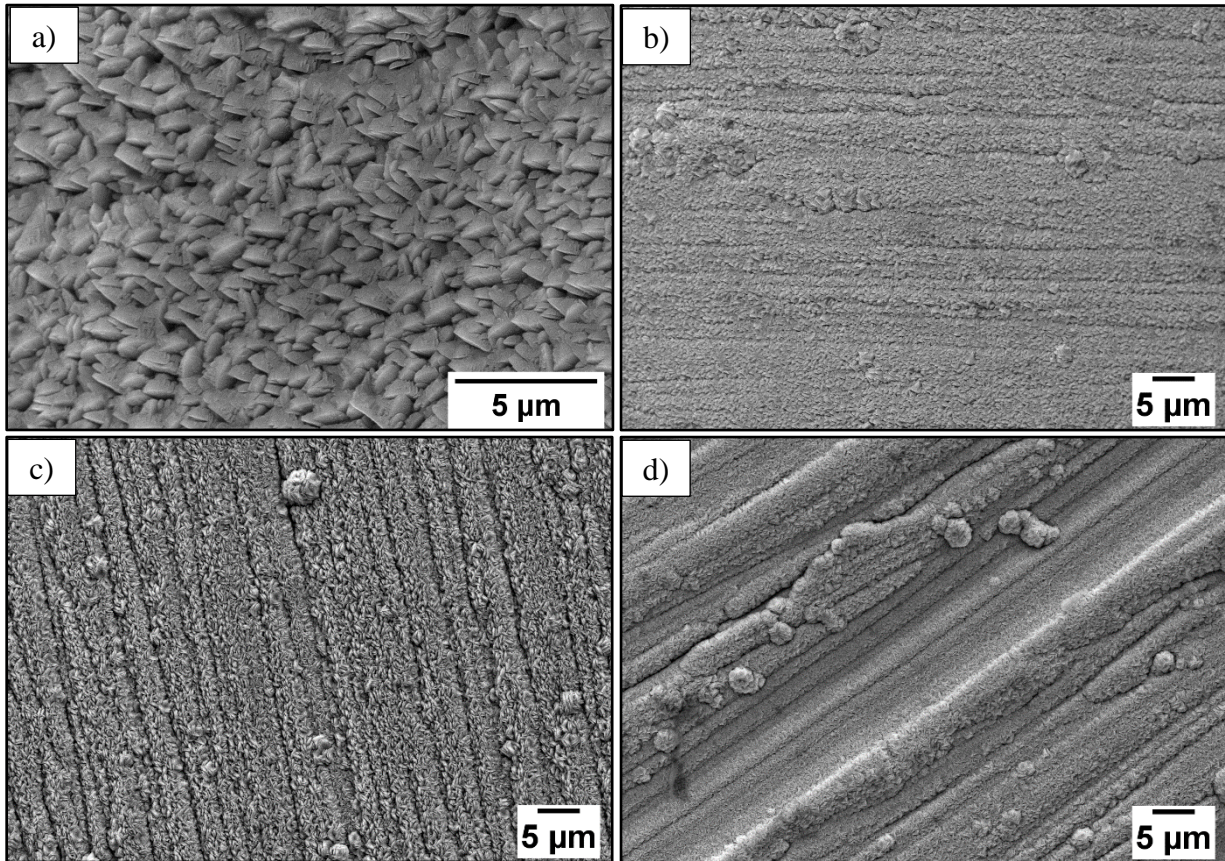
Figure 4.7 Surface micrograph of the Cr-coated Zircaloy-4: a) Zoom-in view of AR-Zr4-Cr, b) AR-Zr4-Cr, c) 600G-Zr4-Cr and d) 240G-Zr4-Cr [206].

Fig. 4.8 illustrates the surface topography of the AR-Zr4 and AR-Zr4-Cr under AFM (note that Fig. 4.8(a) and Fig. 4.8(b) do not correspond to the same region in the sample) along with their average line profile. At the nanoscale, the surface of the Cr-coated sample (Fig. 4.8(a)) gives a rougher appearance

when compared to the bare substrate (Fig. 4.8(b)); the asperities have a rounded morphology with size in the micron range and height in hundreds of nanometers. Although not presented here, the roughness factors r and surface parameter Ra for all three materials were recorded from AFM scans for all substrate and coated samples. The largest r and Ra were logged for the sample 240G-Zr4-Cr, while the other samples showed a slight increment after Cr-coating. The qualitative data from AFM scans were in good agreement with SEM surface micrographs and stylus profilometry results.
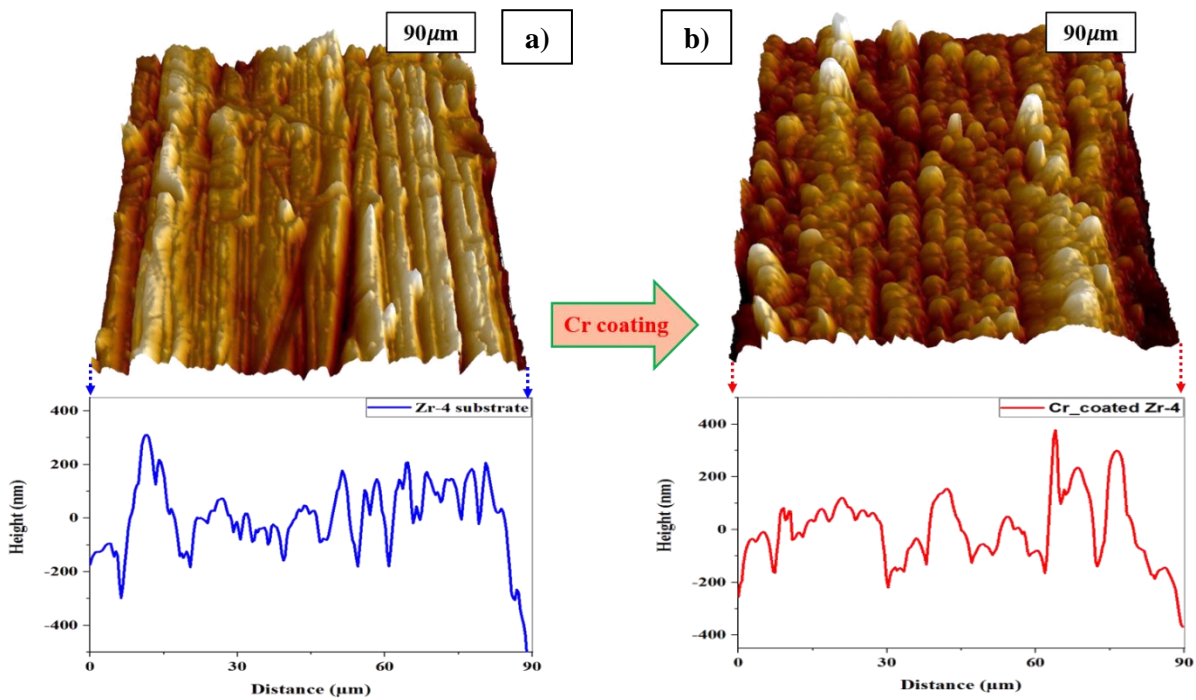
Figure 4.8 AFM surface morphologies and roughness distribution for: a) Zircaloy-4 substrate (AR-Zr4) and b) Cr-coated Zircaloy-4 (AR-Zr4-Cr) [206].

The average of ten contact angle measurements for substrate Zircaloy-4 and Cr-coated Zircaloy-4 samples are compared in Fig. 4.9(a). The substrate sample, AR-Zr4, evidenced the lowest contact angle among the evaluated substrate samples. According to a wide range of studies, surface roughness has proven to play an essential role in wetting and spreading phenomena [186][201-202][216-218]. For example, the contact angle of the Zircaloy surface decreased by 28% when roughness increased from 0.52

51

μm to 0.58 *μm* [129][219]. Cr particles deposited on micro-scratched surfaces changed surface wetting characteristics of the bare surface to more hydrophilic. In Fig. 4.9(a), it is observed that a water droplet partially wets the surface in the case of substrate samples, AR-Zr4, 600G-Zr4 and 240G-Zr4. On the contrary, a complete wetting is observed with a significant decrease in the contact angle for all of the Cr-coated surfaces. This implies that the sub-micron features on the surface possibly start to wick a droplet, causing additional movement of the triple contact line. Second, micro-scratches coupled with the sub-micron Cr features caused an additional wetting of water droplet, whose volume was fully distributed onto the surface. A noticeable higher contact angle was logged for 600G-Zr4-Cr and 240G-Zr4-Cr samples as compared to the AR-Zr4-Cr sample. This can be attributed to the different levels of roughness on the sample surfaces and directions of measurement. Typically, the wetting behavior of a water droplet on unidirectional scratches is shown differently along the different visualization directions [136][220].
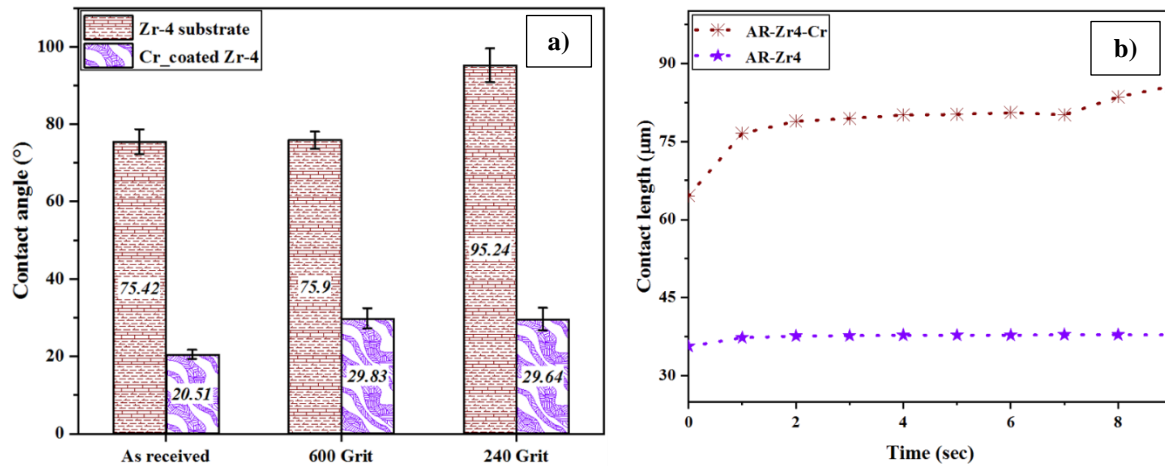
Figure 4.9 Wettability: a) Comparison of static contact angle for all samples and b) Comparison of droplet spreading for AR-Zr4 and AR-Zr4-Cr [206].

The dynamic wetting capability of hydrophilic surfaces could not be distinguished by measuring an equilibrium contact angle alone. This is because the liquid spreading phenomenon involves a rapid angle transition and liquid absorption onto the surface as soon as a droplet makes contact with the surface.

52

Especially below 30º, the surface is considered to be thoroughly wetted by the water droplet. Then, the triple contact line of the droplet on the surface disappears [186]. Thus, to characterize the dynamic wetting behavior of Cr-coated surfaces, dynamic droplet-imaging experiments were conducted by tracking the spreading history of a water droplet, as explained in Chapter 3. Fig. 4.9(b) shows how the drop base diameter advances over the surface on the second timescale for AR-Zr4 and AR-Zr4-Cr samples. A water droplet in Cr-coated samples spread at a rate of almost twice that in their bare substrate. Here, we aimed at the initial spreading behavior from 0-10 s, which was sufficient to determine wetting differences between bare surfaces and coated surfaces.

4.3.3 High-temperature wettability measurement

With the courtesy and support from the Red Lab at MIT, the wettability of the ATF materials was assessed at high temperature and pressure. MIT developed an apparatus (detailed description of facility is provided in MS thesis of Anupam Jena [221]) to measure static, advancing, and receding contact angle from sub-atmospheric conditions up to the critical point of water in a fully degassed, saturated steam-water environment. Fig. 4.10 shows the configuration of the autoclave facility. The actual test section for the contact angle measurement is accommodated inside the autoclave (Fig. 4.10(a)), equipped with two thermocouples for the temperature measurement of the sample and the autoclave environment. A cartridge heater is embedded underneath the sample holder to maintain the sample temperature and evaporate the residual water after each measurement. Fig. 4.10(b-c) shows the average of three contact angle measurements up to PWR temperature and pressure for both Zircaloy-4 and Cr-coated Zircaloy-4 samples. For both samples, the contact angle at high pressure and temperature becomes zero, which indicates that the surfaces become super-hydrophilic. However, the contact angle decreases faster on the coated sample (Fig. 4.10(b)) than on the substrate surface (Fig. 4.10(c)). The potential cause of this trend can be the different surface roughness and surface energy [186][221]. In this study, the average roughness, Ra for Zircaloy-4 was 0.39 μm, while for Cr-coated Zircaloy-4 it was 0.45 μm.

53
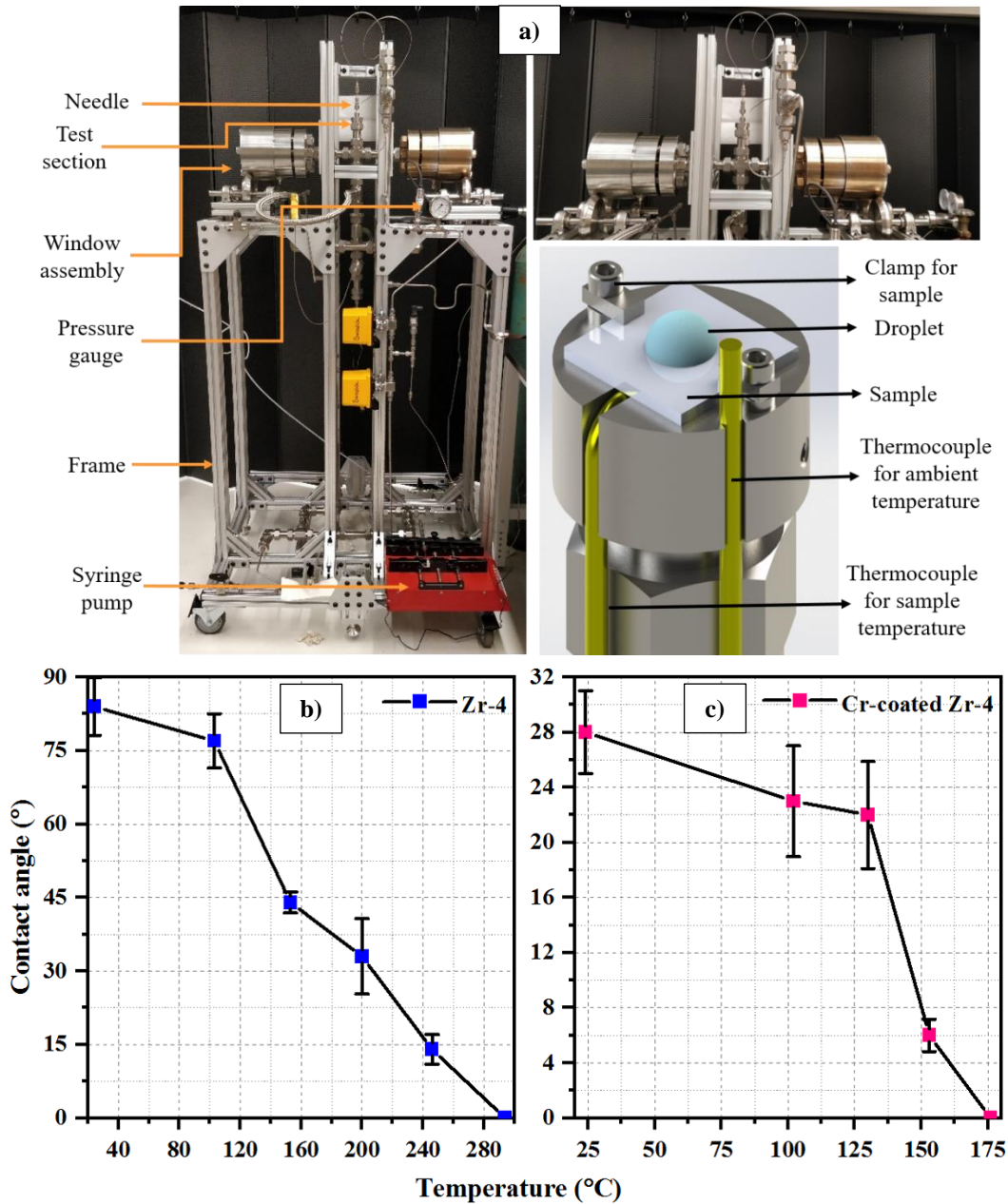
Figure 4.10 High-temperature wettability: a) Autoclave-facility with test section [221]; temperature dependence of contact angle of water on b) Zircaloy-4, and c) Cr-coated Zircaloy-4 samples.

4.4 Summary

Detailed surface characterization was conducted for ATF cladding candidates, such as APMT, C26M, Zircaloy-2, substrate Zircaloy-4 and Cr-coated Zircaloy-4 produced by PAPVD technique. The surface

properties of all samples were assessed in terms of chemical composition, roughness, topography, and wettability. The microindentation test showed that the coating has a high hardness (4.12 GPa) compared to that of the substrate, Zircaloy-4, which has a hardness value of approximately 2.24 GPa. The pull-off test indicated that the coating adhered well to the Zircaloy-4 substrate. Roughness measured from as-received samples were logged higher value for both FeCrAl alloys (APMT and C26M), which were almost double compared to the Zircaloy-2 specimen. Similarly, overall roughness for coated samples was higher compared to their substrates. The influence of the substrate's roughness on adhesion property is not substantial, though larger adhesion values were obtained for rougher substrates. The wettability of each surface was assessed by measuring its contact angle with water. According to the study for the as-received materials, Zircaloy-2 showed a lower contact angle compared to the FeCrAl alloys (APMT and C26M). A significant enhancement in wettability was logged after the deposition of chromium coating, which may improve the thermal-hydraulic performance of the cladding surface, tolerating higher heat fluxes before departure boiling is evidenced. Furthermore, the contact angle measurements at high temperature and pressure also confirmed the hydrophilic wetting characteristics of the coating.

55

Chapter 5: Surface modification and the evolution of ATF cladding surface under environment exposure

5.1 Introduction

The research on ATF claddings has highlighted and evidenced that the use of coatings could be a practical way to improve the existing nuclear fuel system [16][24][222]. However, the adoption of coatings for fuel claddings has faced challenges due to inadequate adhesion with the substrate that impacts the overall performance of the material [30][32][197]. The adhesion properties can be improved by ensuring thick and dense microstructures in the coating layer. For the evolution, Kim et. al. [210] coated a thick Cr-layer on the Zircaloy-4 surface using a 3D laser coating technique and confirmed that the layer was intact without any defects in microstructure during ring tensile tests. This result indicates that the micro-coated layer on Zr-based has excellent adhesion performance. However, it should be noted that regarding thermal and mechanical properties, the surface coating inevitably encounters a conflict between material integrity and thermal safety. For the material aspect, the microstructures of the coating layer need to be thick and dense, whereas, from the thermal safety viewpoint, very smooth surface finishing resulting from thick and dense structures may cause an unintended reduction in CHF. For example, Kam et. al. [119] compared the pool boiling CHF between the SiC layer deposited using PVD sputtering, Cr layer deposited using electroplating process and Zircaloy-4. Their results report that the CHF of the Cr layer decreased by 70% of the bare Zircaloy-4, while the CHF of a 1 um thick SiC layer increased by 150%. The reduction of the CHF in the Cr layer could be due to a low roughness value. This indicates that a very smooth surface has the potential to reduce the CHF. Yeom et. al. prepared as-deposited and as-polished (sample polished after coating with 600 grit) Cr-coated Zirlo® samples and reported 67% higher CHF for polished sample due to higher surface roughness level [223]. Furthermore, FeCrAl and Cr-coating were deposited on polished stainless steel substrate using 60 and 800 grit sandpaper were tested in a pool boiling facility to understand the effect of surface characteristics on CHF measurements. For both coating materials, enhancement in CHF and HTC values for rough surfaces were

obtained and explained by the liquid spreading phenomenon [121]. As mentioned in Chapter1, Son et. al. [117] prepared FeCrAl coated samples with different surface roughness and achieved significant CHF enhancement in pool boiling. Thus, surface-modified Zircaloy-4 was produced by depositing a protective coating of chromium by two different coating techniques, PVD and Cold Spray. Similarly, both FeCrAl alloys were polished using different grit SiC papers to study the effect of surface roughness on their wettability and spreading ability. Mechanical properties such as hardness, adhesion strength, and ring compression strength for both types of Cr-coatings were tested and compared. The surface wettability of all samples was assessed in terms of contact angle using a contact angle goniometer. In most cases, the surface wettability is increasing as a result of the surface pretreatment using atmospheric pressure air plasma [206][224-226]. However, the aging effect decreases the wettability after several hours or days [227]. It may play an important role when there is a time delay between fabrication and installation. Hence, in this part of the dissertation, the influence of the plasma treatments and environmental aging on the wettability at atmospheric conditions of the coated Zircaloy, FeCrAl alloys, and standard Zircaloy samples was studied by investigating the evolution of the surface chemistry. In this section, the formation of Cr oxides and hydroxides and carbonaceous species that affect materials wettability is evidenced. However, there were negligible changes in wetting characteristics recorded for substrate Zircaloy-4 and FeCrAl alloys, APMT and C26M. This is a crucial fact to consider when incorporating surface parameters in the performance of ATF cladding materials.

5.2 Material and methods

After evaluating the effect of the surface roughness of small size substrate specimens on their coating, large-size specimens of Zircaloy-4 substrate were produced with different surface roughness. Before PVD of the Cr coating, the surfaces of the substrates were modified with three different roughness levels to investigate their effect on the Cr-coating characteristics: a) as-received, b) ground with 600-grit SiC grinding paper, and c) ground with 240-grit SiC grinding paper. Similarly, APMT and C26M sample surfaces were also modified with three different roughness levels: a) ground with 1200-grit SiC grinding

57

paper, b) as-received, and c) ground with 120-grit SiC grinding paper. The details of the grinding process were explained in Chapter 3. The samples coated using the cold-spray technique were ground before coating with 320-grit SiC grinding paper, with continuous ethanol spraying. After deposition of the coating, the samples were polished with 600-grit SiC grinding paper to get a uniform coating thickness throughout, followed by a cleaning stage. A detailed description of sample preparation for both coating processes with their sample IDs is provided in Table 5.1.

Table 5.1 Test sample IDs with their conditions.

Sample ID	Conditions
AR-Zr4	As received Zr-4 sample from vendor
600G-Zr4	Zr-4 sample ground using 600 grit SiC abrasive paper
240G-Zr4	Zr-4 sample ground using 240 grit SiC abrasive paper
320G-Zr4	Zr-4 sample ground using 320 grit SiC abrasive paper
AR-Zr4-Cr-PVD	Cr-coating deposited on "AR-Zr4" using PVD technique
600G-Zr4-Cr-PVD	Cr-coating deposited on "600G-Zr4" using PVD technique
240G-Zr4-Cr-PVD	Cr-coating deposited on "240G-Zr4" using PVD technique
AR-Zr4-Cr-CS	Cr-coating deposited on "320G-Zr4" using cold spray technique
AR-APMT	As received APMT sample from vendor
1200G-APMT	APMT sample ground using 1200 grit SiC abrasive paper
120G-APMT	APMT sample ground using 120 grit SiC abrasive paper
AR-C26M	As received C26M sample from vendor
1200G-C26M	C26M sample ground using 1200 grit SiC abrasive paper
120G-C26M	C26M sample ground using 120 grit SiC abrasive paper

The Cr coatings were deposited on the Zircaloy-4 tubes using two different techniques, PVD and Cold Spray. The coating processing conditions used for both PVD and CS techniques are listed in Table

58

5.2. To check coating strength, hardness measurements were performed with a nano-hardness tester NHT (Anton Paar with indentation software version 3.81.05) following the ASTM standard practices [194-195]. In this study, 0.51 and 1.02gf of applied load (5 mN and 10 mN of applied force respectively) were used with an indentation dwell time of 10 s. Ten measurements were taken for AR-Zr4, AR-Zr4-Cr-PVD, and AR-Zr4-Cr-CS. An NST scratch tester (Anton Parr) was used to carry out the scratch adhesion tests. The progressive loading rate was 250 mN/min and the speed was 0.5 mm/min. The nominal maximum load was 200 mN. The Rockwell diamond indenter (radius of 2 μm) was cleared of residues by performing indentation in acrylic before and after testing of the actual specimens. Five scratch tests of 0.24-0.39 mm per sample were performed for statistical analysis. After the tests, the samples were evaluated using optical microscopy.

Table 5.2 Coating process parameters.

PVD		Cold Spray	
Sputtering parameters	**Target condition**	**Parameter**	**Value**
Target material	99.999% pure chromium	Powder	AEE CR-103 (particle size < 45 µm)
Substrate material	Zircaloy-4	Spray System	Impact Innovation 5/11
Substrate temperature	Room temperature	Gun Temperature	900 ºC
Working pressure (Torr)	2.5×10^{-3}	Gun Pressure	45 Bars
DC power (W)	8.0 kW	Process Gas	Nitrogen
Sputtering gas	Argon (Ar)	Nitrogen Flow Rate	85 m^3/Hr
Target size	3.5"×36"	Powder Feed Rate	2.5 RPM
Substrate bias voltage during deposition	-95 V	Carrier Gas Flow Rate	3.0 m^3/Hr

		Lathe & Robot Speed	577 RPM
Plasma clean prior to deposition	-800 V, 30 mTorr, 15 Minutes		
		Step Size	0.04 mm
		Number of Passes	7

Furthermore, the aging studies and the evolution of the contact angle with time after exposure to water and air were evaluated. In this case, both AR-Zr4-Cr and 600G-Zr4-Cr specimens were initially exposed to Ar plasma using Solarus 950 Plasma Treatment System for 4 minutes at a power of 50 W. Afterward, the samples were submerged in distilled water for 48 hours. Once removed from the water, the static contact angle was measured, and then the samples were kept in a glass container open to air. The contact angle was tracked regularly for 50 days.

5.3 Result and discussion

5.3.1 Characterization of ATF materials after surface modification

Fig. 5.1 shows the diffraction pattern of the bare substrate, AR-Zr4, and both types of coatings, AR-Zr4-Cr-PVD and AR-Zr4-Cr-CS. As seen in Chapter 4, all of the diffraction peaks from the substrate Zircaloy-4 corresponded to the α-Zr phase with a HCP crystal structure [143][207]. All four additional peaks identified from Cr-coated Zircaloy-4 corresponded to pure chromium with a BCC structure [44][60][205]. The decrease in intensity or otherwise absence of the peaks associated with Zircaloy-4 in the Cr-coated samples is caused by the attenuation of the diffracted X-rays as they pass through the coating. An interesting feature in the XRD patterns for both types of coatings (AR-Zr4-Cr-PVD and AR-Zr4-Cr-CS) is a disproportionate diffracted intensity of chromium peaks from a given (*hkl*) plane. This could be due to film texture, which is influenced by deposition methods and thickness of deposited coatings [214][228-229].
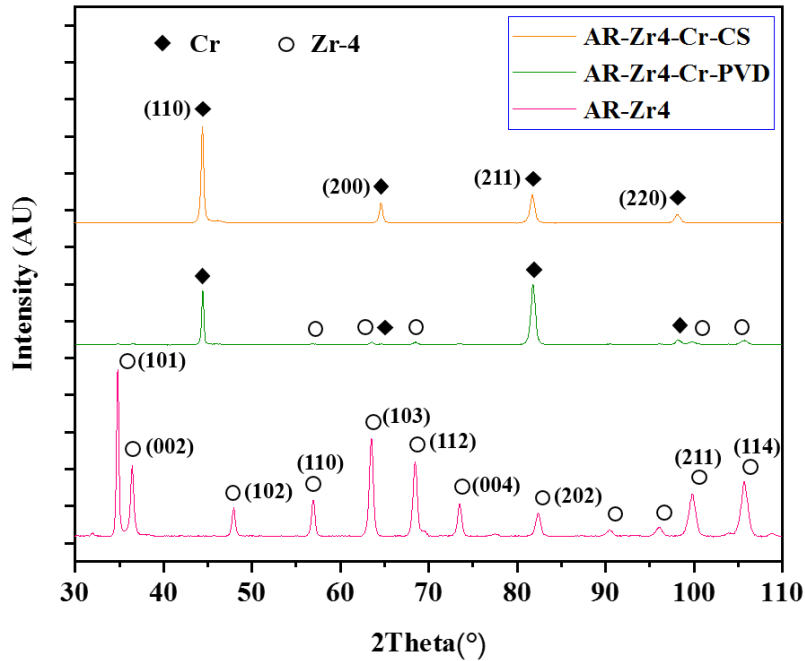
Figure 5.1 X-ray diffraction pattern of the substrate Zircaloy-4 and both types of Cr-coated Zircaloy-4 [152].

The SEM micrographs in Fig. 5.2(a-b) are the cross-sections of the Cr-coated Zircaloy-4 cladding samples, AR-Zr4-Cr-CS and AR-Zr4-Cr-PVD. The measured coating thickness from a micrograph of the Cold Spray Cr-coated Zircaloy-4 sample, AR-Zr4-Cr-CS (Fig. 5.2(a)) was 29.0±2.0 μm. The coating layer and substrate interface shows a strong bonding and mechanical interlocking without significant indications of degradation. Fig. 5.2(b) shows a micrograph of the coated sample, AR-Zr4-Cr-PVD. The thickness of a Cr layer was 6.48±1.41 μm. The coating had a dense microstructure with uniform columnar morphology and a well-defined interface. The measured average coating thickness for the other two samples, 600G-Zr4-Cr-PVD and 240G-Zr4-Cr-PVD, was within ±1.5 SD around the mean value.
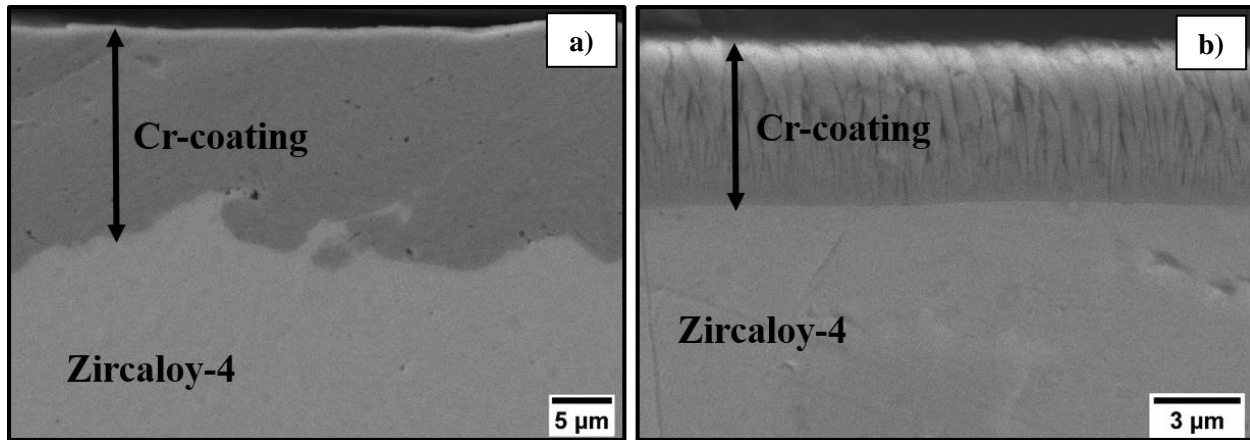
Figure 5.2 Cross-sectional SEM view (Hitachi SU-70): a) AR-Zr4-Cr-CS, and b) AR-Zr4-Cr-PVD

[152].

The engineering stress and strain curves from the ring compression test for the substrate AR-Zr4 and both types of coated samples, AR-Zr4-Cr-PVD and AR-Zr4-Cr-CS, with the samples' appearances before and after the tests are shown in Fig. 5.3(a). The stress-strain curves followed a similar trend for all the materials and evidenced that the strength of the Cr-coated samples was higher than that of the substrate bare sample. The results from this test data are summarized in Table 5.3. The yield strength was higher by almost 8% for AR-Zr4-Cr-PVD, and it was ∼15% higher for AR-Zr4-Cr-CS than that for the substrate, AR-Zr4. Herein, the compressive strength and stiffness of Zircaloy-4 cladding were increased after the deposition of Cr-coating, with both methods PVD and CS, mainly owed to the high modulus of elasticity of Cr with a small contribution by the increased total thickness of cladding tube [230]. Higher compressive strengths after coating were reported in the literature [35][77][231-232]. The nanoindentation test data measured with 5 mN load are shown in Fig. 5.3(b). The deposition of the Cr-coating by both methods showed an increase in the hardness compared to that of the substrate, with CS having the highest values. According to Koehler et. al. [233] a strong solution can be produced with coating materials having widely differing shear moduli (μ) compared to substrate. Because the shear stress required to move dislocations across layer/substrate interface is directly proportional to the product of modulus difference and $\cos\theta$, where θ is the smallest angle between glide planes and the interface. For

62

instance, in this case, the shear modulus of chromium is almost double compared to substrate Zircaloy materials. Hence, coated materials demonstrated higher hardness compared to substrate. Also, for metal and alloy films, the hardness correlates well with the Hall-Petch relation [234] given as following:

$$H = H_i + K_H l_g^{-\frac{1}{2}}$$ (5.1)

Where H is the hardness, H_i is the intrinsic hardness of a single crystal, l_g is the grain size, and K_H is a material constant. Furthermore, hardness measurements may be strongly influenced by the penetration depth of the indenter relative to the coating(s) thickness [195][209]. For this, the indentation depth for all samples was recorded to exclude in the analysis any possible interactions of the indenter with the substrate, particularly for the sample AR-Zr4-Cr-PVD with the lowest coating thickness (~5-6 μm). The maximum indentation depth was not higher than 0.26 µm among all tested samples. The hardness results obtained here are comparable with those reported in the literature [35][40][207-208][211-212].
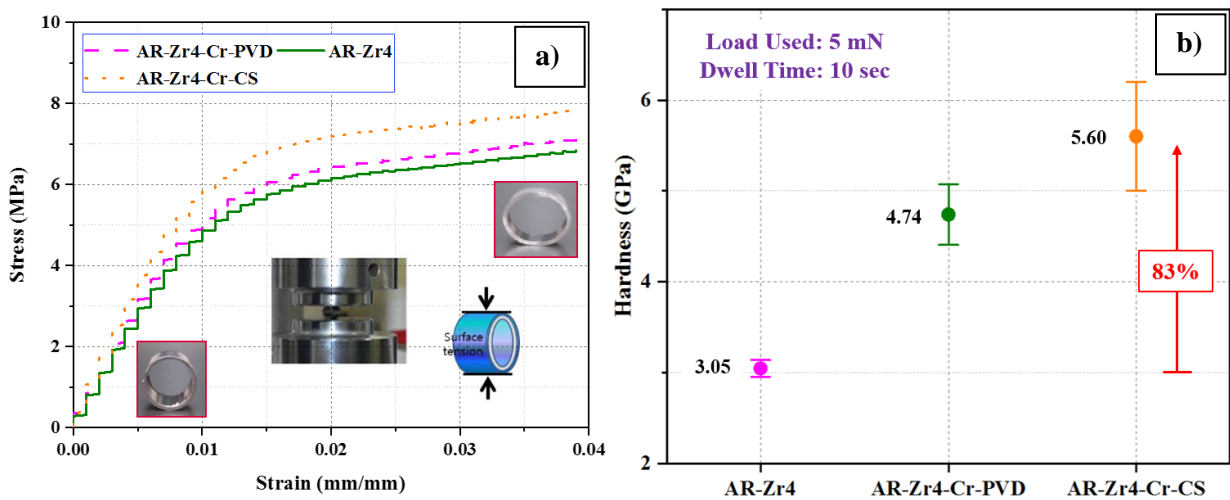
Figure 5.3 Comparison of mechanical properties of substrate Zircaloy-4 (AR-Zr4) and both types of Cr-coatings (AR-Zr4-Cr-PVD and AR-Zr4-Cr-CS): a) Ring compression tests and b) nanoindentation tests [152].

Table 5.3 Ring compression test results.

Sample	Parameter		
	Peak load (N)	Yield strength (Mpa)	Modulus E (Mpa)
AR-Zr4	341.10	5.34	570.23
AR-Zr4-Cr-PVD	371.36	5.79	590.10
AR-Zr4-Cr-CS	398.36	6.13	741.13

The results presented in Fig. 5.4 show that the average roughness, Ra values varied from 0.434 μm for the substrate AR-Zr4 up to 1.222 μm for the sample AR-Zr4-Cr-CS. Among all the tested samples, the Cr-coated samples evidenced a higher roughness compared to their substrate. Based on the definition of Ra, our results indicate deeper valleys and higher peaks in the surface profile with the decreasing of the grit size during the polishing of the substrate.
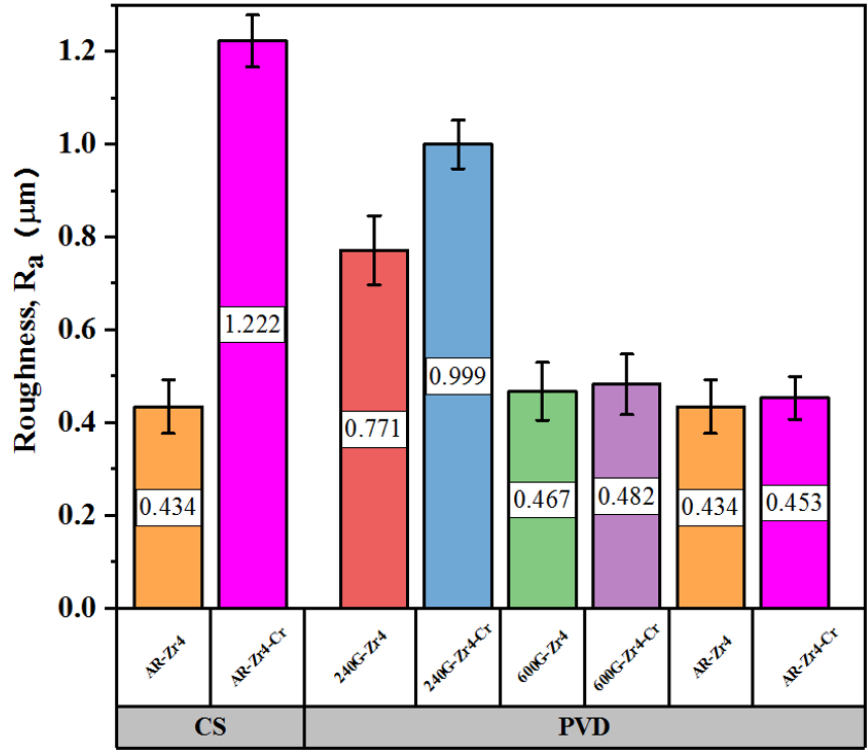
Figure 5.4 Surface roughness measured using contact profilometer for all samples [152].

Fig. 5.5(a-c) shows surface topography images taken with AFM for substrate AR-Zr4 and both types of Cr-coated samples, 600G-Zr4-Cr-PVD and AR-Zr4-Cr-CS. At the nanoscale, the surface of both kinds of Cr-coated samples appears rougher compared to the bare substrate. Compared to contact profilometry, the AFM method operates on a different length scale. It is interesting to note that the Ra values give similar trends, although quantitatively, they are not similar to the values provided by profilometry. The roughness measurements confirmed that Ra was 0.43 μm for AR-Zr4 while it was 0.47 μm for 600G-Zr4-Cr-PVD and 1.04 μm for AR-Zr4-Cr-CS. The roughness values at the nanoscale obtained by AFM, having the highest resolution, were generally lower than those obtained using a profilometer.

65
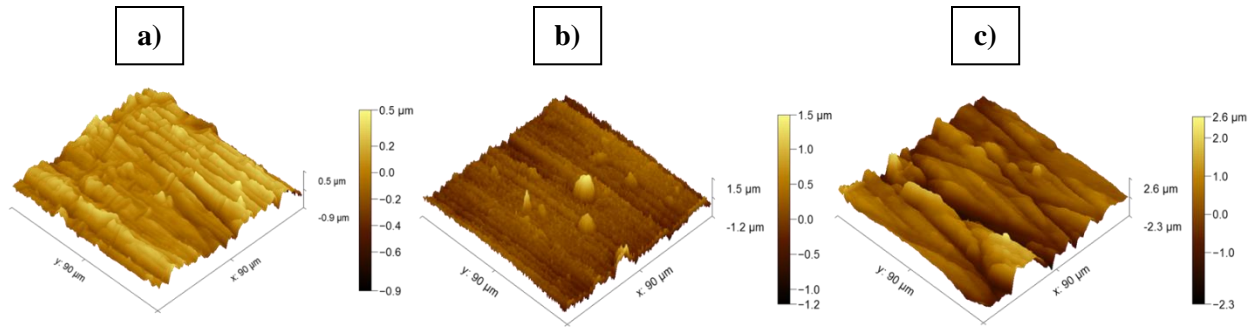
Figure 5.5 AFM surface topography for as received: a) AR-Zr4, b) 600G-Zr4-Cr-PVD and c) AR-Zr4-Cr-CS [152].

The nano scratch test was carried out to evaluate the adhesion between the coating and substrate for the three substrate conditions, as-received, 600 Grit, and 240 Grit for PVD coating and Cold Spray coatings. The point where the coating fails is called delamination, and the load measured at that point is the critical force (Lc) [235]. The adhesion strength of the Cr coating on the substrate is evidenced to be influenced by the substrate roughness. From the results in Table 5.4, the critical force shows an increase with increasing surface roughness. The science of coating technologies has described how a decrease in surface roughness reduces the mechanical interlocking at the interface between the coating and metal substrate. In other words, an increase in roughness increases the specific surface area, and it can be effective in improving the adhesion strength [213]. However, the difference between the critical force for samples 600G-Zr4-Cr-PVD and 240G-Zr4-Cr-PVD was not remarkable. These results align with those obtained for Cr-coated samples using PAPVD techniques described in Chapter 4.

Table 5.4 Adhesion property of all tested samples.

Sample	Critical force Lc (mN)
AR-Zr4-Cr-PVD	117.69 ± 7.44
600G-Zr4-Cr-PVD	158.59 ± 7.46
240G-Zr4-Cr-PVD	169.54 ± 12.02
AR-Zr4-Cr-CS	>200

Fig. 5.6(a) shows an optical micrograph taken from the point of the wear track where the coating failed with a scratch testing curve for PVD (240G-Zr4-Cr-PVD) coated samples. In the graph, Ft (tangential force), the force that opposes the relative motion between the stylus and the surface; COF (scratch coefficient of friction), the ratio of the tangential force to the normal force (Fn) applied to the stylus at a specific point in the scratch; Pd (penetration depth), depth of the indenter into the sample; Rd (residual depth), depth at which permanent plastic deformation occurs. The micrographs revealed delamination for all PVD-coated samples, while no delamination was observed for CS-coated Zircaloy-4 (for sample AR-Zr4-Cr-CS shown in Fig. 5.6(b)). In Fig. 5.6(a) the scratch on the coating became wider and deeper as the load by the indenter gradually increased until reaching the Lc, at ~312 μm from the start of the scratch, at which the substrate is exposed. Furthermore, the penetration depth of the indenter at the point of coating failure was in agreement with the average thickness of the coating. The region circled in Fig. 5.6(a) indicated that the Cr-coating had peeled off from the Zircaloy-4 substrate, consistent with its lower critical load to failure (Table 5.4) as compared to that for the CS coating.
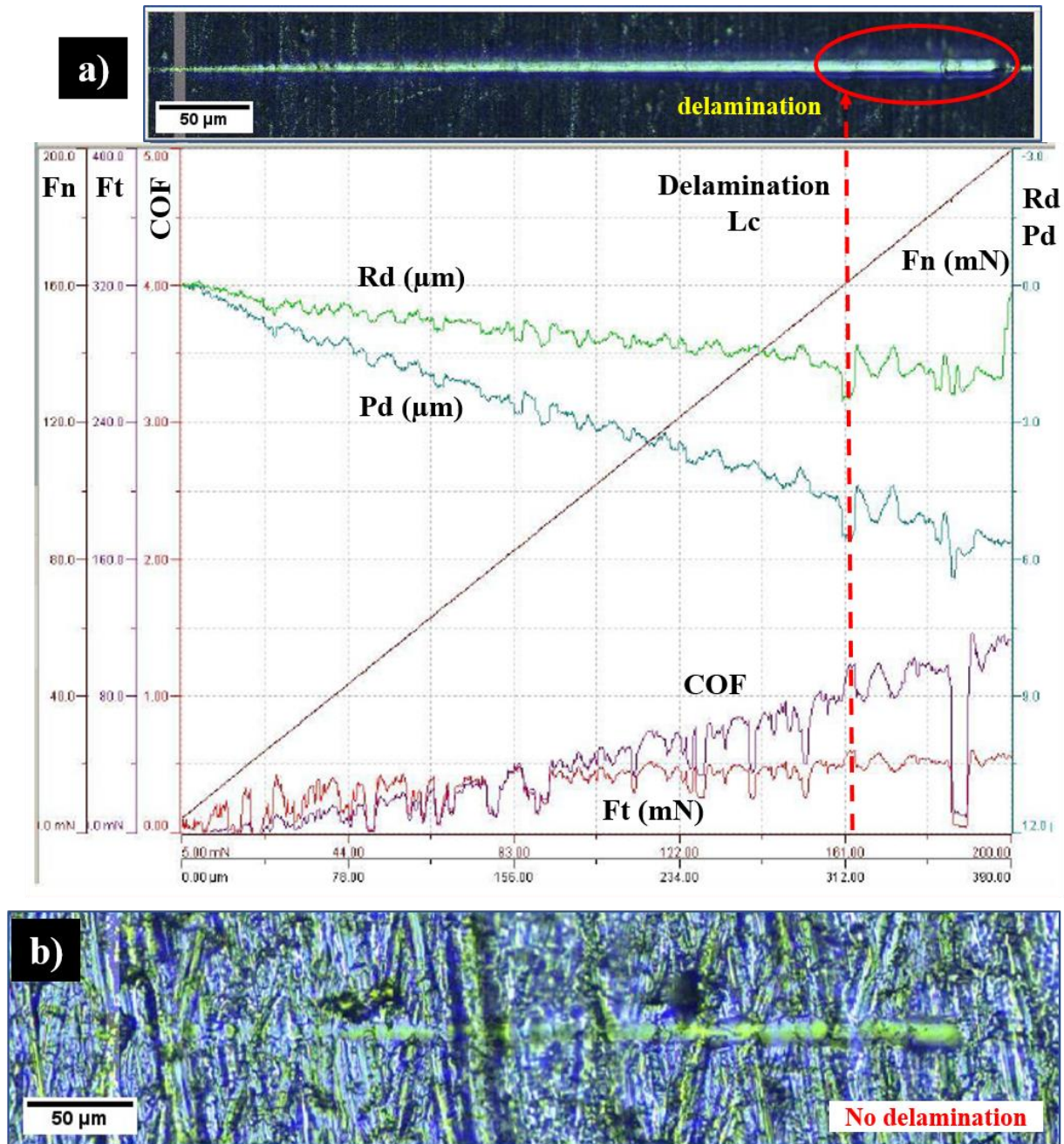
Figure 5.6 Failure of coating for samples: a) 240G-Zr4-Cr-PVD and b) AR-Zr4-Cr-CS [152].

Fig. 5.7(a) provides a comparison of an average of fifty contact angle measurements for substrate Zircaloy-4 samples and both types of Cr-coated Zircaloy-4 samples. The substrate AR-Zr4 demonstrated the lowest contact angle among the tested substrate samples before the deposition of Cr-coating. The broad field of surface science has indicated that surface roughness plays an essential role in wetting and

the spreading phenomena [186][201-203][216-219], as we have also seen in previous results for other samples in section 4.3.1. The deposition of Cr-coating using both coating techniques changed the surface wetting characteristics of the bare surface from moderately hydrophilic to completely hydrophilic. In Fig. 5.7(a), for all substrate samples, the droplet partially wets the surface within the time of contact angle measurement, while complete wetting is observed with a significant decrease in the contact angle for the Cr-coated surfaces. The wetting characteristics after Cr-coating indicate that the sub-micron features on the surface possibly start to wick a droplet, causing additional movement of the triple contact line. In addition to that, micro-scratches of the substrate surface coupled with the sub-micron Cr features caused an additional wetting of water droplet, whose volume was fully distributed onto the surface. If we compare the wettability results of all coated samples with their corresponding roughness data, a trend of increase in contact angle was logged with the increase in surface roughness. This can be attributed to the different levels of roughness on the sample surfaces and directions of measurement [136][220]. To characterize the dynamic wetting behavior of Cr-coated surfaces, dynamic droplet-imaging experiments were conducted by tracking the spreading history of a water droplet. Fig. 5.7(b) shows how the drop base diameter or contact length advances over the surface on the second timescale for substrate AR-Zr4 and both types of Cr-coated samples, AR-Zr4-Cr-PVD and AR-Zr4-Cr-CS. A water droplet on sample AR-Zr4-Cr-PVD spread at a rate of almost twice that on their bare substrate AR-Zr4. While AR-Zr4-Cr-CS showed weak spreading compared to AR-Zr4-Cr-PVD, it was still high compared to the substrate sample AR-Zr4. The lower spreading rate for AR-Zr4-Cr-CS compared to AR-Zr4-Cr-PVD can be understood by its higher surface roughness and higher contact angle values.
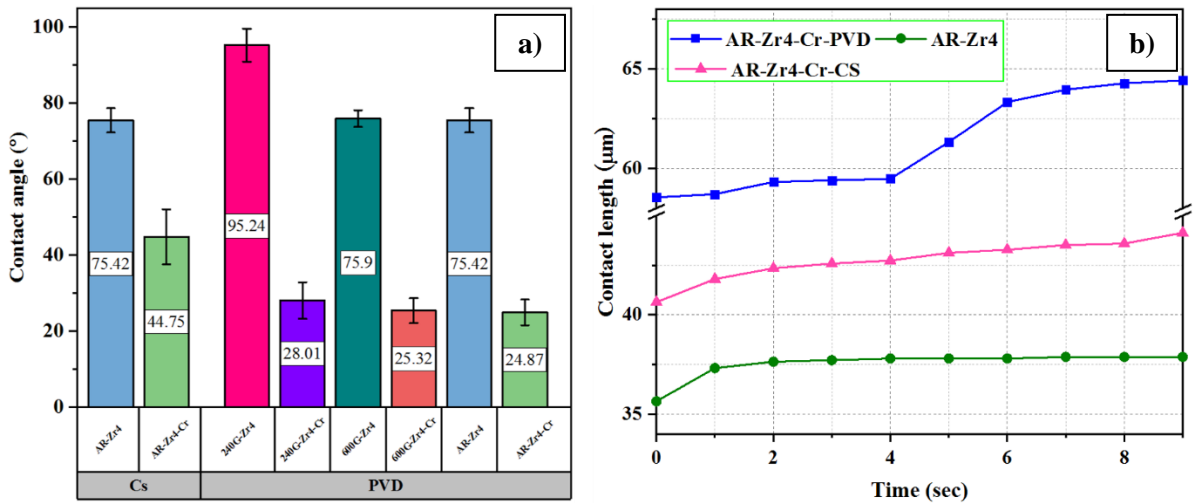
Figure 5.7 Wettability: a) Comparison of static contact angle for all samples, and b) Comparison of droplet spreading for substrate Zircaloy-4 (AR-Zr4) and both types of Cr-coated Zircaloy-4 (AR-Zr4-Cr-PVD and AR-Zr4-Cr-CS) [152].

Surface characteristics, roughness, and wettability, of APMT and C26M after surface modifications were investigated and reported in Table 5.5. Roughness for all three types of modified surfaces is quite similar for both APMT and C26M. Wetting characteristics were assessed by measuring contact angle for all samples and provided in Table 5.5. For as-received samples, their contact angle is almost the same. However, after polishing, the contact angle of the alloys varied to some degree. Between the specimens grounded using 1200 grit SiC paper, C26M showed higher wettability while surface evidenced poor wettability while grounded using 120 grit SiC paper. To understand the effect of surface roughness on wettability, liquid spreading tests were conducted for all samples and results are shown in Fig. 5.8. From the graph, for both FeCrAl alloys, as-received and samples polished with 120 grit SiC paper showed similar trend in droplet spreading. However, 1200 grit polished samples, C26M demonstrated higher droplet spreading (Fig. 5.8 (a)) compared to contact droplet length with time for 1200G-APMT sample (Fig. 5.8 (b)). On the other side, the higher wettability of 120G-APMT can be attributed to large and deep scratches in the surface, visualized from AFM images (Fig. 5.8) compared to the smooth topography of 120G-C26M sample. Here, each big scratch can work as a microchannel which helps to rewet the sample

70

surface during CHF event. A similar concept of capillarity flow through microchannel was used to explain significant CHF enhancement during pool boiling experiment [121].

Table 5.5 Surface roughness and contact angle data for FeCrAl alloys with different surface finish.

Sample	Roughness (µm)	Contact angle (°)
1200G-APMT	0.54 ± 0.07	98.98 ± 3.96
AR-APMT	0.68 ± 0.08	91.97 ± 2.78
120G-APMT	0.89 ± 0.05	84.58 ± 5.65
1200G-C26M	0.57 ± 0.03	83.39 ± 5.07
AR-C26M	0.69 ± 0.07	90.43 ± 2.28
120G-C26M	0.96 ± 0.03	95.94 ± 4.25
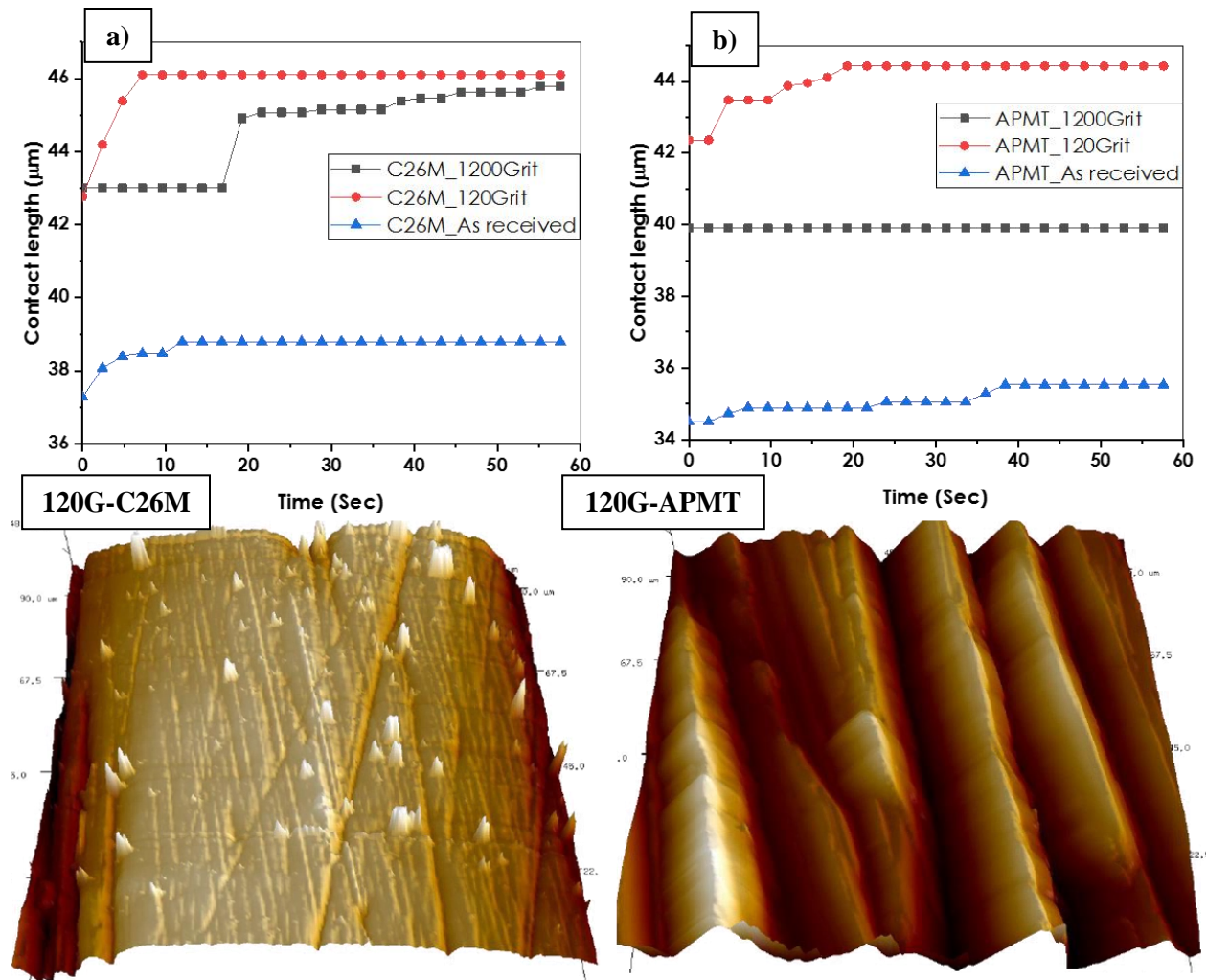
Figure 5.8 Spreadability and surface topography for C26M (a) and APMT (b) samples with polished surfaces.

5.3.2 Ambient aging effect and XPS investigations

The effect of environmental exposure on the specimens' wettability was investigated by tracking the changes in the water contact angle with time. For this, both types of coated samples (240-Zr4-Cr-PVD and AR-Zr4-Cr-CS) with almost similar surface roughness were selected. Before this experiment, the samples were initially cleaned in a plasma cleaner with Ar for 4 minutes. Surface energy has evidenced to be enhanced by plasma cleaning, significantly improving surface wettability [206][224-226]. This is caused by the removal of carbonaceous species from the surface upon their interaction with particles in

the plasma [236]. Similarly, in the current aging study, the samples' surface became superhydrophilic after plasma cleaning, as evidenced by their contact angle. Accurate measurements of the contact angle with 5 μL DI water droplets became difficult for the cylindrical tubes. As such, 1 μL DI water droplet was specifically used for the aging effect studies, minimizing the influence of gravitational forces [237-238]. Every time the measurement was completed for any given day, the samples were stored in a glass vial with a loose cap to allow for continuous air exposure while minimizing contaminations.

The comparison of the contact angle measurements with time for both samples is shown in Fig. 5.9. For both graphs (Fig. 5.9(a-b)), the annotation of the X-axis should be interpreted as follows: "Post-treat" means that samples were treated in plasma with Ar for 4 minutes, "2D Air" means the samples were kept in air for two days and likewise. These experiments using Cr-coated samples, 240G-Zr4-Cr-PVD and AR-Zr4-Cr-CS, revealed that air exposure has a considerable influence on the wettability measurements. At the beginning of the test, contact angle values (Pre-treat.) were large compared to those presented in Fig. 5.9(a) since the measurements were taken a few days after the coating process. The surface post-treatment with plasma clearly shows a significant change in surface wettability. These results are in agreement with a large body of published work in the field, where the plasma treatment is used for metal surface cleaning and activation [206][213][224][227][239-240]. The evolution of the contact angle for both 240G-Zr4-Cr-PVD and AR-Zr4-Cr-CS showed a trend that is a continuous increase of the contact angle with the exposure time (aging) in air. Although at the beginning of the aging studies, the contact angle difference between 240G-Zr4-Cr-PVD and AR-Zr4-Cr-CS was insignificant, the 240G-Zr4-Cr-PVD sample showed a slightly higher wettability at any given time after post-treatment. This phenomenon may be due to the rougher surface of AR-Zr4-Cr-CS compared to 240G-Zr4-Cr-PVD, as higher roughness increases the surface resistance to wetting for moderately hydrophilic and hydrophobic materials [186]. Nonetheless, in both cases, contact angles reached a maximum value ~ 95º and became stable for both types of samples after fifty days of ambient aging. Similarly, the aging study was conducted for both FeCrAl alloys, APMT and C26M, and Zircaloy-4 and Zircaloy-2. The stability of FeCrAl and Zircaloy surfaces is evidenced by

73

their contact angle measurements with time in Fig. 5.10. It is clear that the wettability of these samples was not significantly changed even after hundred days of aging.
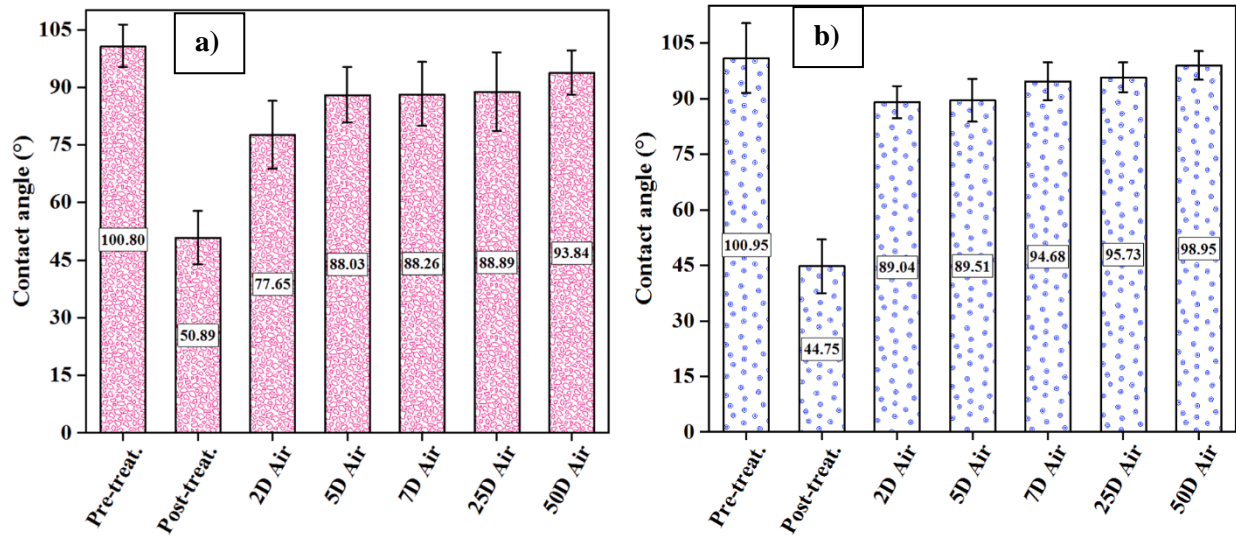
Figure 5.9 Aging effect and hydrophobic recovery of surface wettability for plasma-treated Cr-coated samples: a) 240G-Zr4-Cr-PVD and b) AR-Zr4-Cr-CS [152].
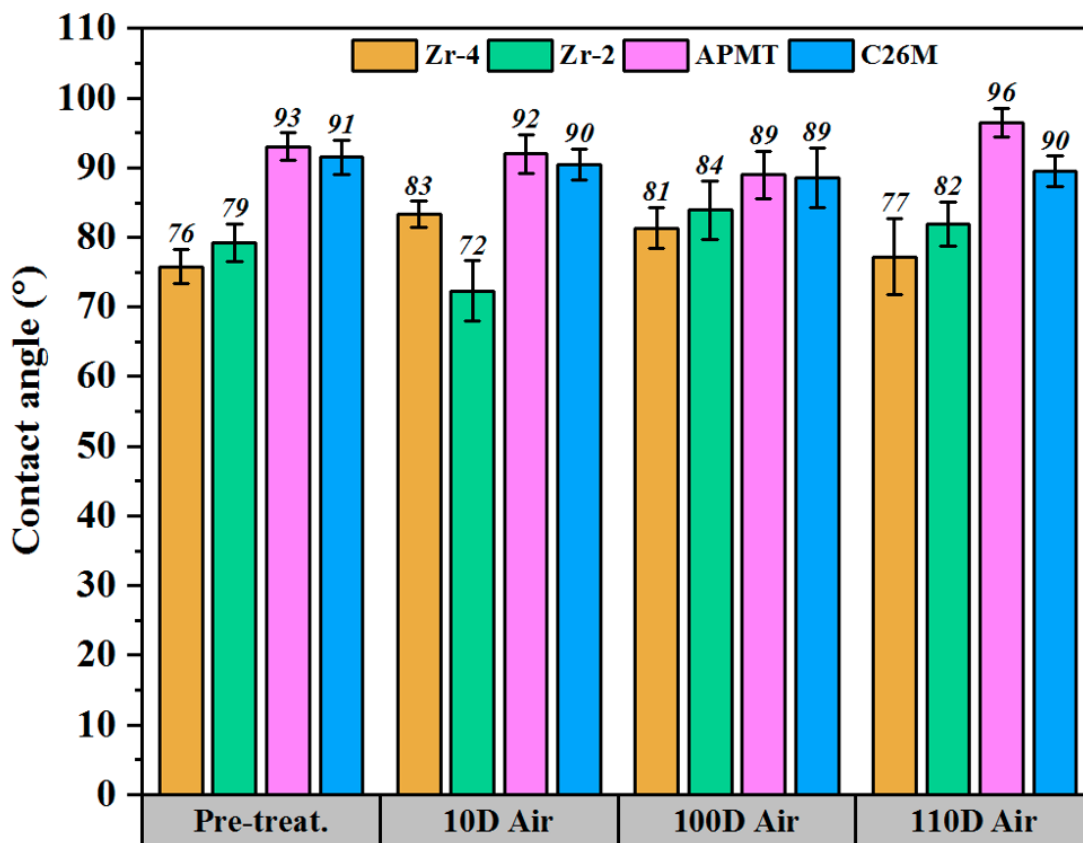
Figure 5.10 Aging effect of surface wettability for non-treated Zircaly-4, Zircaloy-2, APMT and C26M sample.

The aging effect on surface wettability under exposure to air at a normal laboratory environment was investigated by studying the material surface chemistry with XPS. The Cr $2p_{3/2}$ high-resolution XPS peaks of both types of Cr-coated samples, 240G-Zr4-Cr-PVD and AR-Zr4-Cr-CS samples exposed to the air, were deconvoluted to elucidate the contribution to the intensity from species at different valence states and binding energies (Fig. 5.11(a-c)). The XPS from the sample Zr4-Cr-Ref did confirm the presence of metallic Cr(0) with negligible contribution from higher oxidation states. The deconvolution of the XPS spectrum of Cr2p for both exposed samples revealed the presence of metallic Cr(0) and (III) valent chromium species in the surface layer, namely Cr(0) and (III) valent Cr(III) hydroxide (Cr(OH)$_3$) and oxide (Cr$_2$O$_3$) [241-242]. The peak positions associated with each Cr oxidation state are presented in Table 5.6 with their respective percentage area, which is within the range of binging energies reported in

the literature [240][243-249]. The fitting of the Cr(III) oxide in the XPS patterns in this work was treated with a multi-peak [250-252].
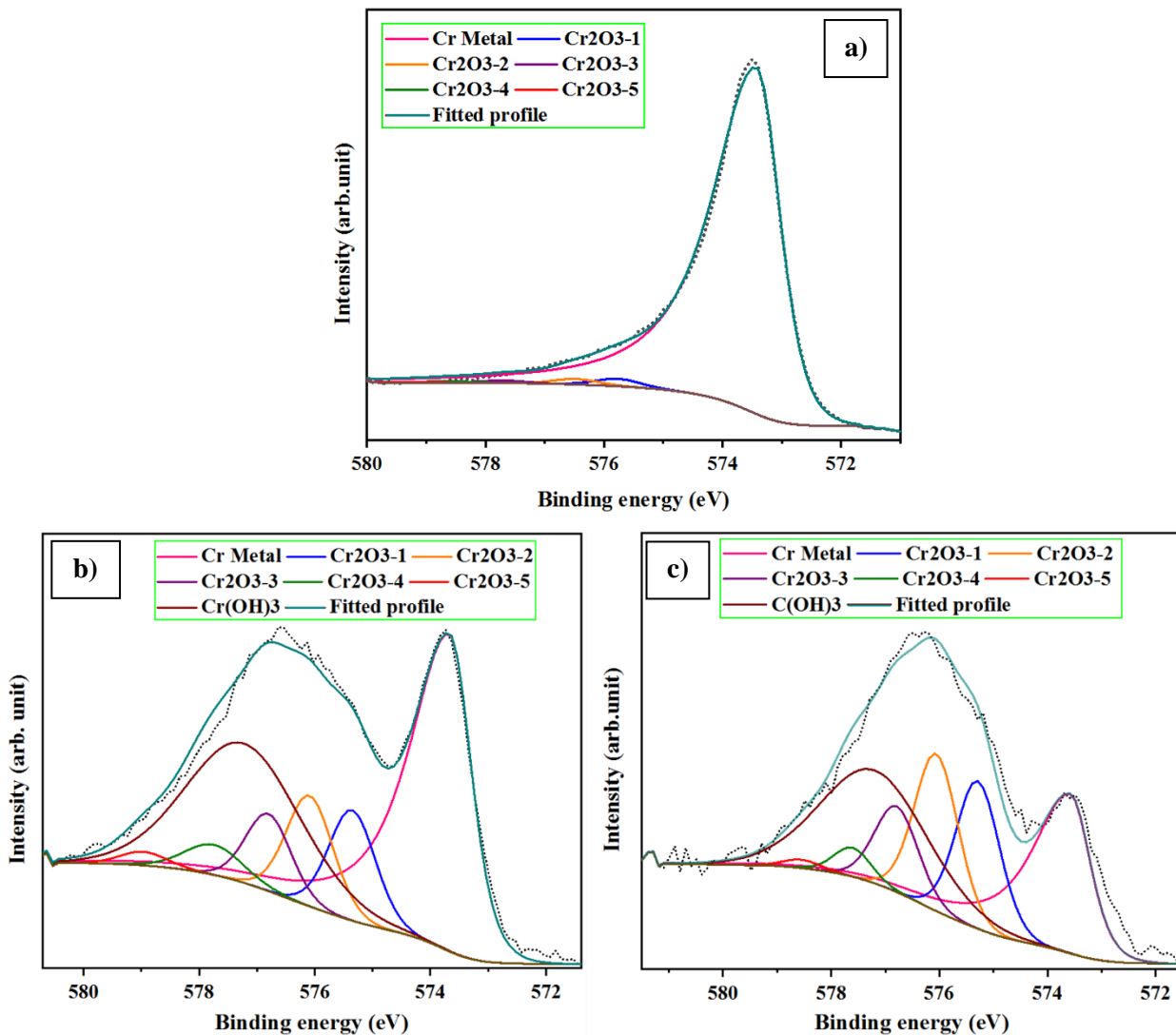
Figure 5.11 Cr 2p high-resolution XPS spectrum of a) Zr4-Cr-Ref; after air-exposed for 50 days: b) 240G-Zr4-Cr-PVD and c) AR-Zr4-Cr-CS (black dotted lines represent original spectra collected from XPS) [152].

Table 5.6 Assignment of the Cr 2p3/2 peak components for all tested samples.

Zr4-Cr-Ref			240G-Zr4-Cr-PVD			AR-Zr4-Cr-CS		
Component	B.E (eV)	Area %	Component	B.E (eV)	Area %	Component	B.E (eV)	Area %
Cr (0)	573.42	97.32	Cr (0)	573.66	42.36	Cr (0)	573.58	26.68
$Cr_2O_3 - 1$	575.77		$Cr_2O_3 - 1$	575.35		$Cr_2O_3 - 1$	575.29	
$Cr_2O_3 - 2$	576.48		$Cr_2O_3 - 2$	576.09		$Cr_2O_3 - 2$	576.06	
$Cr_2O_3 - 3$	577.70		$Cr_2O_3 - 3$	576.80	29.06	$Cr_2O_3 - 3$	576.79	44.30
$Cr_2O_3 - 4$	578.59	2.68	$Cr_2O_3 - 4$	577.75		$Cr_2O_3 - 4$	577.61	
			$Cr_2O_3 - 5$	578.96		$Cr_2O_3 - 5$	578.55	
$Cr_2O_3 - 5$	579.38		$Cr(OH)_3$	577.23	28.58	$Cr(OH)_3$	577.20	29.02

From data presented in Table 5.6, the metallic Cr(0) component identified at a binding energy of ~573.42 eV (Fig. 5.11(a)), and it decreased with aging (Fig. 5.11(b-c)), evidencing the transformation of Cr(0) into higher oxidation states. The deconvolution of the XPS spectra of both exposed samples showed almost similar hydroxide content. However, the metallic Cr(0) component amount was higher in the sample 240G-Zr4-Cr-PVD by 58% compared to AR-Zr4-Cr-CS (Fig. 5.11(b-c)). In addition, XPS survey spectra were collected for Zr4-Cr-Ref, 240G-Zr4-Cr-PVD, and AR-Zr4-Cr-CS, and analyzed data are presented in Table 5.7. A relatively low level of surface carbon (~7.85%) was detected for the Zr4-Cr-Ref sample. However, after 50 days of air exposure, the results indicated that the carbon level on the surface had increased significantly to ~63.15% for 240G-Zr4-Cr-PVD and even higher of ~79.48% for AR-Zr4-Cr-CS. A slightly higher wettability of 240G-Zr4-Cr-PVD after 50 days air exposure (Fig. 5.9(a-b)) can be attributed to the higher amount of Cr(0) measured on the surface and lower adsorption of airborne carbon species onto the clean chromium surfaces. To conclude, the plasma treatments lead to improving the wettability of chromium surfaces, while the exposure to air oxidized the surface leading to the

presence of various Cr(III) species as confirmed by the Pourbaix diagrams. Although Pourbaix diagrams are constructed for aqueous solutions at diluted concentrations of the particular element species, they provide the chemical reactions and the thermodynamically stable phases that form at specific conditions, such as temperature and pH [192-193].

Table 5.7 Chemical composition of sample surfaces acquired from XPS survey spectra.

Sample	Composition at (%)		
	Cr 2p	C 1s	O 1s
Zr-4-Cr-Ref	83.22	7.85	8.93
240G-Zr4-Cr-PVD	4.20	63.15	32.65
AR-Zr4-Cr-CS	1.80	79.48	18.72

As mentioned before, Cr coated zirconium alloys (e.g., Zircaloy-4) and FeCrAl (APMT and C26M) are candidate materials for accident tolerant fuels in light water reactors. These ATF materials should improve environmental resistance under accident conditions and be equal or better than the current material under normal operating conditions. Current results regarding the performance during critical heat flux (CHF) events show that the Cr coated surfaces have higher wettability than the original Zircaloy-4 surfaces. Cr-coated surfaces may improve the thermal-hydraulic performance of the cladding surface, tolerating higher heat fluxes before departure boiling is evidenced. This statement is true for both types of coatings (PVD and Cold Spray); however, Cold Spray coatings may have a slight advantage against PVD from the point of view of CHF and mechanical properties wettability, and probably scalability in the manufacturing process. There is, however, hydrophobic recovery of the surface wettability of Cr-coating during aging in humid air that could result in decreased thermal-hydraulic performance, especially when there is a time delay between testing stages. However, good stability of wetting characteristics was recorded for substrate Zircaloy-4 and FeCrAl alloys, APMT and C26M.

5.4 Summary

In this work, chromium coatings were deposited on Zircaloy-4 substrates by two different coating techniques, PVD and Cold Spray. The properties of both types of coatings were measured through SEM, XRD, nanoindentation, nano-scratch test, and ring compression tests. The X-ray diffraction for both types of coatings confirmed the presence of the chromium with BCC crystalline structure and some texture effects. The ring compression test confirmed the higher mechanical strength of the tubes after the deposition of the coatings. Higher hardness was recorded for both types of coatings compared to that of the substrate Zircaloy-4, which had a hardness value of approximately 3.05 GPa. The adhesion of the coatings to the substrate, assessed by the nano-scratch test, indicated that the Cr coatings adhered well to the Zircaloy-4 substrate, and the results showed increasing adhesion with increasing initial substrate surface roughness. The surface topography was studied by measuring surface roughness quantitatively and qualitatively for all samples. The wettability of each surface was assessed by measuring its contact angle with DI water droplets. A significant enhancement in wettability was logged after the deposition of chromium coating, which may improve thermal-hydraulic performance of cladding material. The spreadability test results confirmed the hydrophilic wetting characteristics of the Cr coating. The ambient aging of the plasma-treated chromium surfaces in air resulted in a significant change in Cr(0) oxidation states to Cr(III), oxides and hydroxides, and the absorption of carbonaceous species, which in turn decreased the wetting characteristics. However, there were negligible changes in wetting characteristics recorded for substrate Zircaloy-4 and FeCrAl alloys, APMT and C26M.

Chapter 6: Microstructure and surface characteristics evolution of ATF after flow boiling testing

6.1 Introduction

Iron-chromium-aluminum alloys, referred to as FeCrAl, have superior oxidation resistance in the event of a severe accident [75]. FeCrAl has excellent environmental resistance characteristics under normal operation both for boiling and pressurized water reactors coolants [77][168][170-171]. These materials have demonstrated higher oxidation resistance in high-temperature steam environments than traditional Zircaloy cladding systems [153]. Similar studies reported extremely low weight change for FeCrAl alloy compared to Zircaloy when exposed to LWR water for a very long-time [78][168]. With outstanding oxidation resistance, FeCrAl has also shown enhancement in thermal-hydraulic performance. For example, in pool-boiling experiments, FeCrAl layers deposited at a substrate temperature of 150 ℃ and a sputtering time of 1 h and FeCrAl deposited at a substrate temperature of 600 ℃ and a sputtering time of 1 h enhanced CHF by 42% and 32%, respectively [117]. In a similar study, oxidized FeCrAl showed almost 39% higher CHF than Zr-4 samples [95]. In steady-state flow boiling experiments, FeCrAl alloy, with higher wettability, demonstrated a 22% and 14% increase in CHF compared to Zircaloy-4 and Inconel 600, respectively [128]. Furthermore, in a pool boiling test, superhydrophilic Cr coating with particulate-nanostructure reported lower HTC compared to hydrophilic lumped-nanostructure of the FeCrAl coating [121]. However, literature on the evolution of surface chemistry and characteristics at the high temperatures of the cladding expected at CHF is limited. It becomes essential to understand the materials' surface chemistry when this event occurs to provide the chemical nature of the oxides formed at the early stage, which leads to knowledge of oxidation mechanisms and kinetics, ultimately explaining materials' performance. For example, Lee et. al. [128] repeated the flow boiling experiment ten times using the same test specimens of FeCrAl, Zircaloy-4, and Inconel 600 and recorded noticeable changes in surface wettability as well as the surface roughness of all materials. Yeom et. al. [223] conducted pool boiling experiments where post-CHF Cr-coated Zirlo® samples showed noticeable enhancement in wettability and a slight increment in surface roughness. Since it is well known that

80

chromium forms chromia when oxidized, direct chromia nanoparticles were coated on nichrome wire surface and reported significant CHF enhancement during pool boiling experiments [118]. The literature has shown that the development of an oxide layer on the surface is responsible for the increased wettability [141-142]. In this study, we studied the surface characteristics and surface chemistry of FeCrAl alloys, Cr-coated Zircaloy-4 produced using PVD and cold spray techniques, before and after flow boiling CHF testing under atmospheric pressure. The surface roughness and wettability were assessed using contact profilometry, AFM, and contact angle goniometry. Furthermore, the materials' microstructure was studied using SEM and XRD. Finally, our detailed surface chemistry analysis of the selected ATF materials, carried out by XPS, evidenced the formation of various oxides during the test. These results elucidate the rapid response of FeCrAl alloys and Cr-coated Zircaloy-4 toward accident scenarios.

6.2 Material and methods

CHF experiments were led by University of Wisconsin – Madison Thermal Hydraulic Lab and the details of the experimental work is given in the flow boiling research published by this Lab [253-254]. The ATF materials, AR-Zr4, 600G-Zr4-Cr-PVD, AR-Zr4-Cr-CS, APMT, and C26M were first characterized at VCU and then transferred to UW for thermal-hydraulic experiments. Once samples were tested for CHF measurements, the samples were sent back to VCU for post-CHF characterization. Fig. 6.1 shows the flow boiling CHF facility used for this study. Instrumented heater rods were fabricated from ~450 mm long ATF cladding tubes for direct heating via an applied current with a uniform power profile. The experiment was conducted using water as the working fluid at atmospheric pressure, with 76 °C of subcooling, and at a flow rate of 750 kg/m^2. Although this system is designed to shut down the power supply immediately when it reaches the CHF condition, the cladding temperature rises to sufficiently high temperatures for oxide layers to grow. For example, Fig. 6.1 shows how the samples oxidized and partially melted after reaching the CHF point. A list of samples with their identification and descriptions is provided in Table 6.1.

81
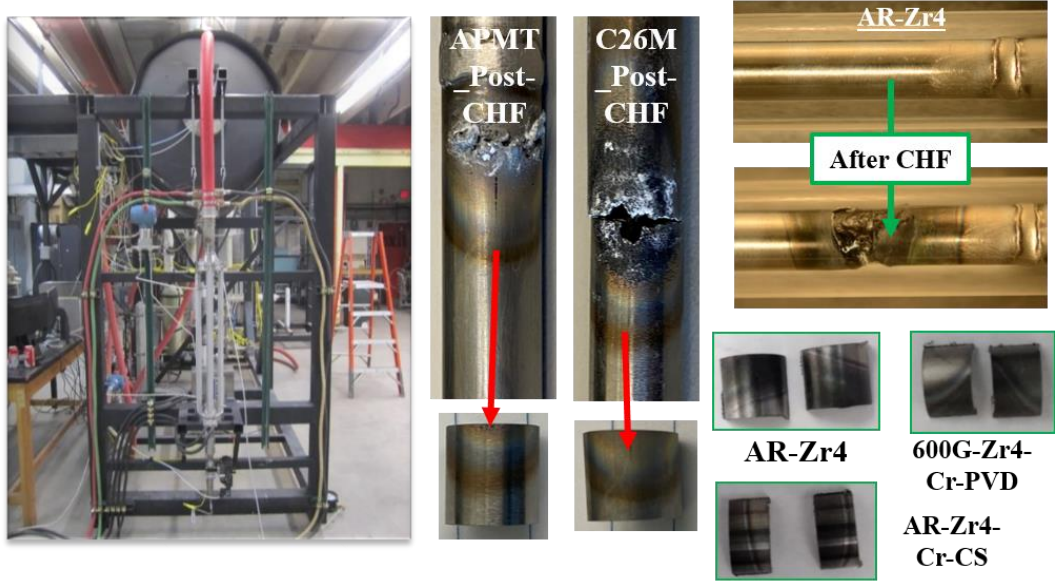
Figure 6.1 CHF testing: Flow boiling atmospheric pressure test loop (left) and post-CHF samples (right).

Table 6.1 Test sample identification (ID) with their conditions.

Sample ID	Conditions
600G-Zr4-Cr-PVD	Cr-coating deposited using PVD technique on Zr-4 substrate ground using 600 grit SiC abrasive paper
AR-Zr4-Cr-CS	Cr-coating deposited using Cold Spray technique on Zr-4 substrate ground using 320 grit SiC abrasive paper
APMT_Pre-CHF	As received APMT sample before flow boiling test
C26M_Pre-CHF	As received C26M sample before flow boiling test
APMT_Post-CHF	APMT sample tested in flow boiling CHF test
C26M_Post-CHF	C26M sample tested in flow boiling CHF test

6.3 Result and discussion

6.3.1 Surface characterization for post-CHF Cr-coated Zircaloy-4

The results presented in the previous chapter (aging effect) demonstrated the evolution of wettability of Cr-coated surfaces with aging time under atmospheric conditions. The surface characteristics, such as wettability and roughness of this kind of material as ATF cladding, must be carefully assessed when evaluating their influence on heat transfer parameters such as CHF and heat transfer coefficients (HTC). Given the dynamic change of the surface chemistry, the wettability of Cr-coated surfaces may be altered due to different species present at the time of testing. With this understanding of aging effects, flow boiling CHF tests were conducted for substrate Zircaloy-4 and both types of Cr-coated samples after aging. These aged tubes were chosen for testing as this would be expected in a real case scenario, where plasma etching before using the fuel cladding might not be viable.

For the CHF experiment, the three different samples, AR-Zr4, 600G-Zr4-Cr-PVD, and AR-Zr4-Cr-CS were used. Sample selection for the CHF test, especially for PVD coating, was based on two criteria, the surface roughness of 600G-Zr4-Cr-PVD is very similar to commercial cladding, and improved adhesion strength of the coating compared to AR-Zr4-Cr-PVD. The tests were repeated twice for all three tested samples, and the average CHF values for AR-Zr4, 600G-Zr4-Cr-PVD, and AR-Zr4-Cr-CS were 2.63 MW/m^2, 2.58 MW/m^2, and 2.31 MW/m^2, respectively. Only a slight drop of CHF of ~2% was recorded for 600G-Zr4-Cr-PVD, while a significant drop of ~12% in CHF value was evidenced for AR-Zr4-Cr-CS compared to the substrate sample AR-Zr4. In particular, the wettability effect on CHF was clearly described in various reports [194-195]. In boiling heat transfer, CHF refers to the limit heat flux for surface failure by an abrupt increase of surface temperature. This abrupt increase in surface temperature is generated by a vapor film formation which disturbs heat transfer to the liquid. Therefore, in a surface with low wettability, the liquid supplying capability is low, so it is hard to remove the vapor film on the surface, resulting in a low CHF [194-195]. In this study, the CHF testing results showed that the CHF was reduced, compared to AR-Zr4, 11.5% for AR-Zr4-Cr-CS having the lowest wettability and

10.5% for 600G-Zr4-Cr-PVD. However, roughness has the opposite effect on the heat transfer coefficient, and as seen in Fig. 6.2, where an improvement of HTC was measured for the Zr-Cr-CS (AR-Zr4-Cr-CS). It is well known that HTC is closely related to the micro-roughness of the surface. In fact, many studies have shown that HTC can be improved for both pool and flow boiling by modifying the surface through polishing or applying a specific coating to increase micro-roughness of the surface under study [95][196][257-258]. A cartoon in Fig. 6.2 explains how the micro-roughened surface has a higher density or micro-cavities to serve as sites for bubble nucleation. As a result, small and fast bubble nucleation occurs on the entire surface, increasing the HTC.
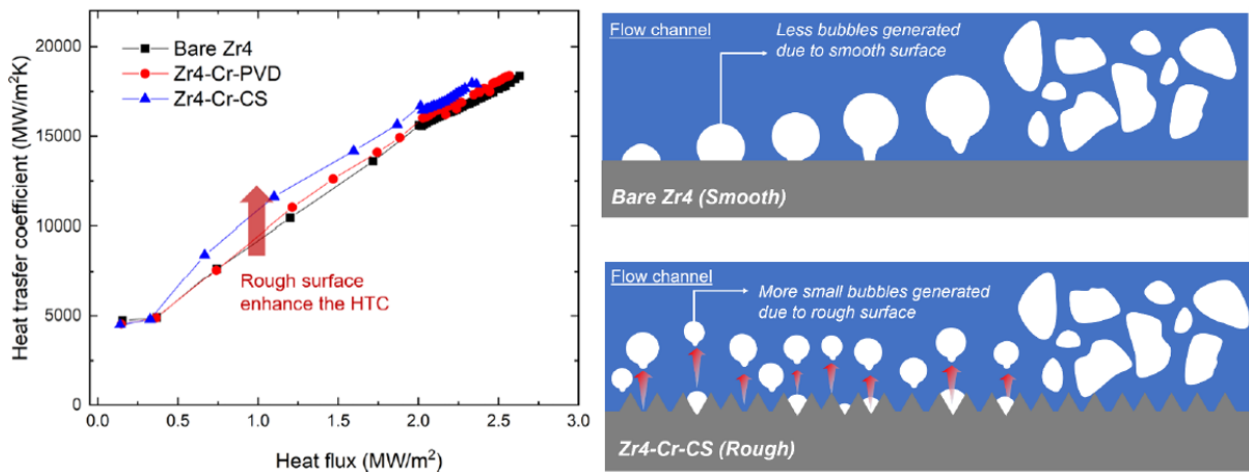
Figure 6.2 Comparison of average heat transfer coefficient on the bare Zr-4 (AR-Zr4), Zr4-Cr-PVD (600G-Zr4-Cr-PVD), and Zr4-Cr-CS (Ar-Zr4-Cr-CS) with a cartoon showing bubble formation on smooth and rough surfaces [259].

Literature has shown the impact of an evolving surface structure in CHF events [128][141-142]. Thus, the surface wettability of the post-boiling samples was measured, and the average contact angle data is presented in Fig. 6.3(a). The measurements taken after the tests indicate a slight increase in the contact angle of 600G-Zr4-Cr-PVD, whereas a noticeable increase in wettability was recorded for both the AR-Zr4 and AR-Zr4-Cr-CS samples. The formation of surface oxides during the boiling test is

considered the reason for the observed wettability increase. To support this wettability trend, droplet spreading tests were performed for all CHF tested samples following the same procedure explained in Chapter 3. As shown in Fig. 6.3(b), both 600G-Zr4-Cr-PVD and AR-Zr4-Cr-CS showed poor wetting characteristics during spreading studies after the CHF tests.
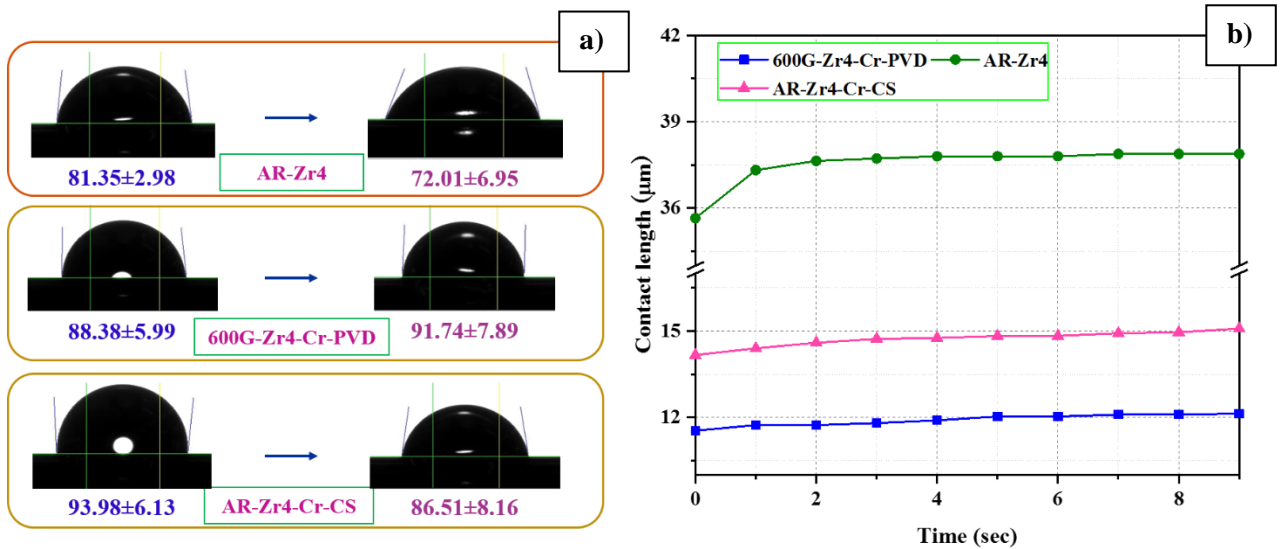
Figure 6.3 Wettability after CHF testing: a) Comparison of static contact angle data for all samples and b) Droplet spreading study for all samples [152].

To further investigate the surface roughness characteristics of the CHF-tested samples, AR-Zr4, 600G-Zr4-Cr-PVD, and AR-Zr4-Cr-CS roughness measurements were collected using the stylus profilometer. The average Ra values of 10 scans are presented in Fig. 6.4 with their standard deviation. The results indicate a slight increase in the surface roughness for the post-CHF samples. Additionally, XPS survey spectra for both post-CHF Cr-coated samples were analyzed, and results are presented in Table 6.2. The spectrum from Cold Spray Cr coating shows a relatively higher level of chromium (~31%) attributed to oxides. However, the PVD Cr coating demonstrated a large amount of carbon (~67%) on the surface. The observed decrease in the wettability of PVD coating after the CHF test could, in part, be attributed to the adsorption of airborne carbon species onto the chromium surfaces. This could be

attributed to a large number of nanoscale features on the PVD coating surface compared to the Cold

Spray coating, as shown in Fig. 5.5. A large number of nanoscale features would increase overall surface

area, leading to higher absorption of surface contaminants for PVD coatings. The effect of surface

contaminants on wettability has been reported in the literature [198-200][227].
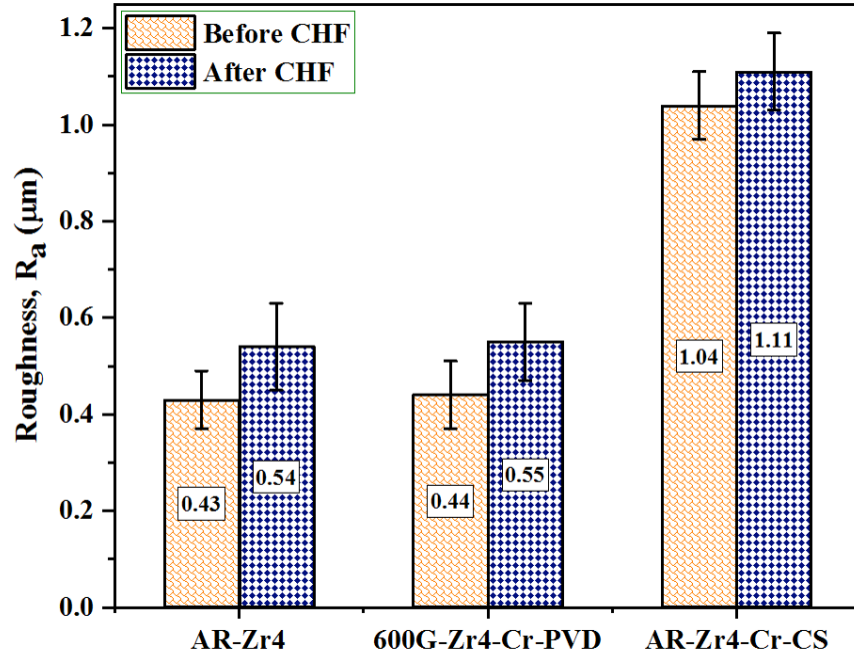
Figure 6.4 Average surface roughness parameter (Ra) for all samples before and after CHF testing

[152].

Table 6.2 Data calculated from the XPS survey spectra obtained from both type of Cr-coated

samples after CHF testing.

Post-CHF Sample	Composition at (%)		
	Cr 2p	C 1s	O 1s
600G-Zr4-Cr-PVD	5.17	67.96	26.87
AR-Zr4-Cr-CS	30.93	27.15	41.92

6.3.2 Study of microstructure and surface characteristics for pre- and post-CHF FeCrAl samples

The flow boiling tests for FeCrAl alloy samples, APMT and C26M, were performed to record CHF events. The CHF of APMT and C26M samples were 2.54 MW/m^2 and 2.26 MW/m^2, respectively. Tested FeCrAl samples after the flow boiling test are shown in Fig. 6.5 and their IDs are listed in Table 6.1. The SEM images of FIB-prepared cross-section for APMT_Post-CHF and C26M_Post-CHF are shown in Fig. 6.5. A thin Pt layer was deposited on the sample surfaces to protect the oxide layer from any damage during the milling process. These micrographs evidenced the formation of an oxide layer after flow boiling testing for both FeCrAl alloys. The oxide layer, indicated by red arrows, was ~90 nm thick for APMT_Post-CHF (Fig. 6.5(a)), while a thicker layer of ~173 nm was observed for the C26M_Post-CHF (Fig. 6.5(b)).
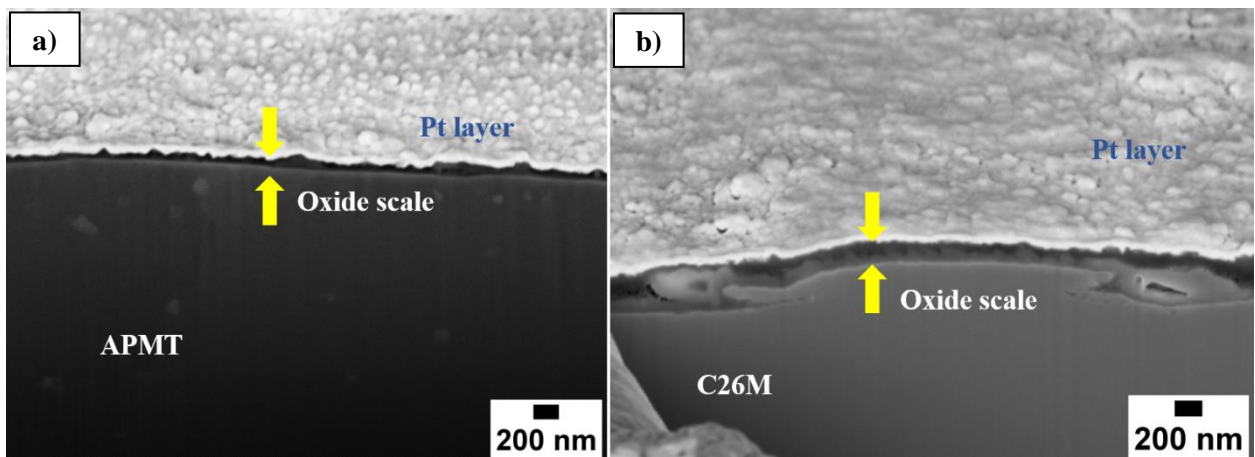
Figure 6.5 Cross-sectional SEM images of FeCrAl samples after CHF testing: a) APMT_Post-CHF and b) C26M_Post-CHF (cross-sections were milled near blue region on sample surface showed in Fig. 6.1).

The surface roughness measurements recorded by contact profilometry and AFM for both FeCrAl alloys before and after CHF testing are shown in Table 6.3. The surface roughness parameter Ra for APMT_Pre-CHF (0.4 μm) is very similar to that of commercial cladding Zircaloy-2 and Zircaloy-4 [263].

In contrast, Ra of C26M was twice that of APMT_Pre-CHF. Furthermore, the surface of the C26M_Pre-CHF, compared to that of APMT_Pre-CHF, had a higher Rz value, accompanied by a larger RSm, indicating a high average distance between two profile elements. Both FeCrAl samples evidenced a slight increase in the surface parameters after CHF testing. This result may be attributed to the oxide formation on the tubes' surface during the flow boiling testing [128][264]. AFM scans for the FeCrAl samples before and after CHF testing are shown in Fig. 6.6(a-d). At the nanoscale, the surface of the C26M_Pre-CHF sample appears rougher compared to the APMT_Pre-CHF. Similarly, post-CHF samples evidenced an increased surface roughness compared to their corresponding pre-CHF samples, supporting the results found in contact profilometry. The roughness parameter Ra and roughness factor r, measured by AFM, were recorded for three scans from each sample, and the average values are presented in Table 6.3. The measurements showed a Ra of 205 nm for APMT_Pre-CHF, while it was 454 nm for C26M_Pre-CHF. Insignificant changes in roughness values were recorded after CHF testing.

Table 6.3 Roughness measurements for both types of FeCrAl surfaces before and after CHF testing.

Sample	Contact profilometry measurements (μm)			AFM measurements (nm)	
	Ra	Rz	RSm	Ra	r
APMT_Pre-CHF	0.40±0.09	3.89±0.99	70.11±7.24	205	1.02
APMT_Post-CHF	0.47±0.08	4.68±1.03	76.86±8.22	243	1.03
C26M_Pre-CHF	0.80±0.12	8.75±1.65	130.27±22.73	454	1.02
C26M_Post-CHF	0.90±0.10	9.62±1.83	138.86±22.92	550	1.04
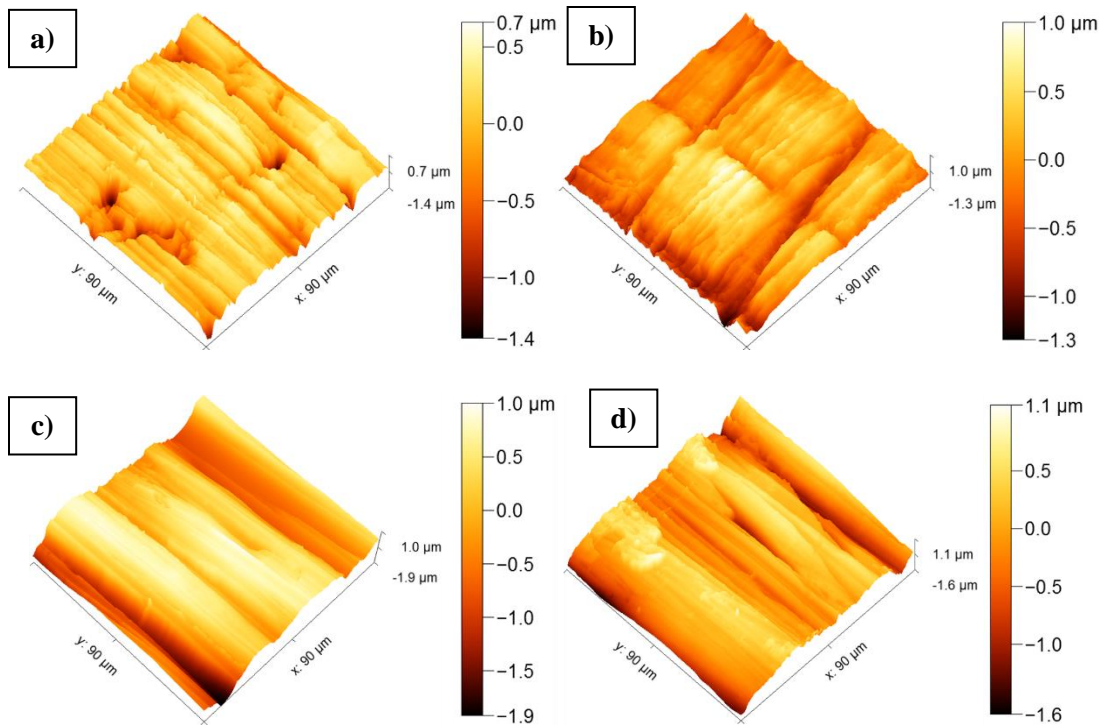
Figure 6.6 AFM surface topography for as received: a) APMT_Pre-CHF, b) APMT_Post-CHF, c) C26M_Pre-CHF and d) C26M_Post-CHF (note that a and b & c and d do not correspond to the same region in the sample).

A comparison of wettability, characterized by measuring static contact angle for both FeCrAl types, is shown in Fig. 6.7(a). The C26M demonstrated a lower contact angle than the APMT sample before the CHF testing. For hydrophilic surfaces, the influence of surface roughness on wetting and the spreading phenomena has been evidenced in the literature [186][201-203][216][219]. An explanation for this phenomenon is that the large scratches on the surface possibly start to wick a droplet, causing additional movement of the triple contact line. Furthermore, a lower contact angle was logged for both FeCrAl alloys Post-CHF. Similar behavior was observed in our results show in previous sections, where the increase in surface roughness after CHF testing led to an increase in the material's wettability. Fig. 6.7(b) shows the evolution of the drop base diameter or contact length over the surface on the second timescale for all FeCrAl samples. According to these results, a water droplet spreads faster on the C26M_Pre-CHF

89

than APMT_Pre-CHF, which can be understood by the lower surface roughness and higher contact angle

of APMT_Pre-CHF. However, the spreading of APMT_Post-CHF was high among all tested samples.
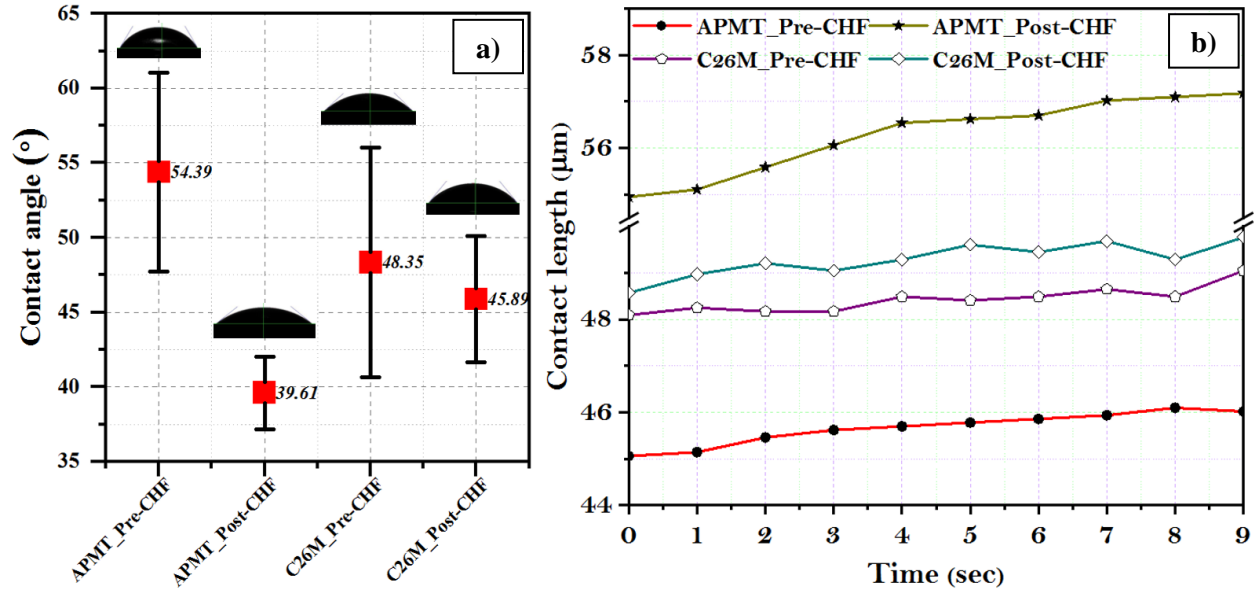
Figure 6.7 Wettability: a) Comparison of static contact angle for all samples, and b) Comparison of droplet spreading for FeCrAl alloys before and after CHF test.

The surface chemistry of the FeCrAl samples after CHF testing was investigated with XPS. The

samples were sputtered at selected time (2 min) intervals to obtain the compositional depth profiles, 150

cycles for APMT_Post-CHF (total sputtering time of 300 min) and 200 cycles for C26M_Post-CHF (total

sputtering time of 400 min). Due to the presence of different species in the surface layer and the shallow

depth at the end of sputtering, the sputtering rate (nm/min) was difficult to quantify. However, it is known

that the relative sputtering rate depends on the material nature. For example based on the literature,

sputtering rate under certain ion beam conditions can be classified as: $C > SiC > SiO_2 > Fe_3O_4 > Cr_2O_3$

[265-269]. The compositional depth profile results of APMT_Post-CHF and C26M_Post-CHF are shown

in Fig. 6.8. The high or equal oxygen-to-metal ratio in the APMT_Post-CHF sample (Fig. 6.8(a)) was

evident up to about 80 min of sputtering, while it was observed up to 250 min of sputtering for the

C26M_Post-CHF sample (Fig. 6.8(b)). This result is in good agreement with the thickness of the oxide layers obtained in cross-sectional SEM images in Fig. 6.5. A thin Si-rich layer was identified in the profile for both samples. It is thought that the thin Si-rich layer was formed either as a result of Si contaminants in the flow boiling facility during testing or from Si residues in the material itself. During depth profiling, the high-resolution XPS spectra of Al2p, Fe2p, and Cr2p were collected at different depths and deconvoluted to elucidate their chemical state. Fig. 6.9 and Fig. 6.10 show the deconvoluted spectra for both APMT_Post-CHF and C26M_Post-CHF, respectively. Additionally, high-resolution spectra for pre-CHF samples, APMT_Pre-CHF and C26M_Pre-CHF, were collected to serve as a reference (Fig. 6.11). In all high-resolution spectra, black dotted lines represent original spectra collected from XPS, and the thin brown line is the fitted profile. The positions, in binding energy, and intensities of the peaks associated with each element allowed the identification of their oxidation states [240-250][270-277]. The fitting of all XPS patterns in this work was treated with a multi-peak [250-252].
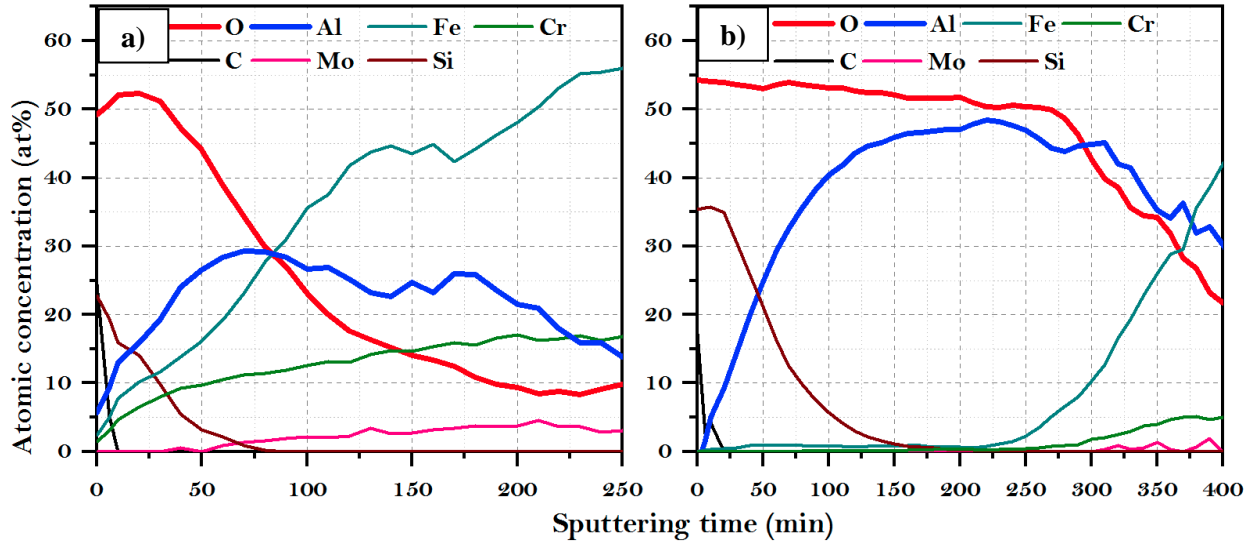
Figure 6.8 Element composition vs. depth (sputter time) profile on the post-CHF samples surface: a) APMT_Post-CHF and b) C26M_Post-CHF sputtering using Ar+ ion with 3 keV beam energy.
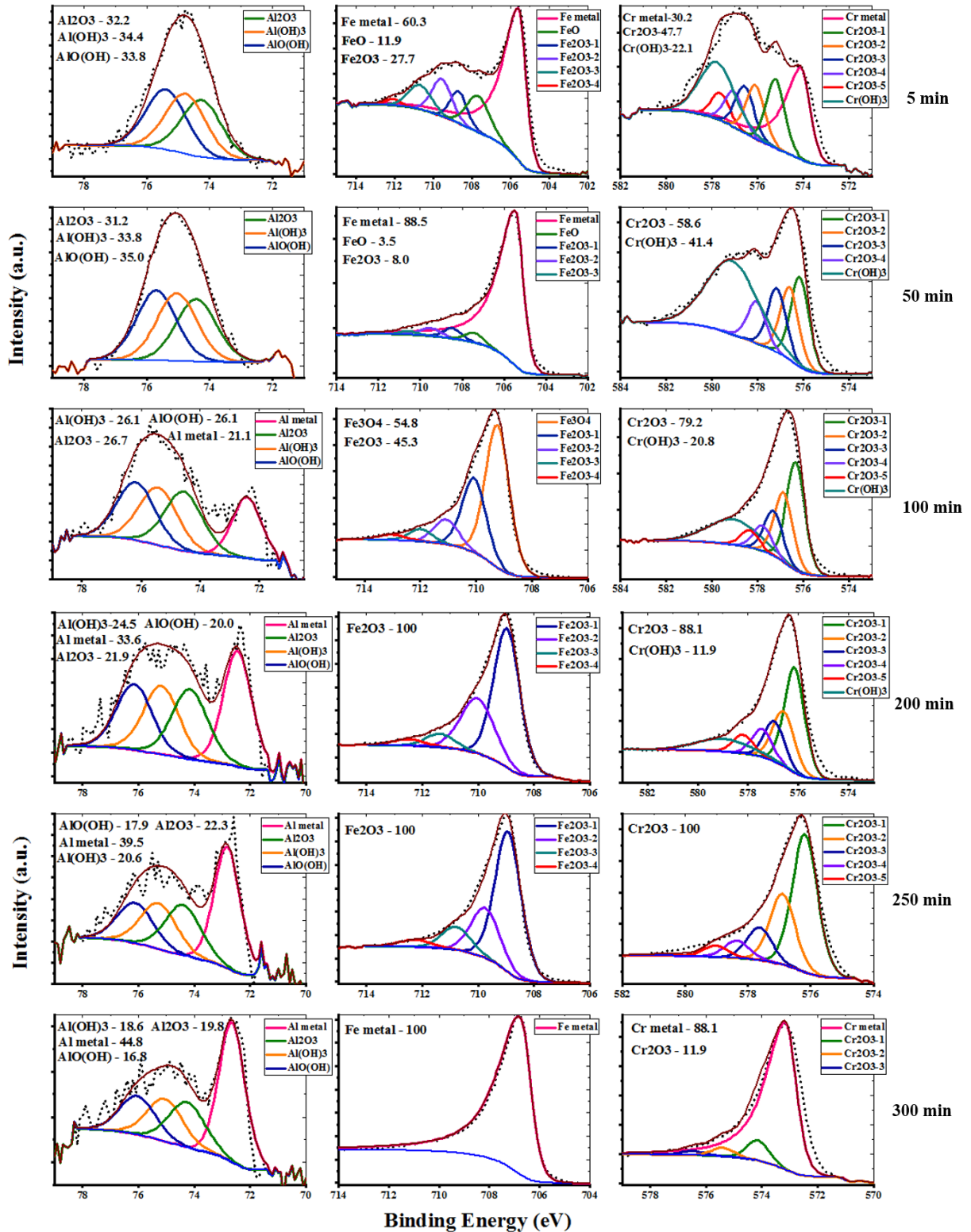
Figure 6.9 XPS high-resolution spectra for Al2p, Fe2p and Cr2p at various depths for the APMT_Post-CHF sample (each present species were calculated in %area).
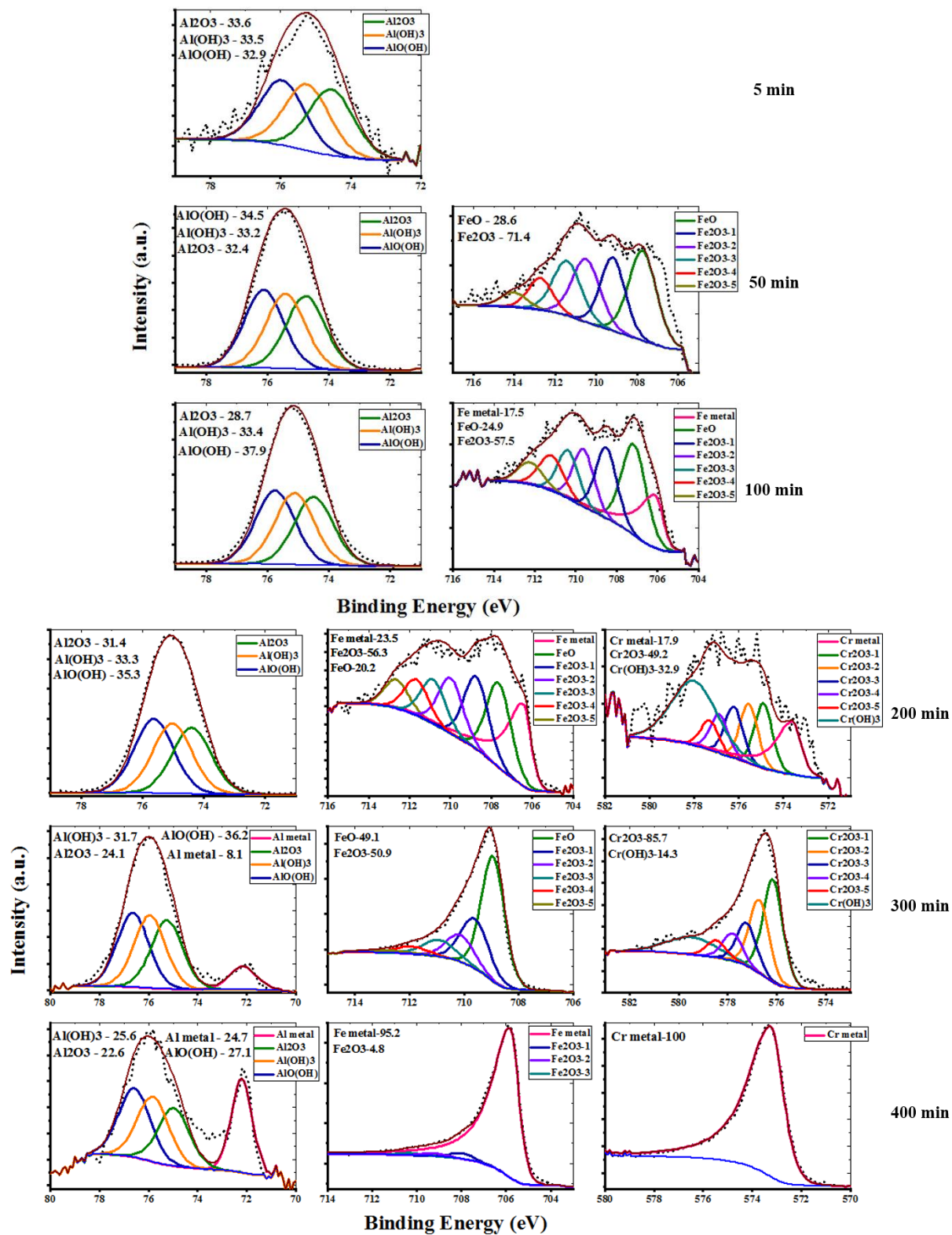
Figure 6.10 XPS high-resolution spectra for Al2p, Fe2p and Cr2p at various depths for the C26M_Post-CHF sample (each present species were calculated in %area).
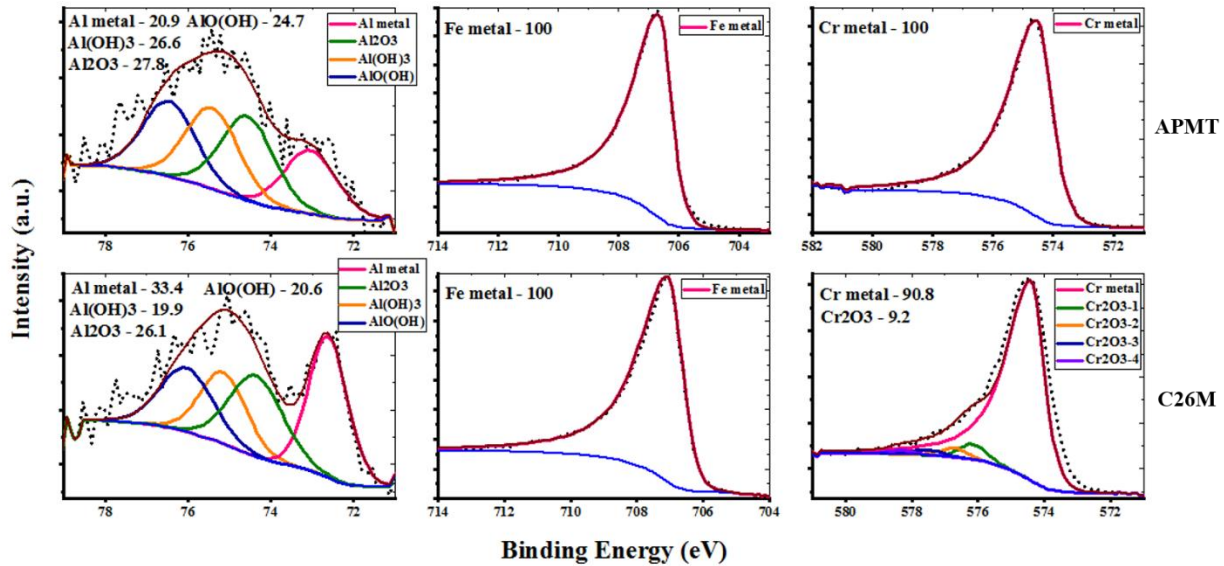
Figure 6.11 XPS high-resolution spectra for Al2p, Fe2p and Cr2p for the APMT_Pre-CHF and C26M_Pre-CHF samples (each present species were calculated in %area).

Fig. 6.13 gives a graphical representation of all high-resolution XPS spectra collected during depth profiling. In these graphs, X-axis reads sputtering times at which high-resolution spectra were collected. When samples were tested in the flow boiling system, working fluid (DI water) would take a series of reactions on the surface, including oxidation and adsorption. Oxidation products include Al_2O_3, $Al(OH)_3$, $AlO(OH)$, FeO, Fe_2O_3, Fe_3O_4, Cr_2O_3, and $Cr(OH)_3$. Reactions among Fe, Cr, Al, and O were dependent on the distribution of elements on the surface. Competitive relation existed among oxidation reactions. For the APMT_Post-CHF sample, mixed oxide film in the first stage of sputtering (5 min in Fig. 6.13(a)) was mainly composed of Al oxides and hydroxides with a noticeable amount of Fe, Cr, and their corresponding oxides and hydroxides. In contrast, in the C26M_Post-CHF sample, the layer was detected with only aluminum oxides and hydroxides (Fig. 6.13(b)). It was assumed that after a thin layer of pure/mixed oxide film formed on the surface, the oxidation reactions between O^{2-} and metal elements on the surface ended. However, because of the existence of mixed oxide film, internal diffusion of O^{2-} was enough to produce more Al_2O_3, $Al(OH)_3$, $AlO(OH)$, Fe_2O_3, Fe_3O_4, and Cr_2O_3. Thus, the oxidation process results from adsorption, ionization, and diffusion of oxidizing species. In the sputtering time between 5 to

95

100 min, the presence of Al$_2$O$_3$, Al(OH)$_3$, and AlO(OH) was predominant for both post CHF samples. The possible reactions of Al with water generates the products identified in this work, which are thermodynamically favorable from room temperature to temperatures even above the aluminum melting point of 660 ℃ [278]. The aluminum hydroxides are the precursors of alumina, and their thermodynamical stability as a function of temperature has indicated that the higher the temperature, the lower the degree of hydration [278]. Dinge et. al. [278] explained the stability of compounds with different stoichiometries by writing [Al$_2$O$_3$,xH$_2$O] with x varying between 0, correspond to α-alumina and 3 for trihydroxides. Thus, the equilibrium between a hydroxide and α-alumina can be written as follows:

$$\alpha - Al_2O_3 + xH_2O \; \leftrightharpoons \; [Al_2O_3, xH_2O] \tag{6.1}$$
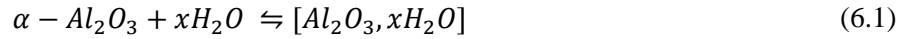
and the corresponding variation of the Gibbs free energy is

$$\Delta G(T) = G^{(s)}_{[Al_2O_3, xH_2O]} - G^{(s)}_{\alpha-Al_2O_3} - xG^{(1/g)}_{H_2O} \tag{6.2}$$

Assuming that the entropic contributions for the solid phases can be neglected versus the contributions of water, $G^{(s)}_{[Al_2O_3, xH_2O]}$ and $G^{(s)}_{\alpha-Al_2O_3}$ will be approximated by their internal energy calculated at 0 K. The expression of $G^{(1/g)}_{H_2O}$ can be expressed as follows according to T. For T<373 K,

$$G^{(1/g)}_{H_2O} = E^{(g)}_{H_2O} - \Delta H^{vap}_{H_2O} - TS^{(1)}_{H_2O} \tag{6.3}$$

Here, $E^{(g)}_{H_2O}$ is the internal energy of one isolated water molecule, $\Delta H^{vap}_{H_2O}$ and $S^{(1)}_{H_2O}$ can be found in thermodynamic tables [279]. For T<373 K,

$$G^{(1/g)}_{H_2O} = E^{(g)}_{H_2O} - TS^{(1)}_{H_2O} \tag{6.4}$$

and the variation of the Gibbs free energy for the reaction 6.1 is approximated by

$$\Delta G(T) \simeq G^{(s)}_{[Al_2O_3, xH_2O]} - G^{(s)}_{\alpha-Al_2O_3} - xE^{(g)}_{H_2O} - xTS^{(1)}_{H_2O} \tag{6.5}$$
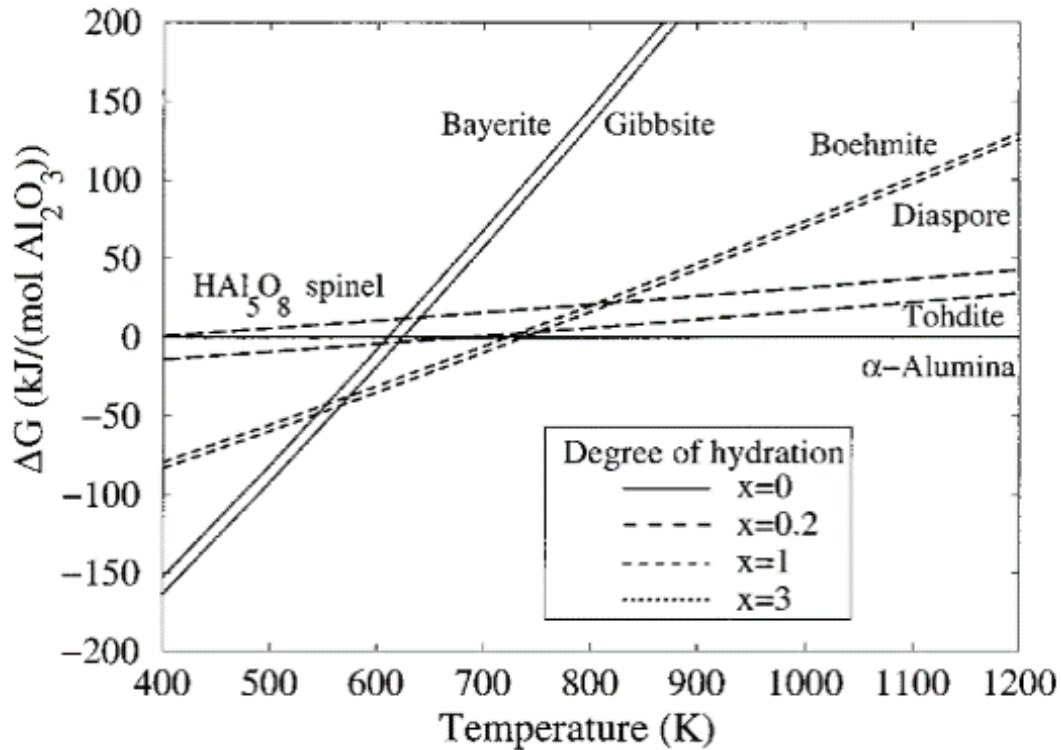
Figure 6.12 Gibbs free energy of the different aluminum hydroxides compared to α-Al₂O₃ (see equation 6.2), as a function of temperature [278].

The Fig. 6.12 shows the stability domains of Al(OH)$_3$ (Bayerite and Gibbsite), AlO(OH) (Boehmite and Diaspore) and Al$_2$O$_3$ as a function of temperature for T greater than the vaporization temperature of water. For given T, the lowest value of ΔG gives the stable phase. However, the straight lines correspond to α-Al$_2$O$_3$. The phase stability diagrams indicate three different domains i) Al(OH)$_3$ is the most stable product from room temperature to 280 ℃, ii) AlO(OH) is the most stable in the temperature range from 280 to 480 ℃ and iii) Al$_2$O$_3$ is the most stable product above 480 ℃. According to the stability diagrams, our results indicate that the analyzed region in the material reached a temperature high enough to promote alumina formation, but this phase did not fully develop as the test was stopped when the CHF was reached. Thus, the fraction of the different products in the material surface is AlO(OH)>Al(OH)$_3$>Al$_2$O$_3$. The C26M_Post-CHF samples also showed FeO and Fe$_2$O$_3$, along with the aluminum oxides/hydroxides, with no evidence of Cr oxides. For the APMT_Post-CHF sample, at depths given by the sputtering times

from 100 min to 250 min, the formation of Fe_2O_3 was favored. A similar effect was seen for the C26M_Post-CHF sample during sputtering times between 200 to 300 min. For both samples, at the highest sputtering time used in this experiment, when the concentration of O^{2-} at the interface (mixed oxide film/matrix) was too low to promote oxide formation, it led to negligible amounts of Al and Cr oxides in APMT_Post-CHF sample and some Al and Fe oxides in C26M_Post-CHF sample. At this point, the area percentage of all elements and their species at different valence states are almost similar to the results of deconvoluted high-resolution spectra of pre-CHF FeCrAl samples, shown in Fig. 6.11.

Figure 6.13 Oxidation behavior diagram of FeCrAl after CHF testing: a) APMT_Post-CHF and b) C26M_Post-CHF.

The results presented in this section demonstrated the evolution of FeCrAl surface chemistry after flow boiling CHF testing under atmospheric conditions. The surface characteristics, such as wettability and roughness of this kind of material as ATF cladding, must be carefully assessed when evaluating their influence in heat transfer parameters such as CHF. Our results discussed above indicate that CHF tested

samples evinced improved wettability of the sample, possibly the consequence of the presence of various oxide and hydroxides species. After flow boiling CHF testing, these changes on FeCrAl alloy surface chemistry can be considered responsible for increasing surface wettability. In contrast, in our previous section, the observed decrease in the wettability of Cr-coated Zircaloy-4 (coated using PVD coating technique) after the CHF test was attributed to the adsorption of airborne carbon species onto the chromium surfaces. However, in this study, a negligible amount of surface contaminations was recorded for FeCrAl samples after CHF testing, contributing to the hydrophilic characteristics of the exposed samples. Similar studies have also been reported in the literature [198-200][227].

Fig. 6.14(a) shows the engineering stress and strain curve from the ring compression test. An inset picture of the FeCrAl tubes before and after compression is also added here with load dies. The stress-strain curves followed a similar trend for both types of FeCrAl alloys before and after CHF testing. Before CHF testing, the APMT_Pre-CHF sample evidenced higher yield strength (the yield strength values are selected at the points where the strains are equal to 0.2%) and peak load than C26M_Pre-CHF (Table 6.4), which agrees with results in the literature for FeCrAl alloys with different Al and Cr content [88][164]. The overall strength of both APMT_Post-CHF and C26M_Post-CHF was found to be higher than the Pre-CHF testing samples. Fig. 6.14(b) compares hardness measurements before and after CHF testing for both types of FeCrAl alloy taken with 0.98 N load. The hardness of APMT was almost 30 % higher compared to the C26M sample, which may be attributed to the higher Cr content in APMT compared to C26M [164][280-282]. After CHF testing, the hardness of both FeCrAl alloys slightly increased. The hardness values of FeCrAl alloys obtained herein are comparable with previous reports [88][283-284].
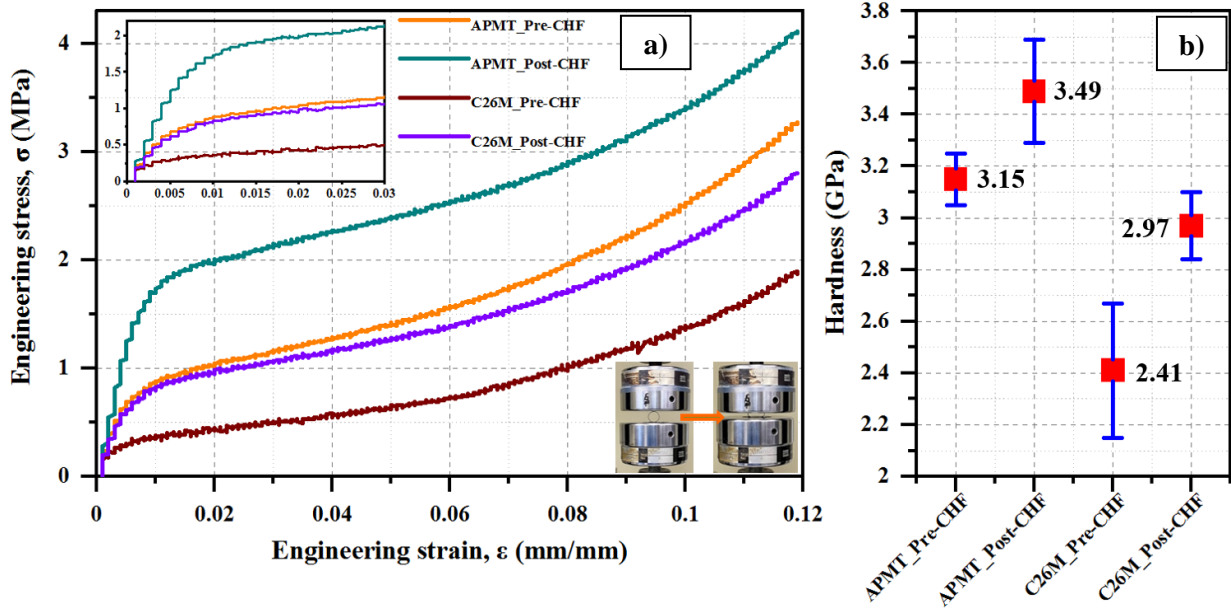
Figure 6.14 Comparison of mechanical properties of FeCrAl alloys before and after CHF testing: a) Ring compression tests and b) Microindentation tests.

Table 6.4 Ring compression test results before and after CHF testing.

Sample	Parameter	
	Peak load (N)	Yield strength (Mpa)
APMT-Pre_CHF	156	0.90
APMT-Post_CHF	188	1.76
C26M-Pre_CHF	97	0.38
C26M-Post_CHF	153	0.83

The XRD patterns of the FeCrAl alloys before and after CHF testing are presented in Fig. 6.15(a). According to peak analysis based on the ICDD database (ICDD pdf #00-054-0387), the diffraction peaks for all samples were observed at $2\theta^o$ of 44.27º, 64.38º, and 81.40º, which confirm the BCC crystal structure [87][285]. The peaks in the XRD pattern of the C26M-Pre_CHF sample compared to those in APMT-Pre_CHF showed up at slightly lower angles, which may be due to the higher Al content (Fig.

100

6.15(a)). According to the Bragg equation, $2d\sin\theta=n\lambda$ (where d, θ, n, λ are lattice parameter, diffraction angle, diffraction series, and beam wavelength, respectively), a decrease of diffraction angle is induced by the increase of the lattice parameter when the diffraction series and beam wavelength are fixed [286]. The increase in lattice parameter with the Al content results from the larger atomic radius of Al compared to Fe [287-288]. Furthermore, a close inspection of the XRD peak profiles indicated a variation of the FWHM for Post-CHF specimens. The calculated FWHM, using Voigt curve fitting [289], for the (110) peak for both post-CHF FeCrAl samples are shown in Fig. 6.15(b). The results indicate a significant decrease in FWHM of the peaks for both FeCrAl samples after CHF testing, which can be attributed to a reduction in dislocation density and residual stresses. This observation correlates with the mechanical properties of the materials post-CHF [290]. The slight shifting of (110) peak for the post-CHF FeCrAl has been attributed to minor displacements of the sample from the center of the XRD goniometer due to their curved geometry [291].
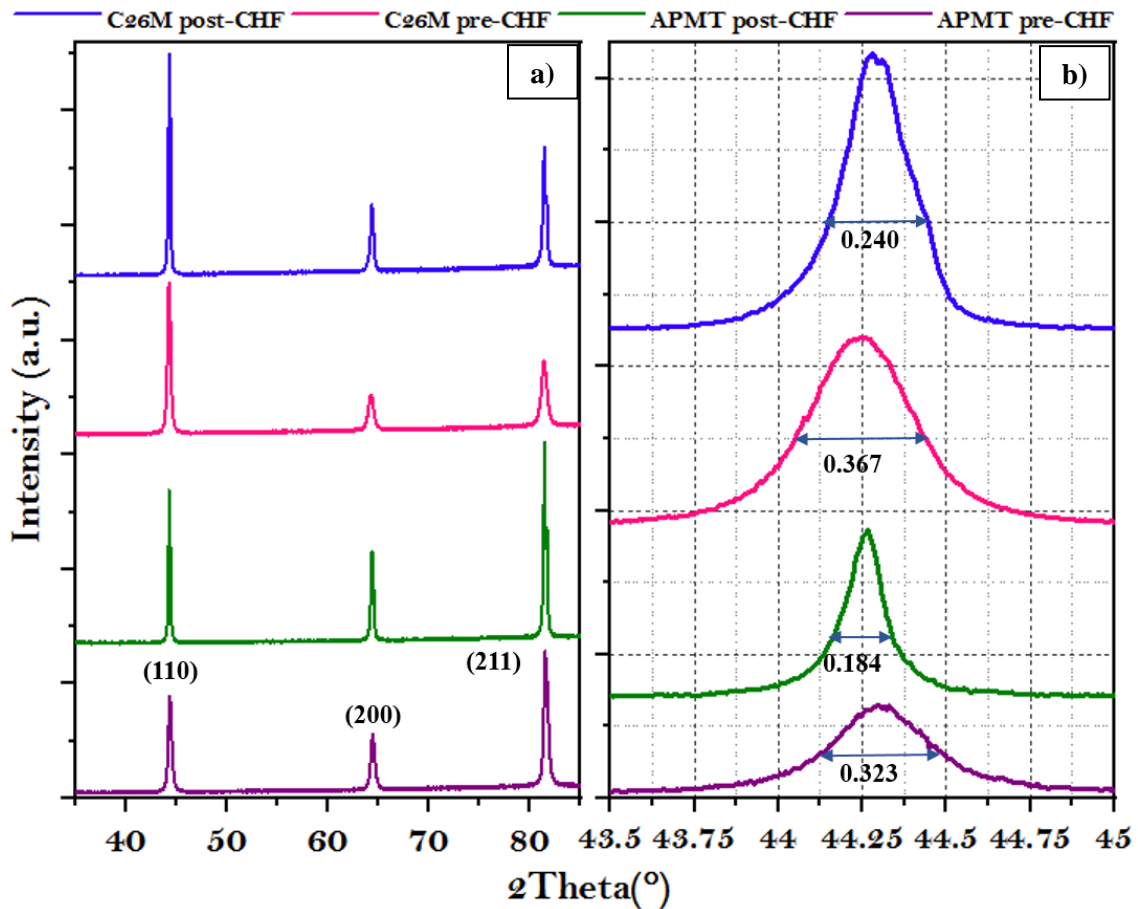
Figure 6.15 X-ray diffraction pattern of the FeCrAl alloys before and after CHF testing (a) and showing effect of CHF testing on peak broadening (b).

The grain size of all FeCrAl samples, APMT_Pre-CHF, C26M_Pre-CHF, APMT_Post-CHF, and C26M_Post-CHF, was determined using the SEM cross-sections. Fig. 6.16(a-b) shows the micrographs of the APMT_Pre-CHF and C26M_Pre-CHF previously etched to reveal grain boundaries. The measured average grain-size of the samples before CHF testing was 7.78±3.38 μm for APMT_Pre-CHF and 46.92±15.42 μm for C26M_Pre-CHF. The significant difference in grain size is due to the different fabrication methods: traditional melting and forging for C26M and powder metallurgy process for APMT [171][292]. Additionally, the lattice constant of ferrite increases with the Al content due to the larger atomic radius of Al compared to Fe, which enhances atomic diffusion and promotes grain growth during solidification [288]. With comparatively smaller grain size, the APMT has evidenced higher overall

102

strength in this study, which is in agreement with previous studies in the literature [171][286][292-293]. The measured average grain-size of APMT_Post-CHF was 6.96±3.27 μm, while it was 44.21±15.33 μm for C26M_Post-CHF. These results did not show significant changes in the grain-size for the post-CHF samples.
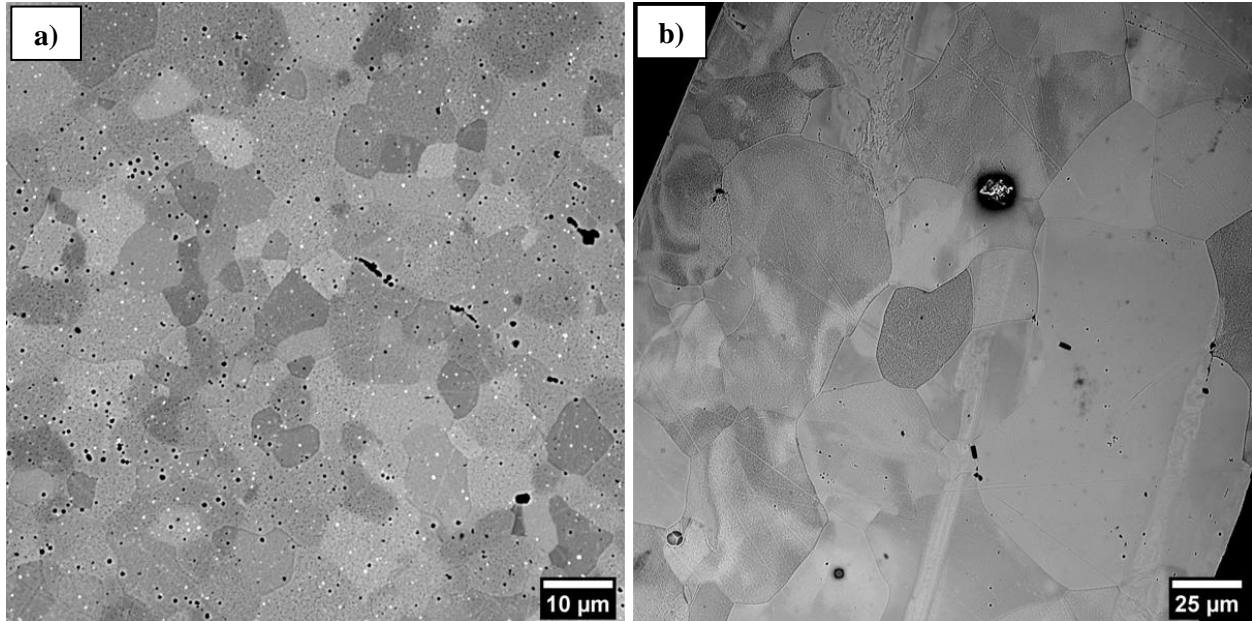
Figure 6.16 SEM micrographs of etched samples: a) APMT_Pre-CHF and b) C26M_Pre-CHF.

The implementation of FeCrAl alloys as accident tolerant fuels in light water reactors relies on their high resistance to degradation at high temperatures and their better performance than the current materials under normal operating conditions. During the flow boiling CHF experiments performed herein, the FeCrAl alloys evinced their ability to rapidly react to the temperature rise during the CHF event forming an oxide layer on the surface that prevents degradation of the cladding, which also led to an improved surface wettability and roughness. These surface properties of both FeCrAl alloys may result in the enhanced thermal-hydraulic performance of the materials.

6.3.3 Detailed microstructural evolution of APMT FeCrAl alloys after CHF with high-resolution XPS, TEM, and XRD techniques.

This section focuses on the detailed microstructural characterization of APMT FeCrAl alloy's surface as a result of CHF testing, which results in rapid temperature excursion. Ramp heating test was conducted in flow boiling facility explained in the previous section. Instrumented heater rod was fabricated from ~450 mm long APMT tube for direct heating via an applied current with a uniform power profile. The heater rod temperature was monitored using K-type thermocouples with a measuring error of less than 1 °C. The experiment was conducted using water as the working fluid at atmospheric pressure, with 76 °C of subcooling, and at a flow rate of 750 kg/m^2. The heat flux was generated by increasing the applied voltage to the heater rod while maintaining the constant inlet conditions (supercooling, mass flux, pressure). From 0 to 2000 kW/m^2 heat flux range, the heat flux was manually increased by 330 kW/m^2 per step. After increasing the heat flux at each step, there was a waiting time of 1 minute to maintain a steady-state, then the heat flux and surface temperature were measured for 1 minute. When a heat flux of 2000 kW/m^2 was reached, and the system was equilibrated, an automatic heat flux ramp was initiated. Note that at this point, the cladding tube's temperature is below 50 °C as can be seen from Fig 6.17. The heat flux was increased at each step by 1.25 kW/m^2 every 10 seconds until an abrupt increase in the heater rod's temperature. At this point, the power supply was automatically disconnected to prevent further heating of the heater rod. Fig. 6.17 shows the temperature variation over time for the APMT sample. The graph shows the cladding tube's surface temperature rises from 50 °C to 419 °C within a second and then rapidly falls once the power supply turns off. After flow boiling testing, approximately 5 mm long specimens were cut out of the tubes and named to APMT_RH (APMT ramp heated sample).
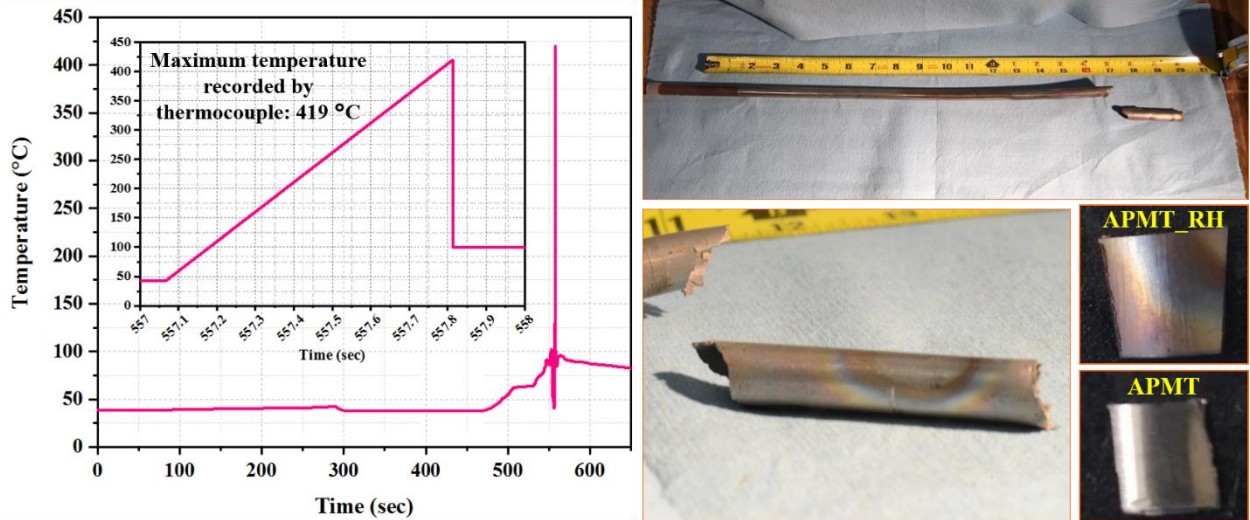
Figure 6.17 Ramp heating process under liquid subcooling of 76 °C (left) and samples after testing with small tube specimens selected for this study (right).

The microstructure and chemistry of oxide formed on the surface of APMT_RH were studied using TEM. Fig. 6.18(a) shows a TEM micrograph evidencing the formation of a thin oxide layer of ~90 nm, highlighted by red arrows. EDS point analysis was carried out for the spherical precipitates marked with A to analyze the microstructure in more detail (Fig. 6.18(a)), and chemical compositions from marked regions are shown in Table 6.5. The data shows that precipitates were rich in Fe and Mo with other alloy elements. Literature has evidenced that Mo segregates at grain boundaries when the temperature reaches 500 °C playing a role in the solution strengthening, and it hinders the recrystallization, which results in tensile properties improvements [294-295]. In Fig. 6.18(a) some features located at the oxide/metal interface are marked as B. The element identification of this region shows the increased presence of yttrium. Some studies in the literature have reported the formation of yttrium oxide precipitated at the grain boundary of alumina on FeCrAl to prevent the formation of voids in the interface, which reduces the growth rate of alumina and improves the adhesion [23][296-297]. The region marked with C mainly contains Pt and Au, deposited before lamella preparation. Fig. 6.18(b) shows X-ray EDS maps for Fe, Cr, Al, and O. The EDS map shows a thin alumina layer with some precipitates marked in the map for Fe.

EDS line analysis was carried out to investigate the elemental distribution inside the oxide layer and the neighboring metal alloy. The variations in the EDS counts of each element along lines H (covers oxide and alloy) and V (only in oxide layer) are shown in Fig. 6.18(c) and (d), respectively. The oxide layer mainly consisted of Al and O (Fig. 6.18(c)), and their steady intensity (Fig. 6.18(d)) indicates a homogeneous chemical composition over the entire cross-section with several Fe-rich precipitates region.
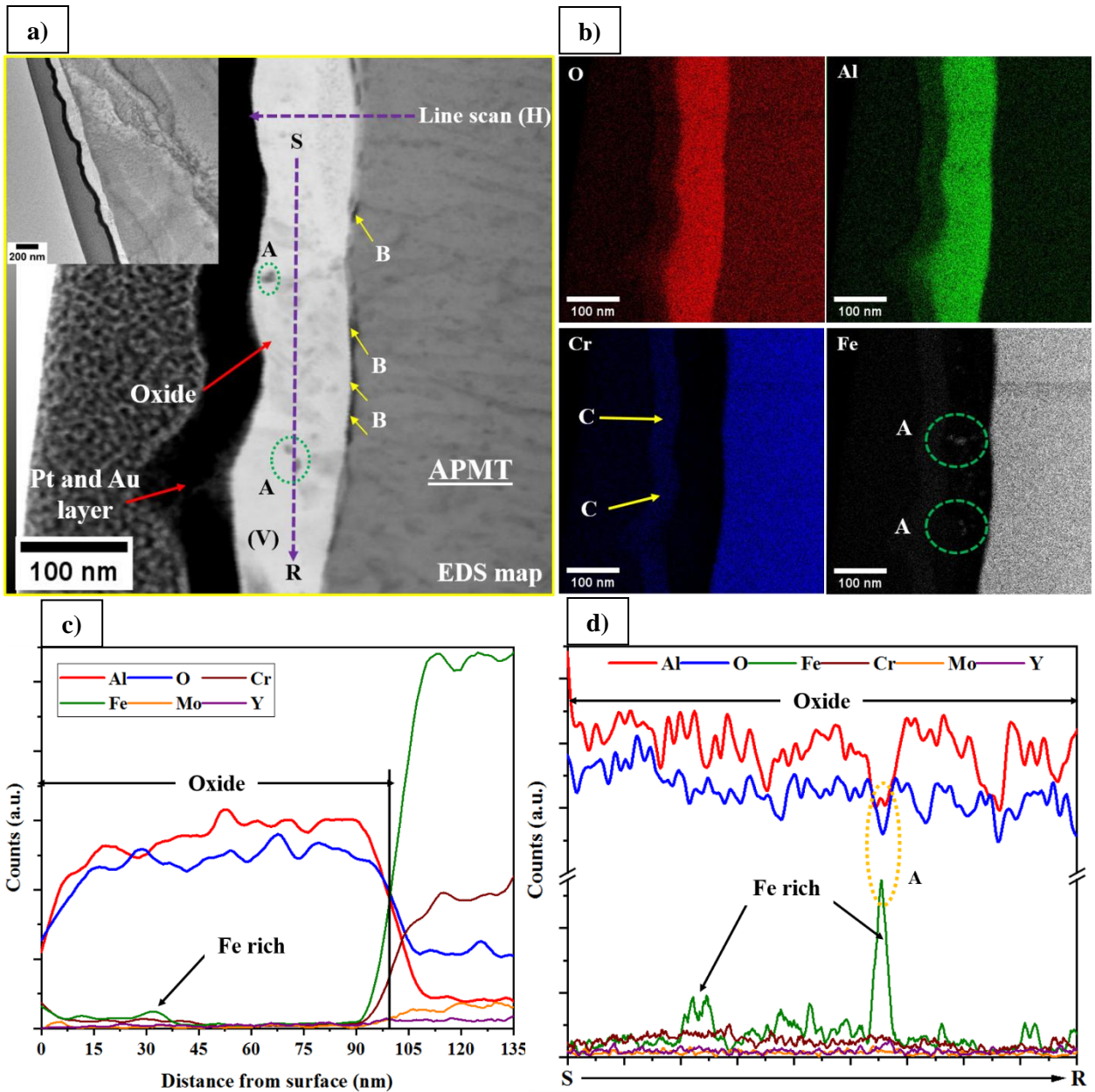
Figure 6.18 TEM observation of APMT after ramp heating: a) STEM cross sectional image of oxide formed on APMT_RH highlighting different features, b) X-ray EDS maps of the major alloy constituents and O, c) X-ray EDS line scan profile across the oxide film, and d) line scan profile along the oxide film.

Table 6.5 Chemical composition of selected points labelled as A, B, and C in Fig. 6.18(a) (as obtained from TEM-EDS).

Points	Elements (%wt)							
	Pt	Au	Fe	Cr	Al	Mo	Y	O
A	-	-	15.37	6.89	30.95	7.35	1.45	39.45
B	-	-	3.22	2.63	1.5	-	89.66	2.99
C	80.64	16.65	0.90	1.64	0.06	-	-	0.12

A comparison of the X-ray diffraction patterns of the APMT specimens before and after ramp heating are presented in Fig. 6.19. All diffraction peaks observed in the APMT sample confirm the BCC crystal structure (ICDD pdf #00-054-0387). The additional peaks observed for APMT_RH were indexed to the α-Al_2O_3 (ICDD pdf #04-015-8610). However, it was challenging to identify with certainty the nature of the other phase present in the diffraction pattern because γ-Fe_2O_3 and Fe_3O_4 showed almost the same XRD pattern owing to their similar structure [294]. High-resolution TEM were collected to obtain more detailed microstructural information on the oxide layer. The HRTEM image showed in Fig. 6.20 confirms the crystalline nature (demonstrated by the lattice fringes) of the oxide layer. The lattice spacing for the (101) planes in a rhombohedral structure of Al_2O_3 was 3.5 Å which agrees with the results obtained in XRD.
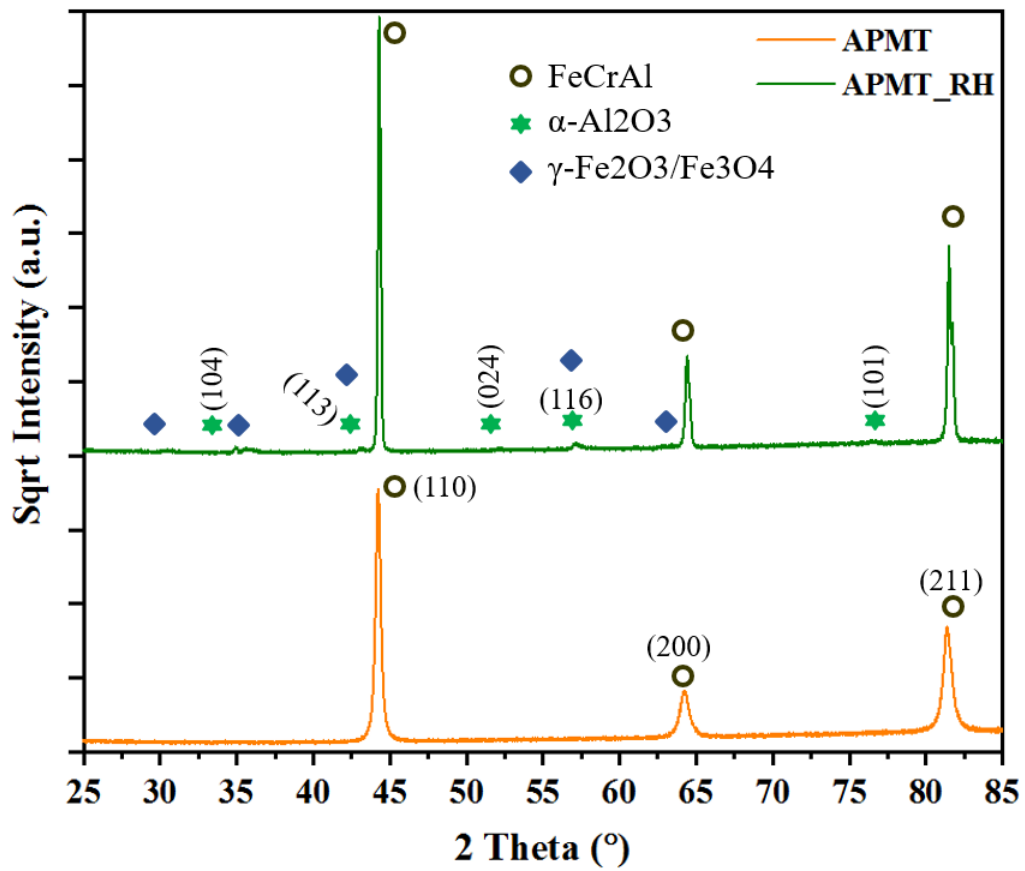
Figure 6.19 X-ray diffraction pattern of the APMT before and after ramp heating testing.
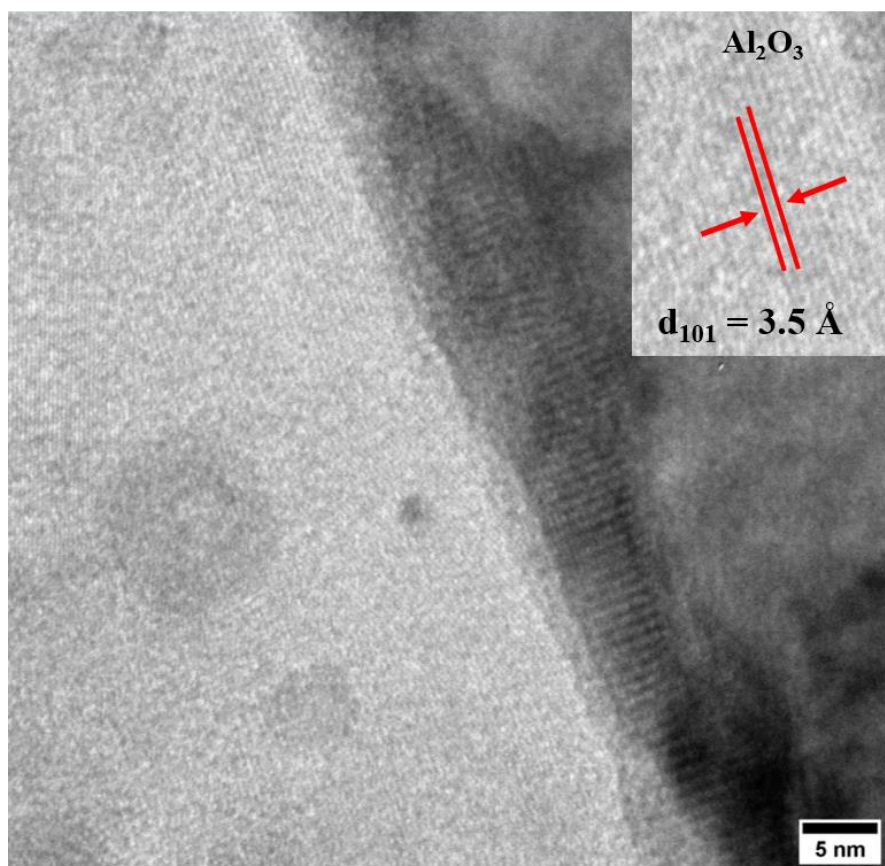
Figure 6.20 HRTEM collected from oxide region (shown in Fig. 6.18(a)) of APMT sample surface after ramp heating.

The compositional XPS depth profile was obtained from the APMT_RH sample surface (somewhere near from blue region shown in Fig. 6.17) and shown in Fig. 6.21. The compositional depth profile result indicated a thin oxide layer enriched in Al with a small amount of other elements like Fe and Cr. The higher or equal oxygen to metal ratio was evident up to about 115 min of sputtering, which is in good agreement with the thickness of the oxide layer calculated from TEM cross-sectional images in Fig. 6.18(a). A thin C-rich layer was identified in these results, which may be attributed to the physical deposition of carbonaceous compounds during sample handling/storage. To determine the oxidation state of the alloying elements, the high-resolution XPS spectra of Al2p, Fe2p, and Cr2p were collected at different depths and analyzed. Fig. 6.22-6.23 shows the deconvoluted spectra. In the analysis of all high-

110

resolution spectra, the original spectra and fitted profile are shown as black dotted lines and the thin brown line. The peak positions associated with each elements and their oxidation states are within range of binding energies reported in the literature [240-250][270-277]. The fitting of all XPS patterns in this work was treated with a multi-peak [250-252]. The results confirmed that Fe, Cr, and Al all exhibited an oxidized nature near the surface and switched to the zero valence state as the depth increased. Consistent with their stabilities, the switch from oxide to metal state occurred earlier for Fe, then Cr, and finally Al, similar trend what we observed for APMT and C26M in the previous section.
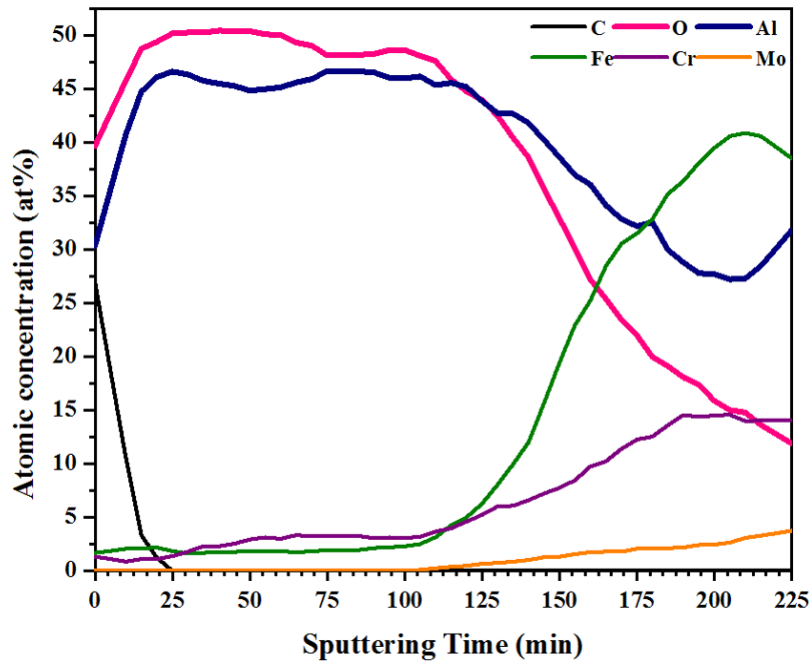
Figure 6.21 Element composition vs. depth (sputter time) profile for APMT_RH surface (sputtering for 112 etching cycle (2 min each) using Ar+ ion with 3 keV beam energy).
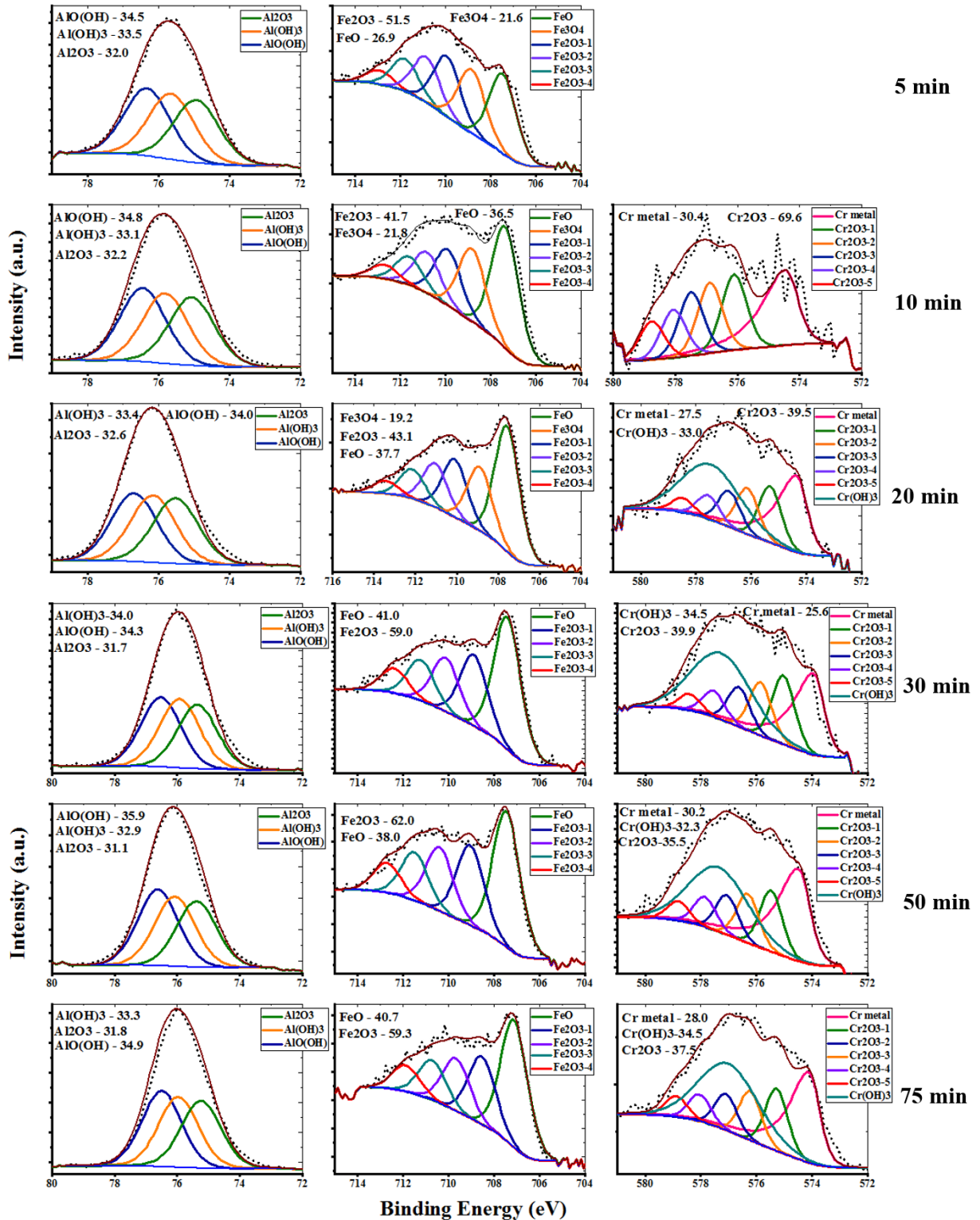
Figure 6.22 XPS high-resolution spectra for Al2p, Fe2p and Cr2p at various depths for the APMT_RH sample (each present species were calculated in %area).
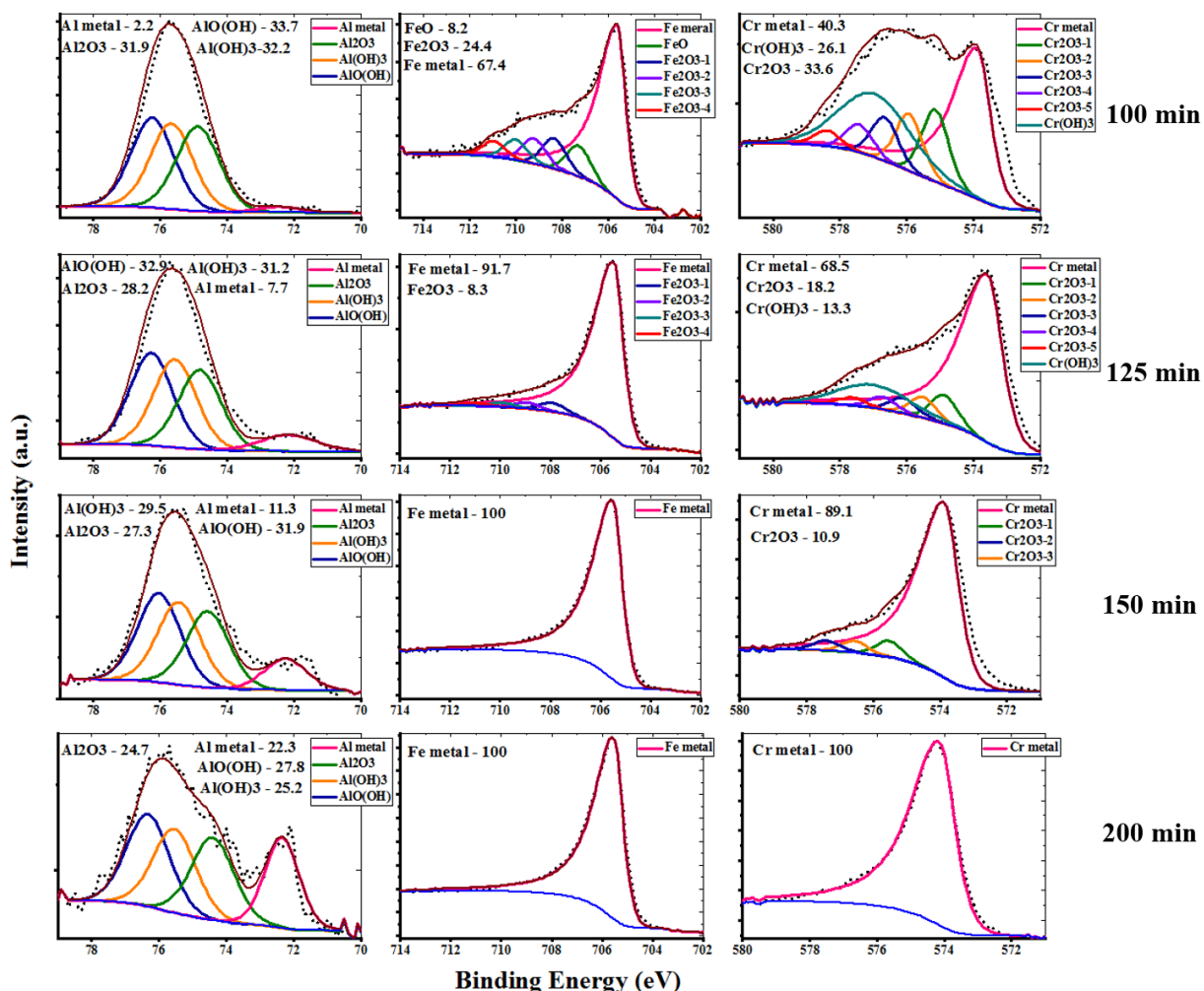
Figure 6.23 (continued 6.22) XPS high-resolution spectra for Al2p, Fe2p and Cr2p at various depths for the APMT_RH sample (each present species were calculated in %area).

Fig. 6.24 shows the graphical representation of the oxide species obtained from deconvolution of all high-resolution XPS spectra collected during depth profiling on APMT_RH in which X-axis reads sputtering times at which high-resolution spectra were collected. During ramp heating process in the flow boiling system, working fluid (DI water) would take a series of reactions on the APMT sample surface. During the first stage of sputtering (5 min in Fig. 6.24), mainly aluminum oxides and hydroxides with a noticeable amount of Fe and its corresponding oxides were obtained, with no evidence of Cr oxides. These data are consistent with phases identified in XRD analysis (Fig. 6.19) as well as TEM observations

(Fig. 6.20). In the ramp heating test, the sample was heated for a short period, which means after a thin layer of pure/mixed oxide film formed on the surface, the oxidation reactions between O^{2-} and metal elements on the surface may be ended. However, because of the existence of mixed oxide film, internal diffusion of O^{2-} was enough to produce more Al_2O_3, $Al(OH)_3$, $AlO(OH)$, FeO, Fe_2O_3, Fe_3O_4 and Cr_2O_3. In the sputtering time between 5 to 10 min, some of the Fe_2O_3 in the internal layer was transformed into FeO, and Cr_2O_3 sub-passive film gradually formed in the interface (scale/matrix). The diffusion speed of O^{2-} is lower in Cr_2O_3 than that in Fe oxides, which reduces the concentration of O^{2-} in the matrix [298]. Thus oxidation rate of alloy stopped accelerating and slowed down. However, at depths given by the sputtering times from 20 min to 150 min, O^{2-} was more likely to react with Al to form oxides and hydroxides. The detailed explanation of the reaction of Al with water was explained by phase stability diagrams in the previous section. For the APMT_RH sample, at the highest sputtering time used in this experiment, when the concentration of O^{2-} at the interface (mixed oxide film/matrix) was too low to promote oxide formation, it led to negligible amounts of Al and Cr oxides. At this point, the area percentage of all elements and their species at different valence states are almost similar to the results of deconvoluted high-resolution spectra of pre-CHF FeCrAl samples shown in the previous section.

Figure 6.24 Graphical representation of all high-resolution XPS spectra (Al2p, Fe2p and Cr2p) collected at different depth for APMT_RH sample.

It is well known that FeCrAl alloys tend to form protective α-alumina layers on their surface at high temperatures [168][299], resulting in the significantly reduced oxidation rate of FeCrAl alloys in high-temperature environments. During the ramp heating experiment performed herein, the APMT evinced the ability to rapidly react to the temperature rise during the CHF event forming an oxide layer on the surface. These preliminary results indicate that oxidized APMT may withstand accident conditions without leading to a boiling crisis.

6.4 Summary

The FeCrAl alloys APMT, C26M, and Cr-coated Zircaloy-4 using PVD and cold spray were tested in a flow boiling testing facility at atmospheric pressure. The surface characteristics, mechanical properties, and microstructural features of all materials were studied before and after CHF testing through XPS, contact profilometry, AFM, contact angle goniometry, microindentation and ring compression, FIB-SEM, and XRD. Surface characterization of post-CHF Cr-coated test samples showed a small increment in surface roughness while a noticeable increase in the surface wettability was reported for substrate Zircaloy-4 and Cold Spray Cr-coated samples because of oxide formation on the surface and decreased carbon content. After the flow boiling test, the formation of a thin oxide layer was evidenced in the cross-sectional examination of both FeCrAl alloys. Analysis of the material's topography showed higher roughness parameters, which may result from the surface oxide formation during CHF testing. The detailed early-stage oxidation of the alloys was studied using XPS depth profiling with the high-resolution spectra of Al2p, Fe2p and Cr2p elements. The results revealed a thin layer of aluminum oxides and hydroxides mixed, with a small fraction of other elements and their oxides for APMT_Post-CHF. A pure Al_2O_3/ $Al(OH)_3$/ $AlO(OH)$ was detected for the C26M_Post-CHF sample. Similarly, the increase in the materials' wettability has been attributed to the hydrophilic behavior of the aluminum species formed in the materials' surface. Hardness was slightly increased for both FeCrAl samples after CHF testing. However, compared to C26M, the APMT sample showed almost 30% higher hardness before and 15% higher after flow boiling testing. The increase of peak load and yield strength was recorded for both types of FeCrAl alloys due to CHF testing. Higher overall mechanical properties of APMT over C26M may be attributed to their different grain size. XRD patterns revealed the sharpening of the peaks after flow boiling testing, indicating lower dislocation density. Additionally, microstructure after ramp heating test of APMT confirmed oxide layer of α-Al2O3 corundum with some spherical precipitates of Cr, enriched Fe, and Mo. Furthermore, the oxide/alloy interface was found to be rich in Y.

Chapter 7: Comparison of the experimental results with preliminary results obtained from

RELAP5-3D

7.1 Introduction

The current research in ATF cladding materials has mostly focused on the ability to resist steam oxidation and retain mechanical strength and structural integrity under normal and accident scenarios. However, it is essential to investigate the materials' thermal-hydraulic behavior by estimating CHF and HTC phenomena by conducting experiments and simulations to determine safety margins in LWR operations. The literature has reported a tremendous amount of pool and flow boiling experimental work performed for different ATF materials [295]. However, there is limited work that has been done on the simulation side. The prediction of CHF remains challenging to conceptualize and model because most of the experimental thermal-hydraulic research focused on obtaining data for specific conditions and geometries. Additionally, the large amount of data that has been collected under corporate supervision remains proprietary. Hence, most CHF predictions rely on comparing tabulated values or applying correlations [91]. However, when compared with experimental data, these correlations have demonstrated limited success due to the complexity of the phenomenon. Furthermore, the effect of many variables such as mass flux, local quality, pressure, flow geometry, axial heat flux profile, wettability, and surface roughness in CHF enhancement is evidenced in the literature [90]. Thus, a single experiment may or may not apply to other situations. The use of data and correlations from uniform heat profile experiments and applying a correction factor to account for the non-uniformity has become common practice in the nuclear industry, leading to a misunderstanding of the CHF phenomenon. Because for example, in channels with uniform heat flux, CHF always occurs at the end, where the quality is highest; however, CHF events rarely happen at the exit when non-uniform heat flux profiles are applied. Since most correlations are constructed from the experiments performed using a single heated tube during application in the irregular geometry of the reactor core, these values must then be adjusted for the heated rod bundle geometry. Thus it is necessary to use simulation tools to understand thermal hydraulic response of ATF to design basis

117

accident condition, such as loos of coolant accident (LOCA). In this work, we performed an early

thermal-hydraulic evolution by comparing high-resolution experimental data of traditional Zircaloy-4

obtained from the University of Wisconsin and results from computational tool, RELAP5-3D, modeled

based on those experiments.

7.2 CHF correlations

There is a number of CHF correlations exist in the literature. These correlations are useful prediction

methods for assessing new flow systems. Some of the most common methods for CHF prediction are

discussed here. The Babcock & Wilcox CHF correlation [300] has been derived based on 601 data points

obtained from seven separate tests, including partial and full-length rod bundles with both uniform and

non-uniform axial flux shapes. This correlation is only applicable to 17×17 fuel geometry. Another

correlation developed from uniformly heated tube experimental data is the Biasi correlation [301]. This

correlation does not include any modifications for rod bundle geometry or non-uniform power profile but

the nuclear industry uses it as a consistent reference point. To predict CHF in PWRs the Westinghouse

Electric Corporation developed the W-3 correlation [302]. Although this correlation has been developed

for predicting the DNB (departure from nucleate boiling) using data for an axially uniform heat flux

distribution, the correlation incorporates the so-called Tong F-factor to correct for non-uniform heat flux

distributions. Since this correlation is developed to predict the local DNB heat flux and DNB location, it

is limited to high mass flux and low local quality conditions, which means it is not suited for dryout

phenomena. Similarly, the EPRI correlation was developed based on rod bundle CHF data which

intrinsically accounts for rod bundle geometry effects. However, the applicable range for this correlation

is limited to less than 17 MPa. There are several other correlations in literature developed using pool

boiling experimental data cannot be for nuclear application [99][136][303-306]. More recently,

Groeneveld et. al. [96] has gathered worldwide data and organized it into a table format known as look-up

table (LUT), which was last updated in 2006. The literature has shown good agreement between

experimental CHF value with predicted value using LUT [259][307]. Since the LUT was constructed

118

from many experimental data sets, it remains valid across a wide range of operating conditions with high

error in certain regions where a limited number of data samples are used to compose the table. The LUT

has multiplicative factors, K-factors, similar to the previously described correlations to account for

differences in configuration. Table 7.1 summarizes the applicable ranges of pressure, mass flux, and

quality for the discussed correlations in this section.

Table 7.1 Different CHF correlation with their validated ranges.

CHF Correlations	Validated Ranges		
	Mass Flux (kg/m²s)	Pressure (MPa)	Local quality
Babcock & Wilcox	1274 – 5425	12 – 17	-0.03 – 0.22
Biasi	100 – 6000	0.27 – 14.2	0 – 1
W3	1360 – 6780	6.9 – 15.86	-0.15 – 0.15
EPRI	270 – 5560	1.38 – 16.9	-0.25 – 0.75
LUT	0 – 8000	0.1 – 21	-0.5 – 1

7.3 Results and discussion

7.3.1 Experimental results

The CHF tests used to compare RELAP5-3D model were conducted at the University of Wisconsin –

Madison Thermal Hydraulics Lab flow boiling facility. Detailed specifications for the flow boiling facility

are described in Chapter 6. Table 7.2 shows the parameters used for the flow boiling test. Instrumented

heater rods were fabricated from Zircaloy-4 cladding material, designed for direct heating via an applied

current with a uniform power profile. The inner wall temperature of the cladding tube was measured

using optical fiber inserted into the heater rod. Using the temperature profile measured with the optical

fiber and the measured heat flux, it was possible to estimate the heater rod surface temperature via a 1D

radial conduction model. The uncertainty of temperature measurement was found to be ±1.9 ºC. Using

optical fibers, the temperature was measured every 2.5 mm in the axial direction of cladding tubes. For a

119

457 mm length of tube, total 142 measurements were recorded along the length of the rod. CHF was determined when an abrupt increase of the heater rod's temperature occurred. Specifically, the temperature threshold for CHF was set to 25-30 ℃ higher than the steady-state operating temperature of the heater rod. The CHF trip occurred in the temperature range of 190-220 ℃ for the heater rod. When CHF is detected, the power supply was automatically shut down to prevent further heating of the heater rod and avoid load failure. The surface temperature profile measured for Zircaloy-4 rod during the automatic heat flux ramp phase is shown in Fig. 7.1. Results show a nearly uniform temperature profile along the flow direction; however, bubbles accumulate near the outlet region as the heat flux increases and peak temperature occurs. This location was confirmed to have occurred near the outlet, between 70-80% of the heated length by visual observation form temperature profile as well as discoloration on the surface of the rod following the experiment.

Table 7.2 Parameters of the flow boiling heat transfer experiment.

Parameter	Value
Hydraulic diameter	10.5 mm
Cladding tube OD	9.5 mm
Cladding wall thickness	0.51 mm
Heated length	457.2 mm
Cladding material	Zircaloy-4
Nominal heat flux	0 - 3 MW/m^2
Heat flux profile	Uniform
Flow channel	Annular
Inlet temperature	24 ℃
Inlet pressure	115 kPa
Nominal mass flux	750 kg/m^{2}s
Working fluid	Water
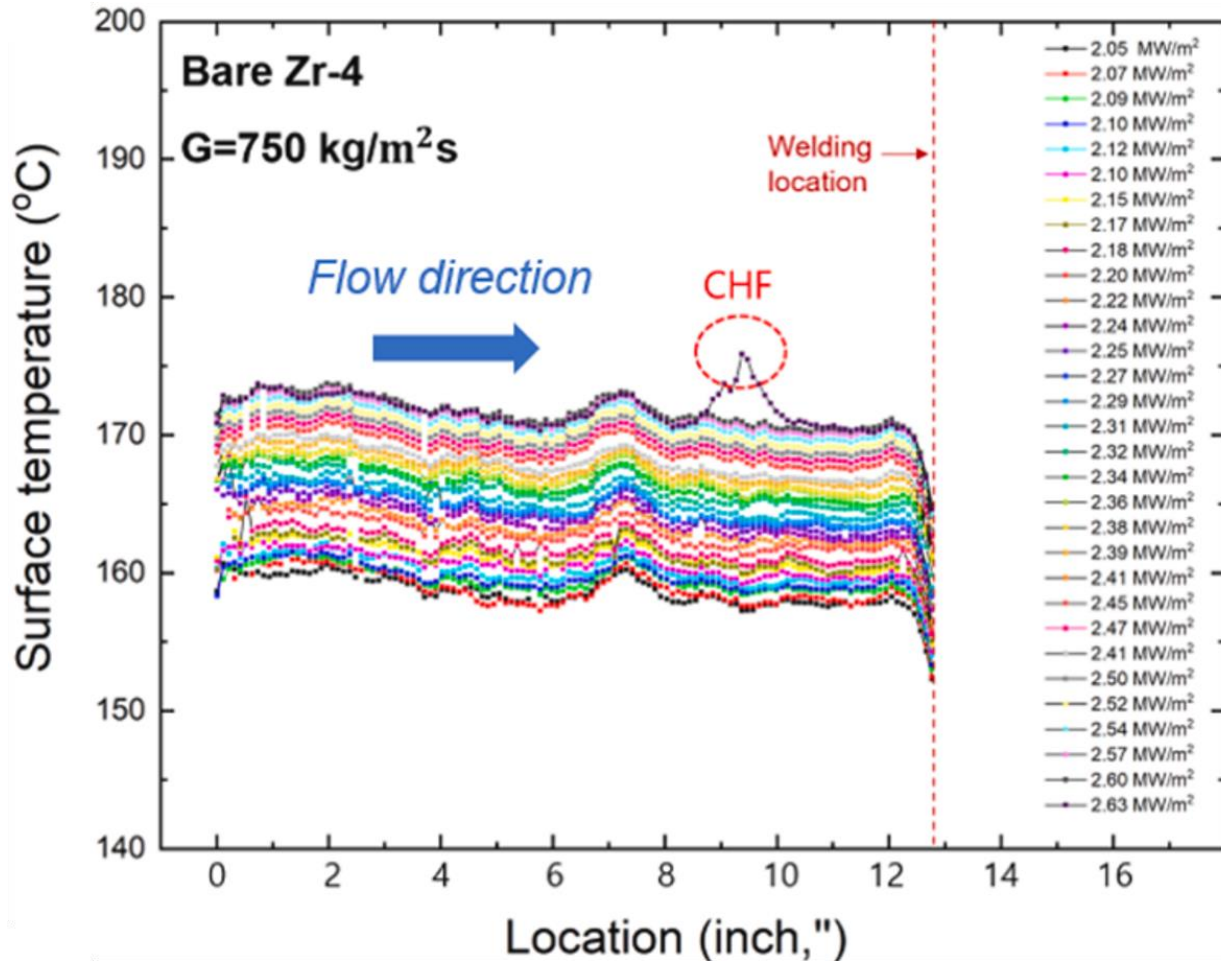
Figure 7.1 Surface temperature profile for Zircaloy-4 rod recorded during flow boiling experiment [259].

7.3.2 RELAP5-3D model description

Fig. 7.2 shows the nodalization diagram of the RELAP5 model [308-309], created in Computation Applied Reactor Physics Laboratory (CARPL) by PhD student Tao Liu. The tube dimensions listed in Table 7.2 were replicated in the models. In the RELAP5-3D, the heat transfer packages within the codes always assume fully developed flow hence, only the heated length of the test section was modeled. In this model a time-dependent inlet volume, labeled with 100 is connected to a vertical pipe using a time-dependent junction, which is then connected to an outlet, labeled with 140 using a single junction. A heat structure is attached to the pipe to provide the power transient. The heat structure had 50 axial nodes. A

121

minimum timestep of 1×10^{-8} s was used. RELAP automatically ensures that the maximum timestep used is below the Courant limit. The boundary conditions, pressure, mass flux, and temperature of the coolant used in this model are listed in Table 7.2. The Groeneveld look-up table was used as the CHF prediction method.
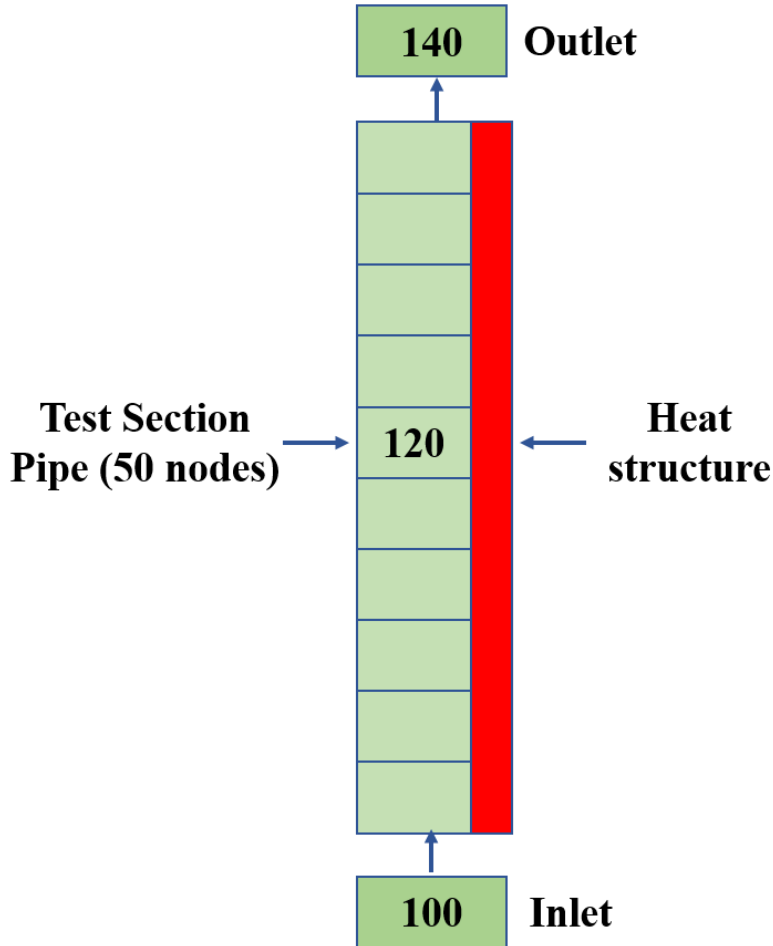
Figure 7.2 Nodalization diagram of RELAP5-3D model.

The thermal conductivity and volumetric specific heat of Zircaloy-4 as a function temperature were used as input are given as following:

$$k = 8.8527 + 7.0820 \times 10^{-3}T + 2.5329 \times 10^{-6}T^2 + 2.9918 \times 10^3 T^{-1} \ W/mK \qquad (7.1)$$

$$c_p = 17.2319 \times 10^5 + 624.4559T - 49.8819 \times 10^8 T^{-2} \; J/m^3K \qquad (7.2)$$

Where the temperature T is in K. Fig. 7.3 shows thermal conductivity and volumetric specific heat with temperature.
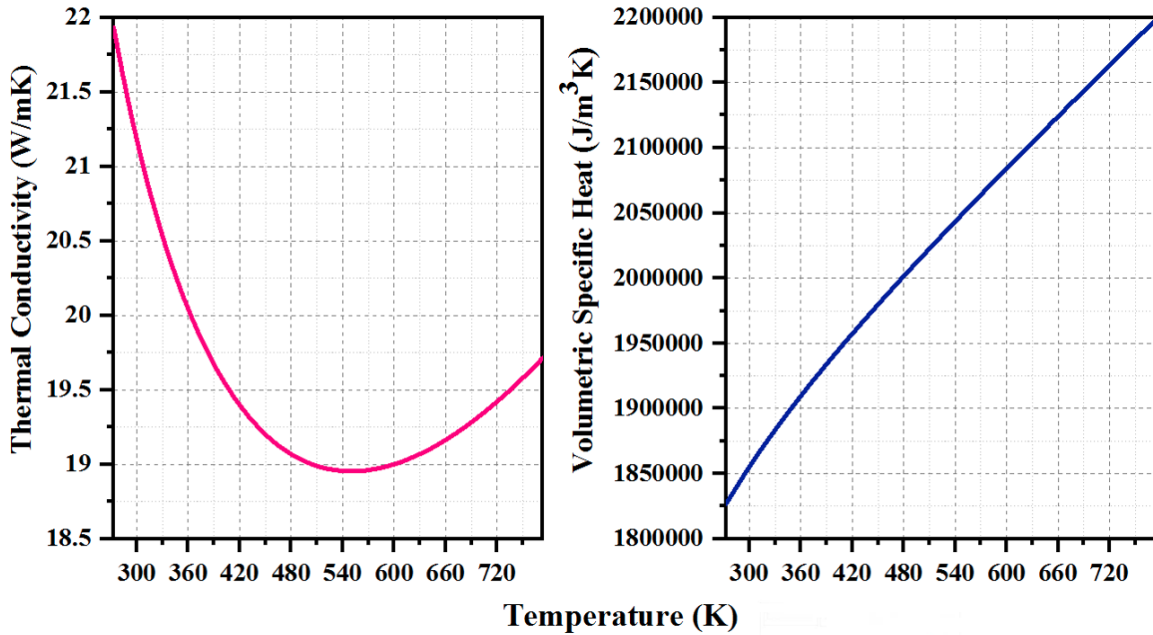
Figure 7.3 Thermal conductivity (left) and Volumetric specific heat (right) of Zircaloy-4 vs temperature [310].

7.3.3 Code-to-experiment comparisons of outer surface temperature

Using material properties and flow boiling experimental conditions described in previous sections, the surface temperature was estimated for Zircaloy-4 sample in RELAP5-3D. The surface temperature was calculated for three roughness finish, as-received (0.399 µm), 600-grit polished (0.496 µm) and 240 grit polished (0.776 µm) samples. The surface temperature was almost similar for all surface roughness, and Fig. 7.4 shows the temperature profile for the as-received Zircaloy-4 sample. Here, the temperature was measured for two different heat-flux; experimental CHF value, 2.63 MW/m^2 and CHF value predicted by Engineering Equation Solver (EES), 3.26 MW/m^2. From the temperature profile, it was clear that surface temperature estimated by RELAP5-3D for heat-flux predicted using EES was almost similar to the

123

experimental temperature profile obtained for heat-flux, 2.63 in Fig. 7.1. Further study will focus on estimating CHF value for all samples with different roughnesses to study their effect on CHF.
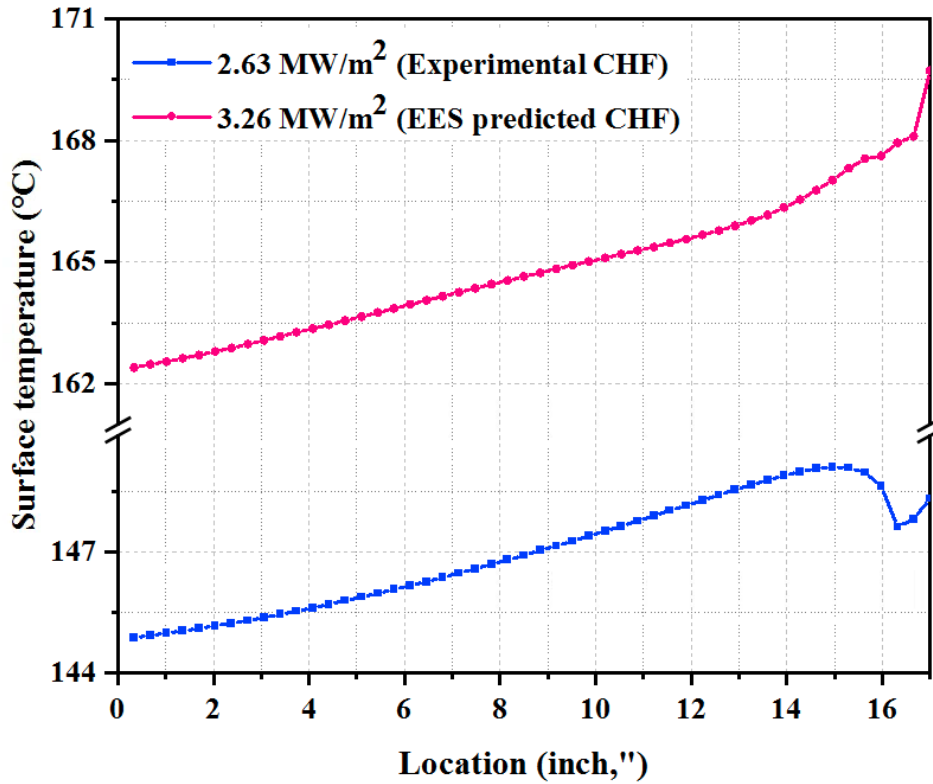
Figure 7.4 Surface temperature of Zircaloy-4 from RELAP5-3D.

7.4 Future work

Future work is underway for the development of a transient heat flux model in RELAP5-3D. The model then would be tested for all ATF materials including, Cr-coated Zircaloy-4 produced by PVD and Cold Spray, both FeCrAl alloys, APMT (with different roughness) and C26M to predict CHF values using inbuilt LUT tables and compared them with thermal-hydraulic data acquired from experiments conducted at University of Wisconsin. Furthermore, effect of surface characteristics such as, roughness and wettability in enhancement of CHF and HTC will be studied using existing correlations in the

literature. These existing models characterizing the cladding surface effects on CHF may be modified to meet the requirements of ATF candidates.

More importantly, sensitivity analysis will be performed to investigate the impact of HTC, and material thermal properties on CHF and peak cladding temperature. RELAP5-3D heat structure input allows for multipliers on heat transfer coefficients and CHF predicted by their respective correlations. These multiplier values will be chosen in several ways, for instance, the experimental nucleate heat transfer coefficient obtained from University of Wisconsin was 0.25 times higher for Cr-coated Zircaloy-4 (using Cold Spray) compared to Zircaloy-4 [259]; hence, the nucleate boiling heat transfer coefficient multiplier will be varied using RAVEN from 0.1 to 0.5 to determine if this effect could have an impact on CHF. Furthermore, the variation of the thermal properties of ATF including volumetric heat capacity and thermal conductivity will be studied, within the uncertainty ranges of those properties. The sensitivity of CHF to thermal effusivity and thermal diffusivity will be calculated. To replicate the enhancement in CHF caused by the transient heating process and to ensure that the experimental CHF was reached, the CHF multiplier will be varied. A large number of combinations will be explored to understand the sensitivities.

Chapter 8: Outlook, Conclusions, and Future work

8.1 Outlook

The overall goal of this work was to investigate different ATF cladding materials and their surfaces by measuring surface properties, such as surface roughness, morphology, and wetting characteristics, as numerous studies have implied the impact of such properties on the boiling performance. Furthermore, this work investigated the changes of the materials' surface properties post-CHF testing and environmental surface aging. This work revolved around the hypothesis that the wettability and topography of ATF cladding surfaces are altered when exposed to normal humid environments and to flow boiling CHF. This work was carried out by investigating the materials' surface chemistry changes as a result of environmental testing conditions (the type of coolant, temperature, pressure). The wetting characteristics results show that the Cr coated (both PVD and Cold Spray coatings) surfaces have higher wettability than the original Zircaloy-4 surfaces, which may improve the thermal-hydraulic performance of the cladding surface, tolerating higher heat fluxes before departure boiling is evidenced. There is, however, hydrophobic recovery of the surface wettability of Cr-coating during aging in humid air that could result in decreased thermal-hydraulic performance, especially when there is a time delay between testing stages. The Cold Spray coatings with higher roughness may have a slight advantage against PVD from the point of view of CHF, coating adhesion, and wettability; however, higher roughness sometimes increases corrosion susceptibility. The detailed comparison for two types of coating with their different surface finish provided in this study can be used as a quality assessment tool for selecting ATF candidates. The ramp heating of two FeCrAl alloys, APMT and C26M, can help to understand their evolution at the early stage of high-temperature excursions. The in-depth surface chemistry analysis evidenced the formation of various oxides that elucidate the rapid response of FeCrAl alloys toward accident scenarios. The results provided in this dissertation provide a foundation for future testing of ATF cladding materials and assessing the thermal performance in full-scale systems taking into account their surface characteristics.

126

8.2 Conclusions

Detailed surface characterization was conducted for ATF cladding candidates, such as APMT, C26M, Zircaloy-2, substrate Zircaloy-4 and Cr-coated Zircaloy-4 produced by two different coating techniques, PVD and Cold Spray. The surface properties of all samples were assessed in terms of chemical composition, roughness, topography, and wettability. For the Cr-coated samples, the coating quality was tested by different mechanical methods, such as nanoindentation, nano-scratch test, and ring compression tests. For coated samples, the ring compression test confirmed the higher mechanical strength of the tubes after the deposition of the coatings. Higher hardness was recorded for both types of coatings compared to that of the substrate Zircaloy-4, which has a hardness value of approximately 3.05 GPa. The adhesion property, assessed by the nano-scratch test, indicated that the coatings adhered well to the Zircaloy-4 substrate, and results showed increasing adhesion with increasing initial substrate surface roughness. Roughness measured from as-received samples were logged higher value for both FeCrAl alloys (APMT and C26M), which were almost double compared to the Zircaloy-2 specimen. Similarly, overall roughness for coated samples was higher compared to their substrates. Surface topography and wetting characteristic were studied after surface modification for all ATF candidates. The contact angles were measured for each surface to evaluate their surface wettability. According to the study for the as-received materials, Zircaloy-2 showed a lower contact angle compared to the FeCrAl alloys (APMT and C26M) and substrate Zircaloy-4. A significant enhancement in wettability was logged after the deposition of chromium coating by PVD and CS, which may improve the thermal-hydraulic performance of the cladding surface, tolerating higher heat fluxes before departure boiling is evidenced. However, ambient aging of the plasma-treated chromium surfaces in air resulted in a significant change in the oxidation states of Cr(0) to Cr(III) oxides and hydroxides and absorption of carbonaceous species, which in turn decreased the wetting characteristics. This hydrophobic recovery of the surface wettability of Cr-coating during aging in humid air could result in decreased thermal-hydraulic performance, especially when there is a time delay between testing stages. The surface characteristics, mechanical properties, and microstructural features of FeCrAl alloys APMT, C26M and Cr-coated Zircaloy-4 using PVD and Cold

Spray were tested after exposing them in flow boiling testing facility at atmospheric pressure. Surface characterization of post-CHF Cr-coated test samples showed a small increment in surface roughness while a noticeable increase in the surface wettability was reported for substrate Zircaloy-4 and Cold Spray Cr-coated samples because of oxide formation on the surface and decreased carbon content. The cross-sectional examination of both post-CHF FeCrAl alloys evidenced the formation of a thin oxide layer. Analysis of the material's topography showed higher roughness parameters, which may result from the surface oxide formation during CHF testing. The detailed early-stage oxidation of the alloys was studied using XPS depth profiling with the high-resolution spectra of Al2p, Fe2p and Cr2p elements. The results revealed a thin layer of aluminum oxides and hydroxides mixed, with a small fraction of other elements and their oxides for APMT_Post-CHF. A pure Al_2O_3/ $Al(OH)_3$/ $AlO(OH)$ was detected for the C26M_Post-CHF sample. Similarly, the increase in the materials' wettability has been attributed to the hydrophilic behavior of the aluminum species formed in the materials' surface. Hardness was slightly increased for both FeCrAl samples after CHF testing. However, compared to C26M, the APMT sample showed almost 30% higher hardness before and 15% higher after flow boiling testing. The increase of peak load and yield strength was recorded for both types of FeCrAl alloys due to CHF testing. Higher overall mechanical properties of APMT over C26M may be attributed to their different grain size. XRD patterns revealed the sharpening of the peaks after flow boiling testing, indicating lower dislocation density. Additionally, microstructure after ramp heating test of APMT confirmed oxide layer of α-Al2O3 corundum with some spherical precipitates of Cr, enriched Fe and Mo. However, oxide/alloy interface was rich in Y.

8.3 Future work

Future studies will explore the mechanical and microstructure properties of both PVD and Cold Spray Cr-coated Zircaloy-4 after CHF testing. The surface chemistry of these samples will be studied by conducting depth profiling and high-resolution XPS analysis. Thermo-Gravimetric-Analysis (TGA) tests will be performed for selected ATF materials to study high-temperature behavior in steam at typical

128

DBA-LOCA (design basis accident (DBA), loss of coolant accident (LOCA)) temperature range. Mass gain behavior for ATF material will be compared with standard Zircaloy claddings. In addition, the thermal-hydraulic experimental data for ATF candidates, Cr-coated Zircaloy-4 produced by PVD and Cold Spray, both FeCrAl alloys, APMT (with different roughness) and C26M taken at atmospheric pressure and high-pressure test facilities at University of Wisconsin will be used together with the materials characterization data to explain how the surface parameters affect the CHF using existing correlations available in the literature. These models characterizing the cladding surface effects will be implemented in industry code RELAP5-3D and may be modified to meet the requirements of ATF candidates. The predicted CHF values compared with experimental data. Furthermore, to investigate the impact of HTC, surface properties, and materials thermal properties on CHF and peak cladding temperature, sensitivity and uncertainty analysis will be performed.

Chapter 9: References

[1] I.A.E. Agency, The Fukushima Daiichi Accident Report by the Director General, Dir. Gen. (2015) 1–222. https://doi.org/10.1037/a0018137.

[2] F. Goldner, Development strategy for advanced LWR fuels with enhanced accident tolerance, Present. to Enhanc. Accid. Toler. LWR Fuels Natl. Metrics Work. Oct. (2012) l5.

[3] Y.-H. Koo, J.-H. Yang, J.-Y. Park, K.-S. Kim, H.-G. Kim, D.-J. Kim, Y.-I. Jung, K.-W. Song, KAERI's Development of LWR Accident-Tolerant Fuel, Nucl. Technol. 186 (2014) 295–304. https://doi.org/10.13182/nt13-89.

[4] F. Goldner, Overview of the accident-tolerant fuel development, (2013) 14. http://www.iaea.org/inis/collection/NCLCollectionStore/_Public/47/013/47013906.pdf.

[5] S.J. Zinkle, K.A. Terrani, J.C. Gehin, L.J. Ott, L.L. Snead, Accident tolerant fuels for LWRs: A perspective, J. Nucl. Mater. 448 (2014) 374–379. https://doi.org/10.1016/j.jnucmat.2013.12.005.

[6] Top Fuel 2015, Reactor Fuel Performance, in: Top Fuel 2015 - React. Fuel Perform., 2015: p. 630. https://www.euronuclear.org/events/topfuel/topfuel2015/transactions/topfuel2015-transactions-oral-1.pdf.

[7] R.B. Rebak, Accident Tolerant Materials for Light Water Reactor Fuels, Elsevier, 2020. https://books.google.com/books?id=hSzJDwAAQBAJ.

[8] K.A. Terrani, Accident tolerant fuel cladding development: Promise, status, and challenges, J. Nucl. Mater. 501 (2018) 13–30. https://doi.org/10.1016/j.jnucmat.2017.12.043.

[9] J. Carmack, F. Goldner, B.S. Shannon M, L.L. Snead, Overview of the U.S. DOE accident tolerant fuel development program, LWR Fuel Perform. Meet. Top Fuel 2013. 2 (2013) 734–739.

[10] B. Cheng, P. Chou, Y.-J. Kim, Evaluations of Mo-alloy for light water reactor fuel cladding to enhance accident tolerance, EPJ Nucl. Sci. Technol. 2 (2016) 5. https://doi.org/10.1051/epjn/e2015-50060-7.

[11] I. Idarraga-Trujillo, M. Le Flem, J.C. Brachet, M. Le Saux, D. Hamon, S. Muller, V.

Vandenberghe, M. Tupin, E. Papin, E. Monsifrot, A. Billard, F. Schuster, Assessment at CEA of coated nuclear fuel cladding for LWRS with increased margins in loca and beyond loca conditions, LWR Fuel Perform. Meet. Top Fuel 2013. 2 (2013) 860–867.

[12]   H.G. Kim, I.H. Kim, J.Y. Park, Y.H. Koo, Application of Coating Technology on Zirconium-Based Alloy to Decrease High-Temperature Oxidation, Zircon. Nucl. Ind. 17th Vol. (2014) 346–369. https://doi.org/10.1520/stp154320120161.

[13]   B.A. Pint, K.A. Terrani, R.B. Rebak, Steam oxidation behavior of fecral cladding, Miner. Met. Mater. Ser. (2019) 1451–1460. https://doi.org/10.1007/978-3-030-04639-2_96.

[14]   K.A. Terrani, S.J. Zinkle, L.L. Snead, Advanced oxidation-resistant iron-based alloys for LWR fuel cladding, J. Nucl. Mater. 448 (2014) 420–435. https://doi.org/10.1016/j.jnucmat.2013.06.041.

[15]   J.D. Stempien, D.M. Carpenter, G. Kohse, M.S. Kazimi, Characteristics of composite silicon carbide fuel cladding after irradiation under simulated PWR conditions, Nucl. Technol. 183 (2013) 13–29. https://doi.org/10.13182/NT12-86.

[16]   H.G. Kim, I.H. Kim, Y.I. Jung, D.J. Park, J.H. Yang, Y.H. Koo, Development of Surface Modified Zr Cladding by Coating Technology for ATF, Top Fuel 2016. (2016) 1157–1163.

[17]   R. Hui, W. Cook, C. Sun, Y. Xie, P. Yao, J. Miles, R. Olive, J. Li, W. Zheng, L. Zhang, Deposition, characterization and performance evaluation of ceramic coatings on metallic substrates for supercritical water-cooled reactors, Surf. Coatings Technol. 205 (2011) 3512–3519. https://doi.org/10.1016/j.surfcoat.2010.12.017.

[18]   Z. Yao, J. Stiglich, T.S. Sudarshan, Molybdenum silicide based materials and their properties, J. Mater. Eng. Perform. 8 (1999) 291–304. https://doi.org/10.1361/105994999770346837.

[19]   Y. Ren, S. Zou, M. Lei, W. Xiao, X. Zhou, D. Tang, H. Deng, C. Xiao, Y. Chen, Effect of roughness of substrate and sputtering power on the properties of TiN coatings deposited by magnetron sputtering for ATF, J. Nucl. Mater. 509 (2018) 542–549. https://doi.org/10.1016/j.jnucmat.2018.07.011.

[20]   V.N. Voyevodin, A.S. Kuprin, E.N. Reshetnyak, V.D. Ovcharenko, R.L. Vasilenko, V.V. Bryk,

131

V.A. Belous, P.N. V'yugov, G.N. Tolmachova, Vacuum-arc chromium-based coatings for protection of zirconium alloys from the high-temperature oxidation in air, J. Nucl. Mater. 465 (2015) 400–406. https://doi.org/10.1016/j.jnucmat.2015.06.016.

[21]   A.T. Nelson, E.S. Sooby, Y.J. Kim, B. Cheng, S.A. Maloy, High temperature oxidation of molybdenum in water vapor environments, J. Nucl. Mater. 448 (2014) 441–447. https://doi.org/10.1016/j.jnucmat.2013.10.043.

[22]   R.B. Rebak, Iron-chrome-aluminum alloy cladding for increasing safety in nuclear power plants, 34 (2017). https://doi.org/10.1051/epjn/2017029.

[23]   Y. Yamamoto, B.A. Pint, K.A. Terrani, K.G. Field, Y. Yang, L.L. Snead, Development and property evaluation of nuclear grade wrought FeCrAl fuel cladding for light water reactors, J. Nucl. Mater. 467 (2015) 703–716. https://doi.org/10.1016/j.jnucmat.2015.10.019.

[24]   B.A. Pint, K.A. Terrani, Y. Yamamoto, L.L. Snead, Material Selection for Accident Tolerant Fuel Cladding, Metall. Mater. Trans. E. 2 (2015) 190–196. https://doi.org/10.1007/s40553-015-0056-7.

[25]   K. Hironaka, T. Nozawa, T. Hinoki, N. Igawa, Y. Katoh, L.L. Snead, A. Kohyama, High-temperature tensile strength of near-stoichiometric SiC/SiC composites, J. Nucl. Mater. 307–311 (2002) 1093–1097. https://doi.org/10.1016/S0022-3115(02)01049-8.

[26]   C.P. Deck, G.M. Jacobsen, J. Sheeder, O. Gutierrez, J. Zhang, J. Stone, H.E. Khalifa, C.A. Back, Characterization of SiC-SiC composites for accident tolerant fuel cladding, J. Nucl. Mater. 466 (2015) 1–15. https://doi.org/10.1016/j.jnucmat.2015.08.020.

[27]   T. Koyanagi, Y. Katoh, Mechanical properties of SiC composites neutron irradiated under light water reactor relevant temperature and dose conditions, J. Nucl. Mater. 494 (2017) 46–54. https://doi.org/10.1016/j.jnucmat.2017.07.007.

[28]   V. Angelici Avincola, K. Fitzgerald, D. Shepherd, D. Kinay, C. Sauder, M. Steinbrueck, High-temperature tests of silicon carbide composite cladding under GFR conditions, Energy Procedia. 127 (2017) 320–328. https://doi.org/10.1016/j.egypro.2017.08.116.

[29]   K. Lee, D. Kim, Y.S. Yoon, SiC/Si thin film deposited on zircaloy to improved accident tolerant

132

fuel cladding, Thin Solid Films. 660 (2018) 221–230. https://doi.org/10.1016/j.tsf.2018.06.006.

[30]   C. Tang, M. Stueber, H.J. Seifert, M. Steinbrueck, Protective coatings on zirconium-based alloys as accident-Tolerant fuel (ATF) claddings, Corros. Rev. 35 (2017) 141–165. https://doi.org/10.1515/corrrev-2017-0010.

[31]   K. Barrett, S. Bragg-Sitton, D. Galicki, Advanced LWR Nuclear Fuel Cladding System Development Trade-off Study, Idaho 83415 INL/EXT-12-27090. (2012) 1–34. https://doi.org/10.2172/1057698.

[32]   R. Hui, W. Cook, C. Sun, Y. Xie, P. Yao, J. Miles, R. Olive, J. Li, W. Zheng, L. Zhang, Deposition, characterization and performance evaluation of ceramic coatings on metallic substrates for supercritical water-cooled reactors, Surf. Coatings Technol. 205 (2011) 3512–3519. https://doi.org/10.1016/j.surfcoat.2010.12.017.

[33]   H.G. Kim, I.H. Kim, Y. Il Jung, D.J. Park, J.H. Park, B.K. Choi, Y.H. Lee, Out-of-pile performance of surface-modified Zr cladding for accident tolerant fuel in LWRs, J. Nucl. Mater. 510 (2018) 93–99. https://doi.org/10.1016/j.jnucmat.2018.07.061.

[34]   H.G. Kim, I.H. Kim, J.Y. Park, Y.H. Koo, Application of Coating Technology on Zirconium-Based Alloy to Decrease High-Temperature Oxidation, Zircon. Nucl. Ind. 17th Vol. (2015) 346–369. https://doi.org/10.1520/stp154320120161.

[35]   H.G. Kim, I.H. Kim, Y. Il Jung, D.J. Park, J.Y. Park, Y.H. Koo, Adhesion property and high-temperature oxidation behavior of Cr-coated Zircaloy-4 cladding tube prepared by 3D laser coating, J. Nucl. Mater. 465 (2015) 531–539. https://doi.org/10.1016/j.jnucmat.2015.06.030.

[36]   B. Maier, H. Yeom, G. Johnson, T. Dabney, J. Walters, J. Romero, H. Shah, P. Xu, K. Sridharan, Development of Cold Spray Coatings for Accident-Tolerant Fuel Cladding in Light Water Reactors, Jom. 70 (2018) 198–202. https://doi.org/10.1007/s11837-017-2643-9.

[37]   K. Shirvan, V. Champagne, A. Seshadri, M. Wagih, A. Gurgen, M. Ševeček, B. Phillips, Y. Che, Development of Cr cold spray–coated fuel cladding with enhanced accident tolerance, Nucl. Eng. Technol. 50 (2018) 229–236. https://doi.org/10.1016/j.net.2017.12.011.

[38]   M. Shahin, J. Petrik, A. Seshadri, B. Phillips, K. Shirvan, Experimental investigation of cold-spray chromium cladding, Topfuel. (2018) 1–10.

[39]   J.C. Brachet, I. Idarraga-Trujillo, M. Le Flem, M. Le Saux, V. Vandenberghe, S. Urvoy, E. Rouesne, T. Guilbert, C. Toffolon-Masclet, M. Tupin, C. Phalippou, F. Lomello, F. Schuster, A. Billard, G. Velisa, C. Ducros, F. Sanchette, Early studies on Cr-Coated Zircaloy-4 as enhanced accident tolerant nuclear fuel claddings for light water reactors, J. Nucl. Mater. 517 (2019) 268–285. https://doi.org/10.1016/j.jnucmat.2019.02.018.

[40]   A. Aubert, R. Gillet, A. Gaucher, J.P. Terrat, Hard chrome coatings deposited by physical vapour deposition, Thin Solid Films. 108 (1983) 165–172. https://doi.org/10.1016/0040-6090(83)90501-1.

[41]   A.S. Kuprin, V.A. Belous, V.N. Voyevodin, R.L. Vasilenko, V.D. Ovcharenko, G.D. Tolstolutskaya, I.E. Kopanets, I. V. Kolodiy, Irradiation resistance of vacuum arc chromium coatings for zirconium alloy fuel claddings, J. Nucl. Mater. 510 (2018) 163–167. https://doi.org/10.1016/j.jnucmat.2018.07.063.

[42]   D. V. Sidelev, E.B. Kashkarov, M.S. Syrtanov, V.P. Krivobokov, Nickel-chromium (Ni–Cr) coatings deposited by magnetron sputtering for accident tolerant nuclear fuel claddings, Surf. Coatings Technol. 369 (2019) 69–78. https://doi.org/10.1016/j.surfcoat.2019.04.057.

[43]   M. Wagih, B. Spencer, J. Hales, K. Shirvan, Fuel performance of chromium-coated zirconium alloy and silicon carbide accident tolerant fuel claddings, Ann. Nucl. Energy. 120 (2018) 304–318. https://doi.org/10.1016/j.anucene.2018.06.001.

[44]   H.G. Kim, Y.I. Jung, J.H. Park, D.J. Park, Y.H. Koo, J. Park, High temperature steam-oxidation behavior of arc ion plated Cr coatings for accident tolerant fuel claddings, Surf. Coatings Technol. 280 (2015) 256–259. https://doi.org/10.1016/j.surfcoat.2015.09.022.

[45]   J. Bischoff, C. Delafoy, C. Vauglin, P. Barberis, C. Roubeyrie, D. Perche, D. Duthoo, F. Schuster, J.C. Brachet, E.W. Schweitzer, K. Nimishakavi, AREVA NP's enhanced accident-tolerant fuel developments: Focus on Cr-coated M5 cladding, Nucl. Eng. Technol. 50 (2018) 223–228.

https://doi.org/10.1016/j.net.2017.12.004.

[46] A. Wu, J. Ribis, J.C. Brachet, E. Clouet, F. Leprêtre, E. Bordas, B. Arnal, HRTEM and chemical study of an ion-irradiated chromium/zircaloy-4 interface, J. Nucl. Mater. 504 (2018) 289–299. https://doi.org/10.1016/j.jnucmat.2018.01.029.

[47] J.-C. Brachet, M. Le Saux, M. Tupin, I. Idarraga-Trujillo, M. Le Flem, D. Hamon, S. Muller, V. Vandenberghe, E. Papin, E. Monsifrot, A. Billard, F. Schuster, Assessment at CEA of coated nuclear fuel cladding for LWRs with increasing margins in LOCA and beyond LOCA conditions Coatings for mechanical applications View project Plasma nitriding of austenitic stainless steel View project 860 Assessment At Cea of Co, (2013) 860–867. https://www.researchgate.net/publication/268801031.

[48] J.C. Brachet, M. Dumerval, V. Lezaud-Chaillioux, M. Le Saux, E. Rouesne, D. Hamon, S. Urvoy, T. Guilbert, Q. Houmaire, C. Cobac, G. Nony, J. Rousselot, F. Lomello, F. Schuster, H. Palancher, J. Bischoff, E. Pouillier, Behavior of Chromium Coated M5 Claddings under LOCA Conditions, 2017 Water React. Fuel Perform. Meet. 2017 Water React. Fuel Perform. Meet. (2017) 1–11.

[49] H.O. Behavior, O.F.C. Zirconium, H. Kim, I. Kim, Y. Jung, D. Park, J. Park, Y. Koo, I. Introduction, High-Temperature Oxidation Behavior of Cr-Coated Zirconium Alloy, (2013) 842–846.

[50] M. Ševecek, J. Krejci, M.H. Shahin, J. Petrik, R.G. Ballinger, K. Shirvan, Fatigue Behavior of Cold Spray - Coated Accident Tolerant, Topfuel. (2018) 1–15.

[51] J.M. Kim, T.H. Ha, I.H. Kim, H.G. Kim, Microstructure and oxidation behavior of CrAl laser-coated Zircaloy-4 alloy, Metals (Basel). 7 (2017) 1–7. https://doi.org/10.3390/met7020059.

[52] K.O. Legg, M. Graham, P. Chang, F. Rastagar, A. Gonzales, B. Sartwell, The replacement of electroplating, Surf. Coatings Technol. 81 (1996) 99–105. https://doi.org/10.1016/0257-8972(95)02653-3.

[53] L. D'Avico, R. Beltrami, N. Lecis, S. Trasatti, Corrosion Behavior and Surface Properties of PVD Coatings for Mold Technology Applications, Coatings. 9 (2018) 7.

135

https://doi.org/10.3390/coatings9010007.

[54]   J. Krejci, M. Sevecek, Development of Chromium and Chromium Nitride Coated Cladding 2017
        Water Reactor Fuel Performance Meeting, (2017).

[55]   B. Fotovvati, N. Namdari, A. Dehghanghadikolaei, On Coating Techniques for Surface Protection:
        A Review, J. Manuf. Mater. Process. 3 (2019) 28. https://doi.org/10.3390/jmmp3010028.

[56]   Donald M . Mattox, V. Coaters, Physical Vapor Deposition (PVD) Processes, Vacuum. (n.d.).

[57]   Cold-Spray Coatings Recent Trends and Future perspectives, 1st ed. 20, 2018.

[58]   K.G. Geelhood, W.G. Luscher, Degradation and Failure Phenomena of Accident Tolerant Fuel
        Concepts, (2019).

[59]   E.D. Lahoda, F. Boylan, Overview of Westinghouse Lead Accident Tolerant Fuel Program, (2019)
        1–7.

[60]   H. Yeom, B. Maier, G. Johnson, T. Dabney, M. Lenling, P. Scallon, J. Romero, J. Walters, P. Xu,
        H. Shah, K. Sridharan, Cold spray coatings for accident tolerant Zr-alloy cladding in light water
        reactors, Trans. Am. Nucl. Soc. 118 (2018) 1576–1579.

[61]   H. Shah, J. Romero, P. Xu, R. Oelrich, J. Walters, J. Wright, W. Gassmann, Westinghouse-Exelon
        EnCore ® Fuel Lead Test Rod (LTR) Program including Coated cladding Development and
        Advanced Pellets, Topfuel. (2018) 1–9.

[62]   H. Shah, J. Romero, P. Xu, B. Maier, G. Johnson, J. Walters, T. Dabney, H. Yeom, K. Sridharan,
        Development of Surface Coatings for Enhanced Accident Tolerant Fuel, Water React. Fuel
        Perform. Meet. (2017).

[63]   H.G. Kim, J.H. Yang, W.J. Kim, Y.H. Koo, Development Status of Accident-tolerant Fuel for
        Light Water Reactors in Korea, Nucl. Eng. Technol. 48 (2016) 1–15.
        https://doi.org/10.1016/j.net.2015.11.011.

[64]   R. Van Nieuwenhove, V. Andersson, J. Balak, B. Oberländer, In-Pile Testing of CrN, TiAlN, and
        AlCrN Coatings on Zircaloy Cladding in the Halden Reactor, Zircon. Nucl. Ind. 18th Int. Symp.
        (2018) 965–982. https://doi.org/10.1520/stp159720160011.

136

[65]   J.-P. Gilbon, D. & Soniak, A. & Doriot, S. & Mardon, Irradiation creep and growth behavior, and microstructural evolution of advanced Zr-base alloys, ASTM Spec. Tech. Publ. 51–73 (2000).

[66]   T.R. Allen, R.J.M. Konings, A.T. Motta, Corrosion of Zirconium Alloys, 1st ed., Elsevier Inc., 2012. https://doi.org/10.1016/B978-0-08-056033-5.00063-X.

[67]   J.C. Brachet, M. Le Saux, M. Le Flem, S. Urvoy, E. Rouesne, T. Guilbert, C. Cobac, F. Lahogue, J. Rousselot, M. Tupin, P. Billaud, C. Hossepied, F. Schuster, F. Lomello, A. Billard, G. Velisa, E. Monsifrot, J. Bischoff, A. Ambard, On-going studies at CEA on chromium coated zirconium based nuclear fuel claddings for enhanced Accident Tolerant LWRs Fuel, LWR Fuel Performance/TopFuel/WRFPM. (2015) 31–38.

[68]   J.C.C. Brachet, C. Lorrette, A. Michaux, C. Sauder, I. Idarraga-Trujillo, M. Le Saux, M. Le Flem, F. Schuster, A. Billard, E. Monsifrot, E. Torres, F. Rebillat, J. Bischoff, A. Ambard, CEA studies on advanced nuclear fuel claddings for enhanced Accident Tolerant LWRs Fuel(LOCA and beyond LOCA conditions), FONTEVRAUD 8- Contrib. Mater. Investig. Oper. Exp. to LWRs' Safety, Perform. Reliab. (2014) 10. https://doi.org/10.13140/2.1.5105.6325.

[69]   F. and B. Brachet, JC and Le Saux, M and Guilbert, T and Urvoy, S and Rouesne, E and Le Flem, M and Idarraga-Trujillo, I and Schuster, F and Lomello, Chromium Coated Nuclear Fuel Claddings for Enhanced Accident Tolerant LWRs fuel, in: IAEA Tech. Meetibf on" Ac-Cident Toler. Concepts LWRs". USA Oak Ridge Na-Tional Lab., 2014.

[70]   V. V. Bryk, V.N. Voyevodin, I.M. Neklyudov, A.N. Rakitskij, Microstructure investigation of Cr and Cr alloys irradiated with heavy ions, J. Nucl. Mater. 225 (1995) 146–153. https://doi.org/10.1016/0022-3115(95)00066-6.

[71]   A. Jain, S. Loganathan, J.D. Kanjilal, G.K. Mehta, High energy heavy ion irradiation of chromium films, Vacuum. 46 (1995) 369–371. https://doi.org/10.1016/0042-207X(94)00081-6.

[72]   C.W. Weaver, Irradiation and the ductility of chromium, Scr. Metall. 2 (1968) 463–466. https://doi.org/10.1016/0036-9748(68)90195-6.

[73]   A. Wu, J. Ribis, J.C. Brachet, E. Clouet, F. Leprêtre, E. Bordas, B. Arnal, G.S. Was, HRTEM and

137

chemical study of an ion-irradiated chromium/zircaloy-4 interface, J. Nucl. Mater. 504 (2018) 289–299. https://doi.org/10.1016/j.jnucmat.2018.01.029.

[74]   Y. Lee, J.I. Lee, H.C. NO, Mechanical analysis of surface-coated zircaloy cladding, Nucl. Eng. Technol. 49 (2017) 1031–1043. https://doi.org/10.1016/j.net.2017.03.012.

[75]   K.G. Field, Y. Yamamoto, B.A. Pint, M.N. Gussev, K.A. Terrani, Accident tolerant fecral fuel cladding: current status towards commercialization, Miner. Met. Mater. Ser. (2019) 1381–1389. https://doi.org/10.1007/978-3-030-04639-2_91.

[76]   V.K. Gupta, M. Larsen, R.B. Rebak, Utilizing FeCrAl oxidation resistance properties in water, air and steam for accident tolerant fuel cladding, ECS Trans. 85 (2018) 3–12. https://doi.org/10.1149/08502.0003ecst.

[77]   D.J. Park, H.G. Kim, Y. Il Jung, J.H. Park, J.H. Yang, Y.H. Koo, Behavior of an improved Zr fuel cladding with oxidation resistant coating under loss-of-coolant accident conditions, J. Nucl. Mater. 482 (2016) 75–82. https://doi.org/10.1016/j.jnucmat.2016.10.021.

[78]   D.J. Park, H.G. Kim, J.Y. Park, Y. Il Jung, J.H. Park, Y.H. Koo, A study of the oxidation of FeCrAl alloy in pressurized water and high-temperature steam environment, Corros. Sci. 94 (2015) 459–465. https://doi.org/10.1016/j.corsci.2015.02.027.

[79]   B. A. Pint, L. A. Baldesberger and K. A. Kane, Steam Oxidation, Burst and Critical Heat Flux Testing of Commercial FeCrAl Cladding, (2019) 311–316.

[80]   K.G. Field, X. Hu, K.C. Littrell, Y. Yamamoto, L.L. Snead, Radiation tolerance of neutron-irradiated model Fe-Cr-Al alloys, J. Nucl. Mater. 465 (2015) 746–755. https://doi.org/10.1016/j.jnucmat.2015.06.023.

[81]   E. Aydogan, J.S. Weaver, S.A. Maloy, O. El-Atwani, Y.Q. Wang, N.A. Mara, Microstructure and mechanical properties of FeCrAl alloys under heavy ion irradiations, J. Nucl. Mater. 503 (2018) 250–262. https://doi.org/10.1016/j.jnucmat.2018.03.002.

[82]   K.G. Field, S.A. Briggs, K. Sridharan, R.H. Howard, Y. Yamamoto, Mechanical properties of neutron-irradiated model and commercial FeCrAl alloys, J. Nucl. Mater. 489 (2017) 118–128.

138

https://doi.org/10.1016/j.jnucmat.2017.03.038.

[83]   N.M. George, K. Terrani, J. Powers, A. Worrall, I. Maldonado, Neutronic analysis of candidate

accident-tolerant cladding concepts in pressurized water reactors, Ann. Nucl. Energy. 75 (2015)

703–712. https://doi.org/10.1016/j.anucene.2014.09.005.

[84]   P.D. Edmondson, S.A. Briggs, Y. Yamamoto, R.H. Howard, K. Sridharan, K.A. Terrani, K.G.

Field, Irradiation-enhanced α′ precipitation in model FeCrAl alloys, Scr. Mater. 116 (2016) 112–

116. https://doi.org/10.1016/j.scriptamat.2016.02.002.

[85]   K.G. Field, M. Snead, Y. Yamamoto, B.A. Pint, K.A. Terrani, Materials properties of FeCrAl

alloys for nuclear power production applications, (2017) 39.

[86]   Y.H. Lee, T.S. Byun, A comparative study on the wear behaviors of cladding candidates for

accident-tolerant fuel, J. Nucl. Mater. 465 (2015) 857–865.

https://doi.org/10.1016/j.jnucmat.2015.05.017.

[87]   Y. He, J. Liu, S. Qiu, Z. Deng, Y. Yang, A. McLean, Microstructure and high temperature

mechanical properties of as-cast FeCrAl alloys, Mater. Sci. Eng. A. 726 (2018) 56–63.

https://doi.org/10.1016/j.msea.2018.04.039.

[88]   ORNL, Handbook on the Material Properties of FeCrAl alloys for Nuclear Power Production

Applications, 2017.

[89]   R.B. Rebak, K. a. Terrani, R.M. Fawcett, FeCrAl Alloys for Accident Tolerant Fuel Cladding in

Light Water Reactors, (2016) V06BT06A009. https://doi.org/10.1115/PVP2016-63162.

[90]   Z. Chen, J. Cai, R. Liu, Y. Wang, Preliminary thermal hydraulic analysis of various accident

tolerant fuels and claddings for control rod ejection accidents in LWRs, Nucl. Eng. Des. 331

(2018) 282–294. https://doi.org/10.1016/j.nucengdes.2018.03.007.

[91]   B. Zohuri, N. Fathi, Thermal-Hydraulic Analysis of Nuclear Reactors, 2015.

https://doi.org/10.1007/978-3-319-17434-1.

[92]   R.J. Goldstein, E.R.G. Eckert, W.E. Ibele, S. V. Patankar, T.W. Simon, T.H. Kuehn, P.J.

Strykowski, K.K. Tamma, A. Bar-Cohen, J.V.R. Heberlein, J.H. Davidson, J. Bischof, F.A.

Kulacki, U. Kortshagen, S. Garrick, V. Srinivasan, Heat transfer - A review of 2002 literature, Int. J. Heat Mass Transf. 48 (2005) 819–927. https://doi.org/10.1016/j.ijheatmasstransfer.2004.10.011.

[93]   S. Whitaker, S. Whitaker, 10 – Heat Transfer with Boiling and Condensation, 1977. https://doi.org/10.1016/B978-0-08-017866-0.50016-2.

[94]   H.F. O'Hanley, Separate Effects of Surface Roughness, Wettability and Porosity on Boiling Heat Transfer and Critical Heat Flux and Optimization of Boiling Surfaces, Am. Inst. Phys. 024102 (2012) 1–161. https://doi.org/10.1063/1.4813450.

[95]   A.F. Ali, J.P. Gorton, N.R. Brown, K.A. Terrani, C.B. Jensen, Y. Lee, E.D. Blandford, Surface wettability and pool boiling Critical Heat Flux of Accident Tolerant Fuel cladding-FeCrAl alloys, Nucl. Eng. Des. 338 (2018) 218–231. https://doi.org/10.1016/j.nucengdes.2018.08.024.

[96]   D.C. Groeneveld, J.Q. Shan, A.Z. Vasić, L.K.H. Leung, A. Durmayaz, J. Yang, S.C. Cheng, A. Tanase, The 2006 CHF look-up table, Nucl. Eng. Des. 237 (2007) 1909–1922. https://doi.org/10.1016/j.nucengdes.2007.02.014.

[97]   S. Xie, M. Shahmohammadi Beni, J. Cai, J. Zhao, Review of critical-heat-flux enhancement methods, Int. J. Heat Mass Transf. 122 (2018) 275–289. https://doi.org/10.1016/j.ijheatmasstransfer.2018.01.116.

[98]   S. Mori, Y. Utaka, Critical heat flux enhancement by surface modification in a saturated pool boiling: A review, Int. J. Heat Mass Transf. 108 (2017) 2534–2557. https://doi.org/10.1016/j.ijheatmasstransfer.2017.01.090.

[99]   N. Zuber, Hydrodynamic Aspects Of Boiling Heat Transfer (Thesis), (1959). https://doi.org/10.2172/4175511.

[100] S.J. Kim, I.C. Bang, J. Buongiorno, L.W. Hu, Effects of nanoparticle deposition on surface wettability influencing boiling heat transfer in nanofluids, Appl. Phys. Lett. 89 (2006). https://doi.org/10.1063/1.2360892.

[101] A. Ali, H.G. Kim, K. Hattar, S. Briggs, D. Jun Park, J. Hwan Park, Y. Lee, Ion irradiation effects on Cr-coated zircaloy-4 surface wettability and pool boiling critical heat flux, Nucl. Eng. Des. 362

(2020) 110581. https://doi.org/10.1016/j.nucengdes.2020.110581.

[102] C.Y. Lee, T.H. Chun, W.K. In, Critical heat flux of oxidized zircaloy surface in saturated water pool boiling, J. Nucl. Sci. Technol. 52 (2015) 596–606. https://doi.org/10.1080/00223131.2014.956830.

[103] K.N. Almilaji, Fabricating Superhydrophobic and Superoleophobic Surfaces with Multiscale Roughness Using Airbrush and Electrospray, (2016).

[104] M.R. Kashinath, Parameters Affecting Critical Heat Flux of Nanofluids: Heater Size, Pressure Orientation and Anti-Freeze Addition, (2006).

[105] P.J. Berenson, Transition boiling heat transfer from a horizontal surface, (1960) NP-8415.

[106] K.H. Chu, R. Enright, E.N. Wang, Structured surfaces for enhanced pool boiling heat transfer, Appl. Phys. Lett. 100 (2012). https://doi.org/10.1063/1.4724190.

[107] H.S. Ahn, C. Lee, H. Kim, H. Jo, S. Kang, J. Kim, J. Shin, M.H. Kim, Pool boiling CHF enhancement by micro/nanoscale modification of zircaloy-4 surface, Nucl. Eng. Des. 240 (2010) 3350–3360. https://doi.org/10.1016/j.nucengdes.2010.07.006.

[108] H.S. Ahn, H.J. Jo, S.H. Kang, M.H. Kim, Effect of liquid spreading due to nano/microstructures on the critical heat flux during pool boiling, Appl. Phys. Lett. 98 (2011) 98–101. https://doi.org/10.1063/1.3555430.

[109] H. Jo, J.M. Kim, H. Yeom, G.C. Lee, H.S. Park, M. Kiyofumi, M.H. Kim, K. Sridharan, M. Corradini, Boiling performance and material robustness of modified surfaces with multi scale structures for fuel cladding development, Nucl. Eng. Des. 291 (2015) 204–211. https://doi.org/10.1016/j.nucengdes.2015.04.032.

[110] S. Kim, H.D. Kim, H. Kim, H.S. Ahn, H. Jo, J. Kim, M.H. Kim, Effects of nano-fluid and surfaces with nano structure on the increase of CHF, Exp. Therm. Fluid Sci. 34 (2010) 487–495. https://doi.org/10.1016/j.expthermflusci.2009.05.006.

[111] S.G. Liter, M. Kaviany, Pool-boiling CHF enhancement by modulated porous-layer coating: Theory and experiment, Int. J. Heat Mass Transf. 44 (2001) 4287–4311.

141

https://doi.org/10.1016/S0017-9310(01)00084-9.

[112] L. Dong, X. Quan, P. Cheng, An experimental investigation of enhanced pool boiling heat transfer from surfaces with micro/nano-structures, Int. J. Heat Mass Transf. 71 (2014) 189–196. https://doi.org/10.1016/j.ijheatmasstransfer.2013.11.068.

[113] H. Jo, H.S. Ahn, S. Kang, M.H. Kim, A study of nucleate boiling heat transfer on hydrophilic, hydrophobic and heterogeneous wetting surfaces, Int. J. Heat Mass Transf. 54 (2011) 5643–5652. https://doi.org/10.1016/j.ijheatmasstransfer.2011.06.001.

[114] Y.H. Jeong, W.J. Chang, S.H. Chang, Wettability of heated surfaces under pool boiling using surfactant solutions and nano-fluids, Int. J. Heat Mass Transf. 51 (2008) 3025–3031. https://doi.org/10.1016/j.ijheatmasstransfer.2007.09.023.

[115] S. Mori, N. Maruoka, K. Okuyama, Critical heat flux enhancement by a two-layer structured honeycomb porous plate in a saturated pool boiling of water, Int. J. Heat Mass Transf. 118 (2018) 429–438. https://doi.org/10.1016/j.ijheatmasstransfer.2017.10.100.

[116] H.H. Son, G.H. Seo, U. Jeong, D.Y. Shin, S.J. Kim, Capillary wicking effect of a Cr-sputtered superhydrophilic surface on enhancement of pool boiling critical heat flux, Int. J. Heat Mass Transf. 113 (2017) 115–128. https://doi.org/10.1016/j.ijheatmasstransfer.2017.05.055.

[117] G.H. Seo, G. Jeun, S.J. Kim, Enhanced pool boiling critical heat flux with a FeCrAl layer fabricated by DC sputtering, Int. J. Heat Mass Transf. 102 (2016) 1293–1307. https://doi.org/10.1016/j.ijheatmasstransfer.2016.06.077.

[118] G.M. Son, K.M. Kim, I.C. Bang, Chromia coating with nanofluid deposition and sputtering for accident tolerance, CHF enhancement, Int. J. Heat Mass Transf. 118 (2018) 890–899. https://doi.org/10.1016/j.ijheatmasstransfer.2017.11.060.

[119] D.H. Kam, J.H. Lee, T. Lee, Y.H. Jeong, Critical heat flux for SiC- and Cr-coated plates under atmospheric condition, Ann. Nucl. Energy. 76 (2015) 335–342. https://doi.org/10.1016/j.anucene.2014.09.046.

[120] N. Kim, H.H. Son, S.J. Kim, Oxidation effect on pool boiling critical heat flux enhancement of Cr-

coated surface for accident-tolerant fuel cladding application, Int. J. Heat Mass Transf. 144 (2019) 118655. https://doi.org/10.1016/j.ijheatmasstransfer.2019.118655.

[121] H. Hyun, Y. Sik, S. Joong, Experimental study of saturated pool boiling heat transfer with FeCrAl- and Cr-layered vertical tubes under atmospheric pressure, Int. J. Heat Mass Transf. 128 (2019) 418–430. https://doi.org/10.1016/j.ijheatmasstransfer.2018.09.013.

[122] H.D. Kim, M.H. Kim, Effect of nanoparticle deposition on capillary wicking that influences the critical heat flux in nanofluids, Appl. Phys. Lett. 91 (2007) 1–4. https://doi.org/10.1063/1.2754644.

[123] M.M. Rahman, E. Ölçeroglu, M. McCarthy, Role of wickability on the critical heat flux of structured superhydrophilic surfaces, Langmuir. 30 (2014) 11225–11234. https://doi.org/10.1021/la5030923.

[124] G.H. Seo, U. Jeong, H.H. Son, D. Shin, S.J. Kim, Effects of layer-by-layer assembled PEI/MWCNT surfaces on enhanced pool boiling critical heat flux, Int. J. Heat Mass Transf. 109 (2017) 564–576. https://doi.org/10.1016/j.ijheatmasstransfer.2017.02.014.

[125] C.N. Laboratories, G.A. Mcrae, Effect of Oxidation and Fractal Surface Roughness on the Wettability and Critical Heat Flux of Glass-Peened Zirconium Alloy Tubes, (2003). https://doi.org/10.13140/2.1.1884.8008.

[126] H.J. Jo, H. Yeom, E. Gutierrez, K. Sridharan, M. Corradini, Evaluation of critical heat flux of ATF candidate coating materials in pool boiling, Nucl. Eng. Des. 354 (2019) 110166. https://doi.org/10.1016/j.nucengdes.2019.110166.

[127] A. Nazari, S. Saedodin, Critical heat flux enhancement of pool boiling using a porous nanostructured coating, Exp. Heat Transf. 30 (2017) 316–327. http://www.tandfonline.com/doi/abs/10.1080/08916152.2016.1249806.

[128] S.K. Lee, M. Liu, N.R. Brown, K.A. Terrani, E.D. Blandford, H. Ban, C.B. Jensen, Y. Lee, Comparison of steady and transient flow boiling critical heat flux for FeCrAl accident tolerant fuel cladding alloy , Zircaloy , and Inconel, Int. J. Heat Mass Transf. 132 (2019) 643–654.

https://doi.org/10.1016/j.ijheatmasstransfer.2018.11.141.

[129] R.W.L. Fong, T. Nitheanandan, C.D. Bullock, L.F. Slater, G.A. McRae, Effect of oxidation and fractal surface roughness on the wettability and critical heat flux of class-peened zirconium alloy tubes., Proc. 5th Int. Conf. Boil. Heat Transf. (2003).

[130] B.J. Jones, J.P. McHale, S. V. Garimella, The Influence of Surface Roughness on Nucleate Pool Boiling Heat Transfer, J. Heat Transfer. 131 (2009) 121009. https://doi.org/10.1115/1.3220144.

[131] T.J. Hendricks, S. Krishnan, C. Choi, C.H. Chang, B. Paul, Enhancement of pool-boiling heat transfer using nanostructured surfaces on aluminum and copper, Int. J. Heat Mass Transf. 53 (2010) 3357–3365. https://doi.org/10.1016/j.ijheatmasstransfer.2010.02.025.

[132] H.T. Phan, N. Caney, P. Marty, S. Colasson, J. Gavillet, Surface wettability control by nanocoating: The effects on pool boiling heat transfer and nucleation mechanism, Int. J. Heat Mass Transf. 52 (2009) 5459–5471. https://doi.org/10.1016/j.ijheatmasstransfer.2009.06.032.

[133] R. Furberg, B. Palm, S. Li, M. Toprak, M. Muhammed, The Use of a Nano- and Microporous Surface Layer to Enhance Boiling in a Plate Heat Exchanger, J. Heat Transfer. 131 (2009) 101010. https://doi.org/10.1115/1.3180702.

[134] C.S. Sujith Kumar, S. Suresh, C.R. Aneesh, M.C. Santhosh Kumar, A.S. Praveen, K. Raji, Flow boiling heat transfer enhancement on copper surface using Fe doped Al2O3-TiO2composite coatings, Appl. Surf. Sci. 334 (2015) 102–109. https://doi.org/10.1016/j.apsusc.2014.08.076.

[135] D. SchroederRichter, S. Yildiz, Effect of porous coating on critical heat flux removed by subcooled water at low flow rates, Fusion Technol. 29 (1996) 512–518.

[136] J. Kim, S. Jun, R. Laksnarain, S.M. You, Effect of surface roughness on pool boiling heat transfer at a heated surface having moderate wettability, Int. J. Heat Mass Transf. 101 (2016) 992–1002. https://doi.org/10.1016/j.ijheatmasstransfer.2016.05.067.

[137] H.S. Jo, S. An, H.G. Park, M.W. Kim, S.S. Al-Deyab, S.C. James, J. Choi, S.S. Yoon, Enhancement of critical heat flux and superheat through controlled wettability of cuprous-oxide fractal-like nanotextured surfaces in pool boiling, Int. J. Heat Mass Transf. 107 (2017) 105–111.

144

https://doi.org/10.1016/j.ijheatmasstransfer.2016.11.029.

[138] H.H. Son, U. Jeong, G.H. Seo, S.J. Kim, Oxidation effect on the pool boiling critical heat flux of the carbon steel substrates, Int. J. Heat Mass Transf. 93 (2016) 1008–1019. https://doi.org/10.1016/j.ijheatmasstransfer.2015.10.047.

[139] J. Kim, S. Jun, J. Lee, J. Godinez, S.M. You, Effect of Surface Roughness on Pool Boiling Heat Transfer of Water on a Superhydrophilic Aluminum Surface, J. Heat Transfer. 139 (2017) 101501. https://doi.org/10.1115/1.4036599.

[140] M. Tetreault-Friend, R. Azizian, M. Bucci, T. McKrell, J. Buongiorno, M. Rubner, R. Cohen, Critical heat flux maxima resulting from the controlled morphology of nanoporous hydrophilic surface layers, Appl. Phys. Lett. 108 (2016). https://doi.org/10.1063/1.4954012.

[141] G. Cheol Lee, H. Noh, H. Yeom, H.J. Jo, T. Kyun Kim, M. Kim, K. Sridharan, H. Sun Park, Zirconium-silicide coating on zircaloy-4 substrate for accident tolerance: Effects on oxidation resistance and boiling, Ann. Nucl. Energy. 126 (2019) 350–358. https://doi.org/10.1016/j.anucene.2018.11.019.

[142] K.G. Lee, W.K. In, H.G. Kim, Quenching experiment on Cr-alloy-coated cladding for accident-tolerant fuel in water pool under low and high subcooling conditions, Nucl. Eng. Des. 347 (2019) 10–19. https://doi.org/10.1016/j.nucengdes.2019.03.017.

[143] C.L. Withmarsh, Review of Zircaloy-2 and Zircaloy-4 Properties Relevant to N.S. Savannah Reactor Design, (No. ORNL-3281). Oak Ridge Natl. Lab., Tenn.. 4500 (1962) 70. https://doi.org/Report No. ORNL-3281, UC-80-Reactor Technology, TID-4500 (17th ed.).

[144] R.B. Rebak, Y.P. Lin, Y.J. Kim, Review on electrochemical corrosion of zirconium alloys in high temperature water, in: 14th Int. Conf. Environ. Degrad. Mater. Nucl. Power Syst. Water React. 2009, 2009: pp. 1400–1406.

[145] A.T. Motta, A. Couet, R.J. Comstock, Corrosion of Zirconium Alloys Used for Nuclear Fuel Cladding, Annu. Rev. Mater. Res. 45 (2015) 311–343. https://doi.org/10.1146/annurev-matsci-070214-020951.

[146] V.F. Urbanic, T.R. Heidrick, High-temperature oxidation of zircaloy-2 and zircaloy-4 in steam, J. Nucl. Mater. 75 (1978) 251–261. https://doi.org/10.1016/0022-3115(78)90006-5.

[147] K.A. Terrani, B.A. Pint, C.M. Parish, C.M. Silva, L.L. Snead, Y. Katoh, Silicon carbide oxidation in steam up to 2 MPa, J. Am. Ceram. Soc. 97 (2014) 2331–2352. https://doi.org/10.1111/jace.13094.

[148] T. Cheng, J.R. Keiser, M.P. Brady, K.A. Terrani, B.A. Pint, Oxidation of fuel cladding candidate materials in steam environments at high temperature and pressure, J. Nucl. Mater. 427 (2012) 396–400. https://doi.org/10.1016/j.jnucmat.2012.05.007.

[149] Nuclear Energy Agency, Nuclear Fuel Behaviour Under Reactivity-initiated Accident (RIA) Conditions, 2010. http://dx.doi.org/10.1016/j.nucengdes.2010.08.017%0Ahttp://dx.doi.org/10.1016/j.anucene.2012.09.016%0Ahttp://www.nss.si/proc/port2007/htm/pdf/202.pdf%0Ahttp://www.iaea.org/inis/collection/NCLCollectionStore/_Public/44/100/44100530%0Ahttp://dx.doi.org/10.1.

[150] S.J. Zinkle, G.S. Was, Materials challenges in nuclear energy, Acta Mater. 61 (2013) 735–758. https://doi.org/10.1016/j.actamat.2012.11.004.

[151] B.A. Pint, K.A. Terrani, M.P. Brady, T. Cheng, J.R. Keiser, High temperature oxidation of fuel cladding candidate materials in steam – hydrogen environments, J. Nucl. Mater. 440 (2013) 420–427. https://doi.org/10.1016/j.jnucmat.2013.05.047.

[152] R. V. Umretiya, B. Elward, D. Lee, M. Anderson, R.B. Rebak, J. V. Rojas, Mechanical and Chemical Properties of PVD and Cold Spray Cr-coatings on Zircaloy-4, J. Nucl. Mater. 541 (2020) 152420. https://doi.org/10.1016/j.jnucmat.2020.152420.

[153] IAEA Tecdoc Series, Accident Tolerant Fuel Concepts for Light Water Reactors, in: Proc. Tech. Meet. Held Oak Ridge Natl. Lab., 2014.

[154] A. Np, AREVA's Enhanced Accident Tolerant Fuel (EATF) Program, (2017).

[155] H.G. Kim, I.H. Kim, J.Y. Park, Y.H. Koo, Application of Coating Technology on Zirconium-Based Alloy to Decrease High-Temperature Oxidation, Zircon. Nucl. Ind. 17th Vol. (2014) 346–

369. https://doi.org/10.1520/stp154320120161.

[156] J.C. Brachet, M. Le Saux, V. Lezaud-Chaillioux, M. Dumerval, Q. Houmaire, F. Lomello, F. Schuster, E. Monsifrot, J. Bischoff, E. Pouillier, Behavior under LOCA conditions of Enhanced Accident Tolerant Chromium Coated Zircaloy-4 Claddings, Top Fuel 2016. (2016) 1173–1178.

[157] B. Cheng, Y.J. Kim, P. Chou, Improving Accident Tolerance of Nuclear Fuel with Coated Mo-alloy Cladding, Nucl. Eng. Technol. 48 (2016) 16–25. https://doi.org/10.1016/j.net.2015.12.003.

[158] R.B. Rebak, Alloy Selection for Accident Tolerant Fuel Cladding in Commercial Light Water Reactors, Metall. Mater. Trans. E. 2 (2015) 197–207. https://doi.org/10.1007/s40553-015-0057-6.

[159] K. Shimoda, T. Hinoki, H. Kishimoto, A. Kohyama, Enchanced high-temperature performances of SiC/SiC composites by high densification and crystalline structure, Compos. Sci. Technol. 71 (2011) 326–332. https://doi.org/10.1016/j.compscitech.2010.11.026.

[160] K. Yueh, K.A. Terrani, Silicon carbide composite for light water reactor fuel assembly applications, J. Nucl. Mater. 448 (2014) 380–388. https://doi.org/10.1016/j.jnucmat.2013.12.004.

[161] J.H. Perepezko, R. Sakidja, Oxidation-resistant coatings for ultra-high-temperature refractory Mo-based alloys, Jom. 62 (2010) 13–19. https://doi.org/10.1007/s11837-010-0148-x.

[162] R.B. Rebak, Advanced steels for accident tolerant fuel cladding in current light water reactors, Energy Mater. 2014, Conf. Proc. (2014) 433–442. https://doi.org/10.1007/978-3-319-48765-6_51.

[163] F.H. Stott, G.C. Wood, J. Stringer, The influence of alloying elements on the development and maintenance of protective scales, Oxid. Met. 44 (1995) 113–145. https://doi.org/10.1007/BF01046725.

[164] J. Ejenstam, M. Thuvander, P. Olsson, F. Rave, P. Szakalos, Microstructural stability of Fe-Cr-Al alloys at 450-550 °C, J. Nucl. Mater. 457 (2015) 291–297. https://doi.org/10.1016/j.jnucmat.2014.11.101.

[165] H.P. Qu, Y.P. Lang, C.F. Yao, H.T. Chen, C.Q. Yang, The effect of heat treatment on recrystallized microstructure, precipitation and ductility of hot-rolled Fe-Cr-Al-REM ferritic stainless steel sheets, Mater. Sci. Eng. A. 562 (2013) 9–16.

https://doi.org/10.1016/j.msea.2012.11.008.

[166] B.A. Pint, Performance of FeCrAl for accident-Tolerant fuel cladding in high-Temperature steam, Corros. Rev. 35 (2017) 167–175. https://doi.org/10.1515/corrrev-2016-0067.

[167] C. Badini, F. Laurella, Oxidation of FeCrAl alloy: Influence of temperature and atmosphere on scale growth rate and mechanism, Surf. Coatings Technol. 135 (2001) 291–298. https://doi.org/10.1016/S0257-8972(00)00989-0.

[168] K.A. Terrani, B.A. Pint, Y.J. Kim, K.A. Unocic, Y. Yang, C.M. Silva, H.M. Meyer, R.B. Rebak, Uniform corrosion of FeCrAl alloys in LWR coolant environments, J. Nucl. Mater. 479 (2016) 36–47. https://doi.org/10.1016/j.jnucmat.2016.06.047.

[169] K.A. Gamble, T. Barani, D. Pizzocri, J.D. Hales, K.A. Terrani, G. Pastore, An investigation of FeCrAl cladding behavior under normal operating and loss of coolant conditions, J. Nucl. Mater. 491 (2017) 55–66. https://doi.org/10.1016/j.jnucmat.2017.04.039.

[170] R.B. Rebak, Versatile Oxide Films Protect FeCrAl Alloys Under Normal Operation and Accident Conditions in Light Water Power Reactors, Jom. 70 (2018) 176–185. https://doi.org/10.1007/s11837-017-2705-z.

[171] R.B. Rebak, V.K. Gupta, M. Larsen, Oxidation Characteristics of Two FeCrAl Alloys in Air and Steam from 800°C to 1300°C, Jom. 70 (2018) 1484–1492. https://doi.org/10.1007/s11837-018-2979-9.

[172] KANTHAL-SANDVIK, Kanthal APMT Datasheet, 2012. https://doi.org/10.1061/9780784409732.ch09.

[173] Y. Yamamoto, M.N. Gussev, B.K. Kim, T.S. Byun, Optimized properties on base metal and thin-walled tube of Generation II ATF FeCrAl, 2015.

[174] W. Chubb, S. Alfant, A.A. Bauer, E.J. Jablonowski, F.R. Shober, R.F. Dickerson, C. de G. sobre o Alto-Mar, Constitution, metallurgy, and oxidation resistance of iron-chromium-aluminum alloys, 1958. https://scihub.tw/10.1002/iroh.19620470121%0Ahttp://www.osti.gov/servlets/purl/4290548/.

[175] E.A. Little, D.A. Stow, Void-swelling in irons and ferritic steels. II. An experimental survey of materials irradiated in a fast reactor, J. Nucl. Mater. 87 (1979) 25–39. https://doi.org/10.1016/0022-3115(79)90123-5.

[176] K.G. Field, S.A. Briggs, X. Hu, Y. Yamamoto, R.H. Howard, K. Sridharan, Heterogeneous dislocation loop formation near grain boundaries in a neutron-irradiated commercial FeCrAl alloy, J. Nucl. Mater. 483 (2017) 54–61. https://doi.org/10.1016/j.jnucmat.2016.10.050.

[177] I. Younker, M. Fratoni, Neutronic evaluation of coating and cladding materials for accident tolerant fuels, Prog. Nucl. Energy. 88 (2016) 10–18. https://doi.org/10.1016/j.pnucene.2015.11.006.

[178] J. Bischoff, C. Delafoy, N. Chaari, C. Vauglin, K. Buchanan, Cr-coated cladding development at Framatome, in: Top Fuel 2018 Light Water React. Fuel Perform. Meet. Sep 2018, Prague, Czech Republic. Cea-02328963, n.d.

[179] J.C. Brachet, T. Guilbert, M. Le Saux, J. Rousselot, G. Nony, C. Toffolon-Masclet, A. Michau, F. Schuster, H. Palancher, J. Bischoff, J. Augereau, E. Pouillier, Behavior of Cr-coated M5 Cladding during and after High Temperature Steam Oxidation from 800°C up to 1500°C (Loss-of-Coolant Accident & Design Extension Conditions), in: TopFuel 2018 (p. A0100). Prague, Czech Repub. Eur. Nucl. Soc., n.d.

[180] J. Bischoff, C. Vauglin, C. Delafoy, P. Barberis, D. Perche, Development of cr-coated zirconium alloy cladding for enhanced accident tolerance, in: Top Fuel 2016 Light Water React. Fuel Perform. Meet. Sep 2016, Boise, United States. Cea-0238699, n.d.

[181] R. Oelrich, S. Ray, Z. Karoutas, P. Xu, J. Romero, H. Shah, E. Lahoda, F. Boylan, Overview of Westinghouse leas Accident Tolerant Fuel Program, in: TopFuel 2018, Sept. 30 to Oct. 4, 2018, Prague, Czech Repub., n.d.

[182] A. Michau, F. Maury, F. Schuster, F. Lomello, J.C. Brachet, E. Rouesne, M. Le Saux, R. Boichot, M. Pons, High-temperature oxidation resistance of chromium-based coatings deposited by DLI-MOCVD for enhanced protection of the inner surface of long tubes, Surf. Coatings Technol. 349

(2018) 1048–1057. https://doi.org/10.1016/j.surfcoat.2018.05.088.

[183]   Y.P. Lin, R.M. Fawcett, S.S. Desilva, D.R. Lutz, M.O. Yilmaz, P. Davis, R.A. Rand, P.E. Cantonwine, R.B. Rebak, R. Dunavant, N. Satterlee, Path Towards Industrialization of Enhanced Accident Tolerant Fuel, in: TopFuel 2018, 2018: p. A0141.

[184]   C. Delafoy, J. Bischoff, Benefits of framatome's E-ATF evolutionary solution: Cr-coated cladding with Cr2O3-doped fuel, in: Topfuel, 2018: pp. 1–11.

[185]   G. Liang, I. Mudawar, Pool boiling critical heat flux (CHF) – Part 2: Assessment of models and correlations, Int. J. Heat Mass Transf. 117 (2018) 1368–1383. https://doi.org/10.1016/j.ijheatmasstransfer.2017.09.073.

[186]   C. Angle, Surface Wetting, Springer International Publishing, (2015), 1-162, n.d. https://doi.org/10.1007/978-3-319-25214-8.

[187]   S. Bin Seo, I.C. Bang, Effects of AL2O3nanoparticles deposition on critical heat flux of R-123 in flow boiling heat transfer, Nucl. Eng. Technol. 47 (2015) 398–406. https://doi.org/10.1016/j.net.2015.04.003.

[188]   V. Khanikar, I. Mudawar, T. Fisher, Effects of carbon nanotube coating on flow boiling in a micro-channel, Int. J. Heat Mass Transf. 52 (2009) 3805–3817. https://doi.org/10.1016/j.ijheatmasstransfer.2009.02.007.

[189]   ASTM International, Astm D 5725, 99 (1999) 1–7.

[190]   R. Coatings, Standard Practice for Surface Wettability of Coatings , Substrates and Pigments by Advancing Contact Angle Measurement 1, 08 (2018) 8–10. https://doi.org/10.1520/D7334-08R13.2.

[191]   M. Flynn, International Standard, 2003 (2003).

[192]   E.S. Gadelmawla, M.M. Koura, T.M.A. Maksoud, I.M. Elewa, H.H. Soliman, Roughness parameters, J. Mater. Process. Technol. 123 (2002) 133–145. https://doi.org/10.1016/S0924-0136(02)00060-2.

[193]   G. Bitelli, A. Simone, F. Girardi, C. Lantieri, Laser scanning on road pavements: A new approach

for characterizing surface texture, Sensors (Switzerland). 12 (2012) 9110–9128. https://doi.org/10.3390/s120709110.

[194] E2546-07, Standard Practice for Instrumented Indentation Testing, ASTM B. Stand. 1 (2007) 1–23. https://doi.org/10.1520/E2546-07.2.

[195] ASTM Internaional, ASTM E140-12b. Standard Hardness Conversion Tables for Metals Relationship Among Brinell Hardness, Vickers Hardness, Rockwell Hardness, Superficial Hardness, Knoop Hardness, Scleroscope Hardness, and Leeb Hardness, Am. Soc. Test. Mater. (2012) 1–25. https://doi.org/10.1520/E0140-12B.1.

[196] H.H. Son, S.J. Kim, Role of receding capillary flow correlating nano/micro scale surface roughness and wettability with pool boiling critical heat flux, Int. J. Heat Mass Transf. 138 (2019) 985–1001. https://doi.org/10.1016/j.ijheatmasstransfer.2019.04.091.

[197] M. Łępicka, M. Grądzka-Dahlke, The initial evaluation of performance of hard anti-wear coatings deposited on metallic substrates: thickness, mechanical properties and adhesion measurements – a brief review, Rev. Adv. Mater. Sci. 58 (2019) 50–65. https://doi.org/10.1515/rams-2019-0003.

[198] ASTM:D4541-09, Standard Test Method for Pull-Off Strength of Coatings Using Portable Adhesion, ASTM Int. (2014) 1–16. https://doi.org/10.1520/D4541-09E01.2.

[199] R. Umretiya, D. Ginestro, S. Bilbao y Leon, J. Rojas, B. Elward, M. Anderson, R.B. Rebak, Surface characteristics of accident tolerant fuels cladding and their potential impact in critical heat flux, in: 18th Int. Top. Meet. Nucl. React. Therm. Hydraul. NURETH, 2019.

[200] K.Y. Law, Definitions for hydrophilicity, hydrophobicity, and superhydrophobicity: Getting the basics right, J. Phys. Chem. Lett. 5 (2014) 686–688. https://doi.org/10.1021/jz402762h.

[201] A.W. Adamson, A.P. Gast, Physical Chemistry of Solid Surfaces, Nanostructures Nanomater. (2011) 19–60. https://doi.org/10.1142/9789814340571_0002.

[202] K.J. Kubiak, M.C.T. Wilson, T.G. Mathia, P. Carval, Wettability versus roughness of engineering surfaces, 271 (2011) 523–528.

[203] S. Veeramasuneni, J. Drelich, J.D. Miller, G. Yamauchi, Hydrophobicity of ion-plated PTFE

151

coatings, Prog. Org. Coatings. 31 (1997) 265–270. https://doi.org/10.1016/S0300-9440(97)00085-4.

[204] M. Panth, The physics of water droplets on surfaces : exploring the effects of roughness and surface chemistry, (2018). https://doi.org/10.1088/1361-6404/aa9cba.

[205] P.I.B.J. Heuser, Engineered Zircaloy Cladding Modifications for Improved Accident Tolerance of LWR Fuel, OECD/NEA Work. Accid. Toler. Fuels LWRs. (2012) 1.

[206] R. V Umretiya, S. Vargas, D. Galeano, R. Mohammadi, C.E. Castano, J. V Rojas, Effect of surface characteristics and environmental aging on wetting of Cr-coated Zircaloy-4 accident tolerant fuel cladding material, J. Nucl. Mater. (2020) 152163. https://doi.org/https://doi.org/10.1016/j.jnucmat.2020.152163.

[207] D. Fuloria, S. Goel, R. Jayaganthan, D. Srivastava, G.K. Dey, N. Saibaba, Mechanical properties and microstructural evolution of ultrafine grained zircaloy-4 processed through multiaxial forging at cryogenic temperature, Trans. Nonferrous Met. Soc. China (English Ed. 25 (2015) 2221–2229. https://doi.org/10.1016/S1003-6326(15)63835-3.

[208] X.T. Zu, K. Sun, M. Atzmon, L.M. Wang, L.P. You, F.R. Wan, J.T. Busby, G.S. Was, R.B. Adamson, Effect of proton and Ne irradiation on the microstructure of Zircaloy 4, Philos. Mag. 85 (2005) 649–659. https://doi.org/10.1080/14786430412331320017.

[209] X. Hernot, O. Bartier, Y. Bekouche, R. El Abdi, G. Mauvoisin, Influence of penetration depth and mechanical properties on contact radius determination for spherical indentation, Int. J. Solids Struct. 43 (2006) 4136–4153. https://doi.org/10.1016/j.ijsolstr.2005.06.007.

[210] H.G. Kim, I.H. Kim, Y. Il Jung, D.J. Park, J.Y. Park, Y.H. Koo, Adhesion property and high-temperature oxidation behavior of Cr-coated Zircaloy-4 cladding tube prepared by 3D laser coating, J. Nucl. Mater. 465 (2015) 531–539. https://doi.org/10.1016/j.jnucmat.2015.06.030.

[211] F. Cosset, G. Contoux, A. Celerier, J. Machet, Deposition of corrosion-resistant chromium and nitrogen-doped chromium coatings by cathodic magnetron sputtering, Surf. Coatings Technol. 79 (1996) 25–34. https://doi.org/10.1016/0257-8972(95)02454-9.

[212] G. Cholvy, J.L. Derep, M. Gantois, Characterization and wear resistance of coatings in the Cr-C-N ternary system deposited by physical vapour deposition, Thin Solid Films. 126 (1985) 51–60. https://doi.org/10.1016/0040-6090(85)90174-9.

[213] C.J. Lee, S.K. Lee, D.C. Ko, D.J. Kim, B.M. Kim, Evaluation of surface and bonding properties of cold rolled steel sheet pretreated by Ar/O 2 atmospheric pressure plasma at room temperature, J. Mater. Process. Technol. 209 (2009) 4769–4775. https://doi.org/10.1016/j.jmatprotec.2008.11.043.

[214] M. Ohring, Materials Science of Thin Films, 2nd ed., Elsevier Science, Burlington, 2001.

[215] A. Moarrefzadeh, Simulation and modeling of physical vapor deposition (PVD) process, WSEAS Trans. Appl. Theor. Mech. 7 (2012) 106–111.

[216] T.T. Chau, W.J. Bruckard, P.T.L. Koh, A. V. Nguyen, A review of factors that affect contact angle and implications for flotation practice, Adv. Colloid Interface Sci. 150 (2009) 106–115. https://doi.org/10.1016/j.cis.2009.07.003.

[217] Y.J. Lim, Y. Oshida, C.J. Andres, M.T. Barco, Surface characterizations of variously treated titanium materials., Int. J. Oral Maxillofac. Implants. 16 (n.d.) 333–42. http://www.ncbi.nlm.nih.gov/pubmed/11432653.

[218] K. Anselme, M. Bigerelle, Topography effects of pure titanium substrates on human osteoblast long-term adhesion, Acta Biomater. 1 (2005) 211–222. https://doi.org/10.1016/j.actbio.2004.11.009.

[219] V. Carey, Liquid-vapor phase-change phenomena : An introduction to the thermophysics of vaporization and condensation processes in heat transfer equipment, 2nd ed., Taylor and Francis., New York, 2008.

[220] Z. Yao, Y.W. Lu, S.G. Kandlikar, Pool Boiling Heat Transfer Enhancement Through Nanostructures on Silicon Microchannels, J. Nanotechnol. Eng. Med. 3 (2013) 031002. https://doi.org/10.1115/1.4007425.

[221] A. Jena, Wettability of Candidate Accident Tolerant Fuel (ATF) Cladding Materials in LWR conditions, Massachusetts Institute of Technology, 2020.

[222] A. Matthews, E. Broszeit, G. Berg, A. Leyland, C. Friedrich, W. Heinke, Evaluation of PVD nitride coatings, using impact, scratch and Rockwell-C adhesion tests, Thin Solid Films. 270 (2003) 431–438. https://doi.org/10.1016/0040-6090(95)06934-8.

[223] H. Yeom, E. Gutierrez, H.J. Jo, Y. Zhou, K. Mondry, K. Sridharan, M. Corradini, Pool boiling critical heat flux studies of accident tolerant fuel cladding materials, Nucl. Eng. Des. 370 (2020) 110919. https://doi.org/10.1016/j.nucengdes.2020.110919.

[224] L. Bónová, A. Zahoranová, D. Kováčik, M. Zahoran, M. Mičušík, M. Černák, Atmospheric pressure plasma treatment of flat aluminum surface, Appl. Surf. Sci. 331 (2015) 79–86. https://doi.org/10.1016/j.apsusc.2015.01.030.

[225] W. Polini, L. Sorrentino, Improving the wettability of 2024 aluminium alloy by means of cold plasma treatment, Appl. Surf. Sci. 214 (2003) 232–242. https://doi.org/10.1016/S0169-4332(03)00359-3.

[226] K.L. Mittal, A. Pizzi, Adhesion Promotion Techniques, 1st ed., CRC Press, 1999.

[227] V. Prysiazhnyi, Atmospheric Pressure Plasma Treatment and Following Aging Effect of Chromium Surfaces, J. Surf. Eng. Mater. Adv. Technol. 03 (2013) 138–145. https://doi.org/10.4236/jsemat.2013.32018.

[228] I. V. Minin, O. V. Minin, Elements of diffraction quasi-optics, 1994.

[229] B.D. Cullity, J.W. Weymouth, Elements of X-Ray Diffraction, Am. J. Phys. 25 (1957) 394–395.

[230] D. Kim, H. Kim, H. Kim, Y. Yang, Preliminary study of mechanical behavior for Cr coated Zr-4 Fuel Cladding, (2015) 7–9.

[231] Cladding Embrittlement During Postulated Loss-of-Coolant Accidents, (n.d.).

[232] H. Chen, L.X. Cai, Unified ring-compression model for determining tensile properties of tubular materials, Mater. Today Commun. 13 (2017) 210–220. https://doi.org/10.1016/j.mtcomm.2017.10.006.

[233] J.S. Koehler, Attempt to Design a Strong Solid, Phys. Rev. B. Volume 2 (1970).

[234] H. Ryou, J.W. Drazin, K.J. Wahl, S.B. Qadri, E.P. Gorzkowski, B.N. Feigelson, J.A.

154

Wollmershauser, Below the Hall-Petch Limit in Nanocrystalline Ceramics, ACS Nano. 12 (2018) 3083–3094. https://doi.org/10.1021/acsnano.7b07380.

[235] J. Chen, S.J. Bull, Approaches to investigate delamination and interfacial toughness in coated systems: An overview, J. Phys. D. Appl. Phys. 44 (2011). https://doi.org/10.1088/0022-3727/44/3/034001.

[236] B.R. Strohmeier, Improving the wettability of aluminum foil with oxygen plasma treatments, J. Adhes. Sci. Technol. 6 (1992) 703–718. https://doi.org/10.1163/156856192X01051.

[237] S.A. Shedid, M.T. Ghannam, Influences of droplet volume on contact angle of reservoir rocks, Energy Sources. 27 (2005) 1085–1097. https://doi.org/10.1080/00908310490479538.

[238] J. Drelich, J.D. Miller, J. Hupka, The effect of drop size on contact angle over a wide range of drop volumes, J. Colloid Interface Sci. 155 (1993) 379–385. https://doi.org/10.1006/jcis.1993.1050.

[239] F. Truica-Marasescu, S. Guimond, P. Jedrzejowski, M.R. Wertheimer, Hydrophobic recovery of VUV/NH3 modified polyolefin surfaces: Comparison with plasma treatments in nitrogen, Nucl. Instruments Methods Phys. Res. Sect. B Beam Interact. with Mater. Atoms. 236 (2005) 117–122. https://doi.org/10.1016/j.nimb.2005.03.266.

[240] A. Latifi, M. Imani, M.T. Khorasani, M. Daliri Joupari, Plasma surface oxidation of 316L stainless steel for improving adhesion strength of silicone rubber coating to metal substrate, Appl. Surf. Sci. 320 (2014) 471–481. https://doi.org/10.1016/j.apsusc.2014.09.084.

[241] F.M. Capece, V. Di Castro, C. Furlani, G. Mattogno, C. Fragale, M. Gargano, M. Rossi, "Copper chromite" Catalysts: XPS structure elucidation and correlation with catalytic activity, J. Electron Spectros. Relat. Phenomena. 27 (1982) 119–128. https://doi.org/10.1016/0368-2048(82)85058-5.

[242] G.C. Allen, S.J. Harris, J.A. Jutson, J.M. Dyke, A study of a number of mixed transition metal oxide spinels using X-ray photoelectron spectroscopy, Appl. Surf. Sci. 37 (1989) 111–134. https://doi.org/10.1016/0169-4332(89)90977-X.

[243] A. Latifi, M. Imani, M.T. Khorasani, M.D. Joupari, Electrochemical and chemical methods for

improving surface characteristics of 316L stainless steel for biomedical applications, Surf. Coatings Technol. 221 (2013) 1–12. https://doi.org/10.1016/j.surfcoat.2013.01.020.

[244] R.H. Jung, H. Tsuchiya, S. Fujimoto, XPS characterization of passive films formed on Type 304 stainless steel in humid atmosphere, Corros. Sci. 58 (2012) 62–68. https://doi.org/10.1016/j.corsci.2012.01.006.

[245] A.A. Hermas, XPS analysis of the passive film formed on austenitic stainless steel coated with conductive polymer, Corros. Sci. 50 (2008) 2498–2505. https://doi.org/10.1016/j.corsci.2008.06.019.

[246] W. Fredriksson, S. Malmgren, T. Gustafsson, M. Gorgoi, K. Edström, Full depth profile of passive films on 316L stainless steel based on high resolution HAXPES in combination with ARXPS, Appl. Surf. Sci. 258 (2012) 5790–5797. https://doi.org/10.1016/j.apsusc.2012.02.099.

[247] T. Hryniewicz, K. Rokosz, Analysis of XPS results of AISI 316L SS electropolished and magnetoelectropolished at varying conditions, Surf. Coatings Technol. 204 (2010) 2583–2592. https://doi.org/10.1016/j.surfcoat.2010.02.005.

[248] C.J.P. Alexander, V. Naumkin, Anna Kraut-Vass, Stephen W. Gaarenstroom, NIST X-ray Photoelectron Spectroscopy Database, NIST Stand (2012). https://doi.org/http://dx.doi.org/10.18434/T4T88K.

[249] A.M. Salvi, J.E. Castle, J.F. Watts, E. Desimoni, Peak fitting of the chromium 2p XPS spectrum, Appl. Surf. Sci. 90 (1995) 333–341. https://doi.org/10.1016/0169-4332(95)00168-9.

[250] M.C. Biesinger, B.P. Payne, A.P. Grosvenor, L.W.M. Lau, A.R. Gerson, R.S.C. Smart, Resolving surface chemical states in XPS analysis of first row transition metals, oxides and hydroxides: Cr, Mn, Fe, Co and Ni, Appl. Surf. Sci. 257 (2011) 2717–2730. https://doi.org/10.1016/j.apsusc.2010.10.051.

[251] S. Revisited, X - ray Photoelectron Spectroscopy (XPS) Reference Pages, (2015) 2–5.

[252] M. Aronniemi, J. Sainio, J. Lahtinen, Chemical state quantification of iron and chromium oxides using XPS: The effect of the background subtraction method, Surf. Sci. 578 (2005) 108–123.

https://doi.org/10.1016/j.susc.2005.01.019.

[253]   M.S. Greenwood, J.P. Duarte, M. Corradini, Presentation and comparison of experimental critical heat flux data at conditions prototypical of light water small modular reactors, Nucl. Eng. Des. 317 (2017) 220–231. https://doi.org/10.1016/j.nucengdes.2016.12.030.

[254]   J.P. Duarte, D. Zhao, H. Jo, M.L. Corradini, Critical heat flux experiments and a post-CHF heat transfer analysis using 2D inverse heat transfer, Nucl. Eng. Des. 337 (2018) 17–26. https://doi.org/10.1016/j.nucengdes.2018.06.011.

[255]   D. Lee, B.S. Kim, H. Moon, N. Lee, S. Shin, H.H. Cho, Enhanced boiling heat transfer on nanowire-forested surfaces under subcooling conditions, Int. J. Heat Mass Transf. 120 (2018) 1020–1030. https://doi.org/10.1016/j.ijheatmasstransfer.2017.12.100.

[256]   D. Lee, N. Lee, D. Il Shim, B.S. Kim, H.H. Cho, Enhancing thermal stability and uniformity in boiling heat transfer using micro-nano hybrid surfaces (MNHS), Appl. Therm. Eng. 130 (2018) 710–721. https://doi.org/10.1016/j.applthermaleng.2017.10.144.

[257]   R. Sugrue, J. Buongiorno, T. McKrell, An experimental study of bubble departure diameter in subcooled flow boiling including the effects of orientation angle, subcooling, mass flux, heat flux, and pressure, Nucl. Eng. Des. 279 (2014) 182–188. https://doi.org/10.1016/j.nucengdes.2014.08.009.

[258]   H.H. Son, N. Kim, S.J. Kim, Nano/microscale roughness control of accident-tolerant Cr- and CrAl-coated surfaces to enhance critical heat flux, Appl. Therm. Eng. 167 (2020) 114786. https://doi.org/10.1016/j.applthermaleng.2019.114786.

[259]   D. Lee, B. Elward, P. Brooks, R. Umretiya, J. Rojas Supervised, M. Bucci Supervised, R.B. Rebak, M. Anderson Supervised, Enhanced flow boiling heat transfer on chromium coated zircaloy-4 using cold spray technique for Accident Tolerant Fuel (ATF) materials, Appl. Therm. Eng. 185 (2020) 116347. https://doi.org/10.1016/j.applthermaleng.2020.116347.

[260]   W. Polini, L. Sorrentino, M. Seo, N. Sato, A. Mahapatro, D.M. Johnson, D.N. Patel, M.D. Feldman, A.A. Ayon, C.M. Agrawal, L. Sorrentino, L. Carrino, E. Forrest, R. Schulze, C. Liu, D.

Dombrowski, L. Bónová, A. Zahoranová, D. Kováčik, M. Zahoran, M. Mičušík, M. Černák, International Journal of Heat and Mass Transfer Influence of surface contamination on the wettability of heat transfer surfaces, Appl. Surf. Sci. 91 (2015) 311–317. https://doi.org/10.1021/la052817h.

[261] Contact Angle, Wettability and Adhesion., VSP, an imprint of Brill Academic Publishers, Leiden, Netherlands, 2008.

[262] M. Mantel, J.P. Wightman, Influence of the surface chemistry on the wettability of stainless steel, Surf. Interface Anal. 21 (1994) 595–605. https://doi.org/10.1002/sia.740210902.

[263] P.S. G. Su, M. Bucci, Investigations on the Thermal-hydraulic Behavior of Accident Tolerant Fuel Cladding Materials, 2020.

[264] K.T. Hong, H. Imadojemu, R.L. Webb, Effects of oxidation and surface roughness on contact angle, Exp. Therm. Fluid Sci. 8 (1994) 279–285. https://doi.org/10.1016/0894-1777(94)90058-2.

[265] D.R. Baer, M.H. Engelhard, A.S. Lea, P. Nachimuthu, T.C. Droubay, J. Kim, B. Lee, C. Mathews, R.L. Opila, L. V. Saraf, W.F. Stickle, R.M. Wallace, B.S. Wright, Comparison of the sputter rates of oxide films relative to the sputter rate of SiO2, J. Vac. Sci. Technol. A Vacuum, Surfaces, Film. 28 (2010) 1060–1072. https://doi.org/10.1116/1.3456123.

[266] S.M. Rossnagel, J.R. Sites, X-ray photoelectron spectroscopy of ion beam sputter deposited SiO2, TiO2, and Ta2O5, J. Vac. Sci. Technol. an Off. J. Am. Vac. Soc. 2 (1984) 376–379.

[267] A. Sathyamoorthy, W. Weisweiler, Studies of the sputter deposition of carbon, silicon and SiC films, Thin Solid Films. 87 (1982) 33–42. https://doi.org/10.1016/0040-6090(82)90568-5.

[268] L. Kalina, V. Bílek, M. Bušo, J. Koplík, J. Másilko, Thickness determination of corrosion layers on iron using XPS depth profiling, Mater. Tehnol. 52 (2018) 537–540. https://doi.org/10.17222/mit.2016.180.

[269] M.P. Seah, T.S. Nunney, Sputtering yields of compounds using argon ions, J. Phys. D. Appl. Phys. 43 (2010). https://doi.org/10.1088/0022-3727/43/25/253001.

[270] D. Briggs, X-ray photoelectron spectroscopy (XPS), Handb. Adhes. Second Ed. (2005) 621–622.

https://doi.org/10.1002/0470014229.ch22.

[271] S.L. Chang, J.W. Anderegg, P.A. Thiel, Surface oxidation of an Al-Pd-Mn quasicrystal, characterized by X-ray photoelectron spectroscopy, J. Non. Cryst. Solids. 195 (1996) 95–101. https://doi.org/10.1016/0022-3093(95)00537-4.

[272] P.M.A. Sherwood, Introduction to Studies of Phosphorus-Oxygen Compounds by XPS, Surf. Sci. Spectra. 9 (2002) 62–66. https://doi.org/10.1116/11.20030101.

[273] O. Al, Al oxides and hydroxides peak fits, Handbooks Monochromatic XPS Spectra. 3 (2005) 43–66.

[274] J. Kumar, A. Awasthi, Modified trivial rejection criteria in Cohen-Sutherland line clipping algorithm, Commun. Comput. Inf. Sci. 125 CCIS (2011) 1–10. https://doi.org/10.1007/978-3-642-18440-6_1.

[275] X. Zhu, M. Todeschini, A. Bastos da Silva Fanta, L. Liu, F. Jensen, J. Hübner, H. Jansen, A. Han, P. Shi, A. Ming, C. Xie, In-depth evolution of chemical states and sub-10-nm-resolution crystal orientation mapping of nanograins in Ti(5 nm)/Au(20 nm)/Cr(3 nm) tri-layer thin films, Appl. Surf. Sci. 453 (2018) 365–372. https://doi.org/10.1016/j.apsusc.2018.05.042.

[276] N.S. McIntyre, D.G. Zetaruk, X-ray Photoelectron Spectroscopic Studies of Iron Oxides, Anal. Chem. 49 (1977) 1521–1529. https://doi.org/10.1021/ac50019a016.

[277] A.P. Grosvenor, B.A. Kobe, M.C. Biesinger, N.S. McIntyre, Investigation of multiplet splitting of Fe 2p XPS spectra and bonding in iron compounds, Surf. Interface Anal. 36 (2004) 1564–1574. https://doi.org/10.1002/sia.1984.

[278] M. Digne, P. Sautet, P. Raybaud, H. Toulhoat, E. Artacho, Structure and stability of aluminum hydroxides: A theoretical study, J. Phys. Chem. B. 106 (2002) 5155–5162. https://doi.org/10.1021/jp014182a.

[279] D.R. Lide, Handbook of Chemistry and Physics, Internet Version, 2005.

[280] W. Han, K. Yabuuchi, A. Kimura, S. Ukai, N. Oono, T. Kaito, T. Torimaru, S. Hayashi, Effect of Cr/Al contents on the 475°C age-hardening in oxide dispersion strengthened ferritic steels, Nucl.

Mater. Energy. 9 (2016) 610–615. https://doi.org/10.1016/j.nme.2016.05.015.

[281] C. Capdevila, M.K. Miller, K.F. Russell, J. Chao, J.L. González-Carrasco, Phase separation in PM 2000[TM] Fe-base ODS alloy: Experimental study at the atomic level, Mater. Sci. Eng. A. 490 (2008) 277–288. https://doi.org/10.1016/j.msea.2008.01.029.

[282] W.S. Spear, D.H. Polonis, Interstitial precipitation in Fe-Cr-Al alloys, Metall. Mater. Trans. A. 25 (1994) 1135–1146. https://doi.org/10.1007/BF02652289.

[283] J. Petrík, P. Palfy, The influence of the load on the hardness, Metrol. Meas. Syst. 18 (2011) 5. https://doi.org/10.2478/v10178-011-0005-5.

[284] G. Ryge, D.E. Foley, C.W. Fairhurst, Micro-indentation Hardness, in: Annu. Meet. Int. Assoc. Dent. Res., 1960.

[285] G. Su, M. Bucci, P. Sabharwall, A. Jena, H. Kim, B. Phillips, M. Anderson, M. Corradini, B. Elward, E. Guiterrez, H. Jo, H. Yeom, K. Sridharan, J. Rojas, R. Umretiya, N. Brown, J. Gorton, M. Chen, M. He, S. Lee, Y. Lee, A. Prinja, R. Christensen and Ter, Investigations on the thermal-hydraulic behavior of Accident Tolerant Fuel cladding materials, DOE technical report, Idaho National lab, 2020.

[286] J. Callister William D., Materials science and engineering : an introduction, 9th editio, 2014.

[287] F. Reyes-Gómez, W.R. Aguirre-Contreras, G.A. Pérez Alcázar, J.A. Tabares, Theoretical and experimental comparative study about magnetic behavior of Fe-Al alloys in the high Fe concentration region, J. Alloys Compd. 735 (2018) 870–879. https://doi.org/10.1016/j.jallcom.2017.11.207.

[288] S. Pramanik, S. Suwas, Low-Density Steels: The Effect of Al Addition on Microstructure and Properties, Jom. 66 (2014) 1868–1876. https://doi.org/10.1007/s11837-014-1129-2.

[289] R. Elilarassi, G. Chandrasekaran, Effect of annealing on structural and optical properties of zinc oxide films, Mater. Chem. Phys. 121 (2010) 378–384. https://doi.org/10.1016/j.matchemphys.2010.01.053.

[290] D.J. Quesnel, M. Meshii, J.B. Cohen, Residual stresses in high strength low alloy steel during low

cycle fatigue, Mater. Sci. Eng. 36 (1978) 207–215. https://doi.org/10.1016/0025-5416(78)90073-3.

[291] A.C. Vermeulen, E. Houtman, Determination of alignment errors in classical XRD residual stress methods, Mater. Sci. Forum. 347 (2000) 17–22. https://doi.org/10.4028/www.scientific.net/msf.347-349.17.

[292] G.E. Global, N. Fuels, G.E. Power, R. Fawcett, R. Augi, C. Paone, P. Davis, D. Lutz, M. Powers, D. Keck, B. Eber, K. Ledford, P. Cantonwine, R. Stachowski, Y. Lin, S. Desilva, J. Harrison, R. Rand, M. Yilmaz, B. Frew, B. Moore, J. Head, B. Schulz, L. Schichlein, P. Davis, R. Higgins, K. Martin, J. Banfield, J. Reynolds, M. Short, P. Mccumbee, S. Nuclear, J.B. Williams, J. Chavers, N.A. Satterlee, I. National, M. Pi, G. Hoggard, J. Harp, G. Povirk, G. Core, B. Durtschi, C. Woolum, R.O. Brien, DE-NE0008221 GE Final Technical and Scientific Report, 2018.

[293] M.L. Sievers, Influence of grain size on the mechanical behaviour of some high strength materials, Ann. Intern. Med. 84 (1976) 755–756.

[294] J. Yuan, W. Wang, S. Zhu, F. Wang, Comparison between the oxidation of iron in oxygen and in steam at 650-750°C, Corros. Sci. 75 (2013) 309–317. https://doi.org/10.1016/j.corsci.2013.06.014.

[295] B. Qiu, J. Wang, Y. Deng, M. Wang, Y. Wu, S.Z. Qiu, A review on thermohydraulic and mechanical-physical properties of SiC, FeCrAl and Ti3SiC2 for ATF cladding, Nucl. Eng. Technol. 52 (2020) 1–13. https://doi.org/10.1016/j.net.2019.07.030.

[296] J.A. Nychka, D.R. Clarke, Quantification of aluminum outward diffusion during oxidation of FeCrAl alloys, Oxid. Met. 63 (2005) 325–352. https://doi.org/10.1007/s11085-005-4391-4.

[297] C. Tang, A. Jianu, M. Steinbrueck, M. Grosse, A. Weisenburger, H.J. Seifert, Influence of composition and heating schedules on compatibility of FeCrAl alloys with high-temperature steam, J. Nucl. Mater. 511 (2018) 496–507. https://doi.org/10.1016/j.jnucmat.2018.09.026.

[298] T. Horita, H. Kishimoto, K. Yamaji, Y. Xiong, M.E. Brito, H. Yokokawa, Y. Baba, K. Ogasawara, H. Kameda, Y. Matsuzaki, S. Yamashita, N. Yasuda, T. Uehara, Diffusion of oxygen in the scales of Fe-Cr alloy interconnects and oxide coating layer for solid oxide fuel cells, Solid State Ionics. 179 (2008) 2216–2221. https://doi.org/10.1016/j.ssi.2008.07.024.

[299]   D. Pan, R. Zhang, H. Wang, Y. Xu, H. Wang, In Steam Short-Time Oxidation Kinetics of FeCrAl Alloys, J. Mater. Eng. Perform. 27 (2018) 6407–6414. https://doi.org/10.1007/s11665-018-3665-3.

[300]   R.H. Wilson, D.A. Farnsworth, R.H. Stoudt, Babcock & Wilcox Correlation of Critical Heat Flux, 1980.

[301]   L. Biasi, G.C. Clerici, S. Garriba, R. Sala, A. Tozzi, A New Correlation for Round Duct and Uniform: Heating-Comparison With World Data, 1967.

[302]   F.O.R.A.N. Axially, L.S. Tong, W-3 Westinghouse Correlation, J. Nucl. Energy. 21 (1967) 241–248.

[303]   S.G. Kandlikar, A Theoretical Model to Predict Pool Boiling CHF Incorporating Effects of Contact Angle and Orientation, J. Heat Transfer. 123 (2001) 1071. https://doi.org/10.1115/1.1409265.

[304]   W.M. Rohsenow, A Method of Correlating Heat Transfer Data for Surface Boiling of Liquids, Trans. ASME. Vol.74 (n.d.) 969–976.

[305]   K.H. Sun, J.H. Lienhard, The peak pool boiling heat flux on horizontal cylinders, Int. J. Heat Mass Transf. 13 (1970). https://doi.org/10.1016/0017-9310(70)90178-X.

[306]   G.H. Seo, G. Jeun, S.J. Kim, Pool boiling heat transfer characteristics of zircaloy and SiC claddings in deionized water at low pressure, Exp. Therm. Fluid Sci. 64 (2015) 42–53. https://doi.org/10.1016/j.expthermflusci.2015.01.017.

[307]   M. Lee, Critical heat flux approach for square rod bundles using the 1995 Groeneveld CHF table and bundle data of heat transfer research facility, Nucl. Eng. Des. 197 (2000) 357–374. https://doi.org/10.1016/S0029-5493(99)00294-0.

[308]   T.R.-3D© C.D. Team, RELAP5-3D © Code Manual Volume I: Code Structure, System Models and Colution Methods, 2015.

[309]   T.R.-3D© C.D. Team, RELAP5-3D © Code Manual Volume II: User's Guide and Input Requirements, 2015.

[310]   J.K. Fink, L. Leibowitz, Thermal conductivity of zirconium, J. Nucl. Mater. 226 (1995) 44–50.

162

VITA

Rajnikant V Umretiya

EDUCATION

- **Virginia Commonwealth University (May 2021)**

PhD Candidate in Mechanical & Nuclear Engineering Department

- **Virginia Commonwealth University (May 2019)**

Master of Science in Mechanical & Nuclear Engineering

- **L D College of Engineering, India (May 2015)**

Bachelor of Engineering in Mechanical Engineering

PUBLICATIONS

- **R.V. Umretiya**, S. Vargas, D. Galeano, R. Mohammadi, C.E. Castano, J.V. Rojas, Effect of Surface Characteristics and Environmental Aging on Wetting of Cr-coated Zircaloy-4 Accident Tolerant Fuel Cladding Material, J. Nucl. Mater. (2020) 152163.

- **R.V. Umretiya**, B. Elward, D. Lee, M. Anderson, R. B. Rebak, J.V. Rojas, Mechanical and Chemical Properties of PVD and Cold Spray Cr-coatings on Zircaloy-4, J. Nucl. Mater. (2020) 152420.

- D. Lee, B. Elward, P. Brooks, **R. Umretiya**, J. Rojas, M. Bucci, R. B. Rebak, M. Anderson, Enhanced flow boiling heat transfer on chromium coated zircaloy-4 using cold spray technique for accident tolerant fuel (ATF), Applied Thermal Engineering. (2021) 116347.

- **R.V. Umretiya**, D. Lee, B. Elward, M. Anderson, R. B. Rebak, J.V. Rojas, Microstructure and Surface Characteristics Evolution of FeCrAl alloys after Flow Boiling Testing, in submission process (J. Nucl. Mater.).

- J.V. Rojas, **R.V. Umretiya**, M.C. Molina-Higgins, A. Gawi, S. Gobalakrishnan, J. Zweit, Incorporation of ^{67}Cu within luminescent lanthanide phosphate nanoparticles for theranostics, under review (ACS Applied Nano Materials).

- **R.V. Umretiya**, B. Elward, M. Anderson, R. B. Rebak, J.V. Rojas, The effect of ramp heating on the microstructure and surface chemistry of APMT FeCrAl alloy, in preparation.

CONFERENCE PROCEEDINGS

- **R.V. Umretiya**, D. Ginetro, S. Bilbao y Leon, B. Elward, M. Andreson, R.B. Rebak, J.V. Rojas, Surface Characteristics of Accident Tolerant Fuel Cladding and their potential impact in Critical Heat Flux, in NURETH conference proceedings, 2019.

- **R.V. Umretiya**, R. Uhorchuk, S. Vargas, C.E. Castano, J.V. Rojas, Surface Characterization of Chromium Coated Zircaloy-4 Accident Tolerant Fuel Cladding Material, in ANS conference proceedings, 2019.

- **R.V. Umretiya**, S. Vargas, R. Uhorchuk, C.E. Castano, J.V. Rojas, Aging Effect of Chromium Coated Zircaloy-4 Accident Tolerant Fuel Cladding Material, in ANS conference proceedings, 2019.
- **R.V. Umretiya**, R. Uhorchuk, M. Andreson, B. Elward, S. Bilbao y Leon, R.B. Rebak, J.V. Rojas, Evaluation of Surface Characteristics of FeCrAl alloy Accident Tolerant Fuel Cladding Material after Critical Heat Flux Testing under Atmospheric Pressure, in ANS conference proceedings, 2019.
- R. Uhorchuk, **R.V. Umretiya**, M. Andreson, B. Elward, S. Bilbao y Leon, R.B. Rebak, J.V. Rojas, Influence of Surface Roughness on Wettability of Accident Tolerant Fuels Cladding, in ANS conference proceedings, 2019.
- G. Su, M. Bucci, P. Sabharwall, A. Jena, H. Kim, B. Phillips, M. Anderson, M. Corradini, B. Elward, E. Guiterrez, H. Jo, H. Yeom, K. Sridharan, J. Rojas, **R. Umretiya**, N. Brown, J. Gorton, M. Chen, M. He, S. Lee, Y. Lee, A. Prinja, R. Christensen and Ter, Investigations on the thermal-hydraulic behavior of Accident Tolerant Fuel cladding materials, DOE technical report, Idaho National Lab, 2020.